Optimising the Efficiency of Coherent Optical Packet Switched Networks

Anthony John Walsh

BE (Hons)

A Thesis Submitted in Fulfilment of the Requirements for the

Award of

Doctor of Philosophy (PhD)

to the

Dublin City University

Faculty of Engineering and Computing

School of Electronic Engineering

Supervisor: Prof. Liam P. Barry

External Supervisor: Prof. Andrew D. Ellis (Aston University, United Kingdom)

June 2015

Declaration

I hereby certify that this material, which I now submit for assessment on the programme of study leading to the award of Doctor of Philosophy is entirely my own work, and that I have exercised reasonable care to ensure that the work is original, and does not to the best of my knowledge breach any law of copyright, and has not been taken from the work of others save and to the extent that such work has been cited and acknowledged within the text of my work.

Signed: _____________ (Anthony Walsh)

ID No.: ____________

Date: _______

Table of Contents

List of Figures

Acronyms

3D	3-Dimensional
ASE	Amplified Spontaneous Emission
AWGN	Additive White Gaussian Noise
BER	Bit error rate
BERT	Bit Error Rate Tester
BPSK	Binary Phase Shift Keying
CCDF	Complementary Cumulative Distribution Function
CMA	Constant Modulus Algorithm
DBPSK	Differential Binary Phase Shift Keying
DBR	Distributed Bragg reflector
DDPSK	Doubly Differential Phase Shift Keying
DDQPSK	Doubly Differential Quadrature Phase Shift Keying
DFB	Distributed feed-back
DP-DQPSK	Dual-polarisation differential quadrature phase shift keying
DP-QPSK	Dual-Polarisation Quadrature Phase Shift Keying
DPSK	Differential Phase Shift Keying
DQPSK	Differential Quadrature Phase Shift Keying
DS-DBR	Digital supermode distributed Bragg reflector
DSP	Digital Signal Processing
ECL	External cavity laser
EDFA	Erbium Doped Fibre Amplifier
FEC	Forward Error Correction
FFT	Fast-Fourier Transform
FPGA	Field-Programmable Gate Array
FWHM	Full-Width Half-Maximum
IP	Internet Protocol
LMS	Least Mean Squares
LO	Local Oscillator
MZM	Mach-Zehnder Modulator
NRZ	Non-return-to-zero
OADM	Optical Add/Drop Multiplexer
OBS	Optical burst switching
OCS	Optical circuit switching
OFDM	Orthogonal frequency division multiplexing

OLT	Optical Line Terminal
OOK	On-off keying
OPS	Optical packet switching
OSA	Optical Spectrum Analyser
OSNR	Optical Signal to Noise Ratio
OTN	Optical Transport Network
PBS	Polarisation Beam Splitter
PC	Polarisation Controller
PD	Photodiode
PMD	Polarisation Mode Dispersion
PRBS	Pseudo random bit sequence
PSD	Power spectral density
PSK	Phase Shift Keying
QAM	Quadrature amplitude modulation
QPSK	Quadrature Phase Shift Keying
RFSA	Radio Frequency Spectrum Analyser
RIN	Relative intensity noise
Rx	Receiver
SDH	Synchronous Digital Hierarchy
SDPSK	Single Differential Phase Shift Keying
SDQPSK	Single Differential Quadrature Phase Shift Keying
SG-DBR	Sampled grating distributed Bragg reflector
SMSR	Side-mode suppression ratio
SNR	Signal to noise ratio
SNR_b	Signal to noise ratio per bit
SOA	Semiconductor optical amplifier
SONET	Synchronous Optical Network
TLS	Tuneable Laser Source
Tx	Transmitter
VOA	Variable Optical Attenuator
WDM	Wavelength Division Multiplexing

Abstract

Thesis Title: Optimising the Efficiency of Coherent Optical Packet Switched Networks

Author: Anthony John Walsh

There is a continuing need to increase throughput in optical networks to satisfy the demands of internet applications. However, the non-linear Shannon capacity of standard single mode fibre is being approached. Also, almost all of the power used in optical networks is used by electronic routers. One possible solution to deal with both problems is to use optical packet switching. Optical packet switching uses fast switching tuneable lasers, which can change wavelength in the order of a several nanoseconds, to dynamically vary wavelength assignments in a network, and thus achieve routing in the network without electronic routers. In addition, fast wavelength assignment reduces waiting times, resulting in better utilization of network resources.

However, the frequency dynamics of the tuneable lasers after switching wavelengths increases the waiting times required to successfully transmit data packets. In this thesis, frequency and phase dynamics of a tuneable laser transmitter, after a wavelength switching event, are initially characterised accurately using a novel technique. The effects that the frequency dynamics have on the transmission of coherent optical communication signals are mitigated using doubly differential decoding, a new approach proposed in this work for application in optical packet switched networks. This technique reduces the waiting times required to successfully transmit data after a wavelength switching event, and this enhances overall network efficiency and throughput. In addition, this work proposes and demonstrates the use of a least-mean squares algorithm to overcome polarisation demultiplexing issues which are present in these networks, which also decreases waiting times, increases network efficiency, and improves system robustness.

Acknowledgements

Firstly, I would like to thank my supervisor, Prof. Liam P. Barry, who supervised me during my time at Dublin City University. I am grateful for the advice and support he gave me during my PhD, without which I would not have been able to complete my PhD.

I would like to thank Prof. Andrew D. Ellis for supervising me during my time at the Tyndall National Institute and co-supervising me during my time at Dublin City University. I am grateful for the support he gave me and the patience he afforded me.

I would like to thank Science Foundation Ireland for funding my research. I would like to thank the Tyndall National Institute, University College Cork, the Rince Institute and Dublin City University for providing me with a world-class environment to conduct my research. I would also like to thank James Mountjoy and Anthony Fagan from University College Dublin for collaborating with me during my PhD.

My acknowledgements would not be complete if I did not mention my colleagues at Tyndall and Dublin City University, whose friendship helped me through the difficult periods of my PhD, most notably Ciaran, Sean, Jiadi, John, Vivian, and Prince.

Finally, I would like to thank my family; Mom, Dad, my brothers, my sisters, and their partners. Without their support, both emotional and financial, this PhD would not have been completed. It is to them that I dedicate my thesis.

Chapter 1

Introduction

There is a continuing demand for data rates through fibre optic telecommunication networks to be increased for internet applications. The non-linear Shannon capacity limit of optical fibre is being reached. This has prompted the revival of coherent optical communications in order to increase the spectral efficiency of communication links by using higher-order modulation formats and, consequently, increase throughput. In addition, there is a motivation to reduce the role of electronic routing by using optical burst switched (OBS) networks or optical packet switched (OPS) networks, which can improve the energy efficiency of optical networks, while also enhancing the utilisation of the network capacity through fast setting up and taking down of lightpaths in response to changes in demands between nodes. OBS and OPS typically use tuneable lasers which switch wavelength at the transmitter and/ or receiver in order to route bursts or packets throughout the network.

Previous research focused on intensity modulation and direct detection for transmission and reception of optical packets and bursts. Only recently has research has begun to focus on phase and polarisation modulation, as well as coherent detection, which can further improve spectral efficiency and throughput. The pursuit of coherent optical packet/ burst switched networks could potentially lead to achieving both higher data rates and lower energy consumption. However, there are a number of key issues that need to be addressed when considering coherent optical packet/ burst switched networks:

- Switching the wavelength of tuneable lasers within the order of nanoseconds can produce time-varying frequency transients as the laser settles to a new wavelength. Since coherent communications is affected by both frequency offsets between the transmitting laser and local oscillator (LO) laser at the receiver as well as phase noise, there is a need to develop suitable characterisation techniques in order to characterise the time-varying deterministic frequency transients as well as the time-varying phase noise. Difficulties can arise when trying to separate deterministic time-varying frequency transients from time-varying phase noise profiles as the laser settles to its destination wavelength. However, in order to determine how to best modulate the switching laser and decode coherent optical packets/bursts, it is necessary to characterise deterministic and random phase impairments.

- These often large, time-varying deterministic frequency transients which occur after the tuneable lasers switch wavelengths can cause problems for frequency offset correction at the coherent receiver. Blind digital signal processing (DSP) algorithms used to compensate for the effects of frequency offsets have limited ranges for phase shift keying (PSK) which means that large time-varying frequency offsets may not be properly compensated for. This can result in large waiting times if frequency transient must enter the algorithm's range, or possibly the loss of a packet if it never enters its range. Hence, there is a need to develop a transmission and decoding algorithm which has a large frequency offset range so that PSK packets will not be lost due to the limited range provided by DSP algorithms.
- The network requires robust demodulation algorithms which can quickly compensate for unknown frequency offsets, mitigate phase noise, and demodulate polarisation-multiplexed signals with unknown polarisation rotations. However, one of the most widely used algorithms for polarisation demultiplexing, the constant modulus algorithm (CMA), can have long and variable convergence times. The CMA can also suffer from singularity issues which can result in the permanent loss of the data on one polarisation, although, techniques to avoid this have been introduced. For efficient coherent optical packet/burst switched networks it is necessary to apply a polarisation demultiplexing scheme which has short, non-varying waiting times, and cannot suffer from the singularity issues associated with the CMA.

The following are the main contributions of this work:

- A novel time-resolved characterisation technique to characterise the phase dynamics of a fast switching tuneable laser after a switching event is proposed. The method is based on determining a time-resolved 3-D complementary cumulative distribution functions (CCDFs) of the instantaneous differential phase of the switching laser after a switching event. This method overcomes any potential confusion when trying to consistently characterise both frequency chirp and phase noise since this novel method simultaneously takes both into account in a consistent manner, something which previous techniques do not. The validity of this method is verified by comparing calculated time-resolved bit error rates (BERs) expected from the 3-D CCDF of the instantaneous differential phase with time-resolved BERs measured from a transmission experiment, with very close matching observed.

- The limited frequency offset range typically associated with blind frequency offset compensation/ estimation schemes which use one sample per symbol is overcome by using doubly differential phase shift keying (DDPSK). Since DDPSK has a frequency offset limited only by the bandwidth of the receiver electronics, it allows for very large frequency offsets which may be encountered by coherent optical packet/ burst receivers (also for larger symbol rates it takes smaller frequency offsets for the limited electronic bandwidth to filter out the data). However, DDPSK has a large signal to noise ratio (SNR) penalty compared with conventional methods. A proposed novel decoding scheme called "M^{th} power DDPSK" can greatly reduce the SNR penalty associated with simple DDPSK while still retaining the same large frequency offset tolerance. Very short waiting times are demonstrated using a coherent optical packet/ burst switched transmission system using a tuneable laser transmitter.
- One method of demultiplexing a signal which has two PSK signals, one on each polarisation, is the least mean squares (LMS) method of fitting a plane to a 3-D Stokes space surface (published by a different group) whose normal vector can be used to calculate a polarisation demultiplexing matrix. This method is applied for the first time in a coherent optical packet/ burst switched scenario in order to overcome issues such as the singularity problem and variable convergence times associated with the CMA which has been previously implemented, with different variations, in coherent optical packet/ burst receivers. The LMS method is used with M^{th} power doubly differential quadrature phase shift keying (DDQPSK) and achieves shorter waiting times than other comparable blind compensation methods that decode polarisation-multiplexed quadrature phase shift keying (QPSK) packets or bursts (where the other methods do not employ additional hardware).

The overall structure of the thesis is as follows:

Chapter 2 introduces optical telecommunication networks and focuses on OPS and OBS networks. It explains the motivations behind designing a coherent optical packet/ burst switched network. The main devices of interest in the thesis are described here, which are lasers (tuneable lasers in particular), external modulators and optical receivers. In addition, different modulation schemes are partially discussed.

Chapter 3 discusses the motivations, major concepts and impairments associated with coherent communications. Phase noise, which is an impairment of significant importance in coherent communications, is described along with methods of experimentally characterising the level of phase noise of a static laser and a laser that switches wavelength. DSP for compensating and mitigating back-to-back impairments are discussed as well as additional DSP for decoding phase modulated data which had encoding applied at the transmitter. Penalties associated with different decoding methods are also discussed.

Chapter 4 discusses the most accurate way of estimating the Wiener phase noise of a static laser using a coherent receiver setup. This chapter also proposes a novel frequency chirp and dynamic phase noise characterisation technique which uses time-resolved 3-D complementary cumulative distribution functions (CCDFs) of instantaneous differential phase which can simultaneously capture the deterministic and random phase dynamics after a laser switches wavelength in a consistent manner with very high time-resolution. The validity of this method is verified by comparing measured time-resolved BERs with expected time-resolved BERs calculated using 3-D CCDF plots of the instantaneous differential phase, showing very close matching.

Chapter 5 discusses the use of doubly differential decoding to overcome the limited frequency offset tolerance of commonly used frequency offset compensation algorithms. DDPSK has a frequency offset range limited only by the bandwidth of the electronics (for larger symbol rates it takes smaller frequency offsets for the limited electronic bandwidth to filter out the random data spectrum). However, DDPSK has a large SNR penalty compared with PSK. A proposed novel decoding system called "M^{th} power DDPSK" has the same frequency offset tolerance as the simple DDPSK system but has a much lower SNR penalty compared with PSK than the simple DDPSK system. Simulation and experimental results are provided for static lasers using QPSK constellations and experimental results are provided for the switching case using QPSK constellations. Lower waiting times can be achieved by using M^{th} power DDQPSK than if the typically employed DSP were used.

Chapter 6 describes how the CMA is typically implemented to demultiplex two transmitted streams of data sent on two different polarisations in coherent optical packet/ burst switched scenarios. It is proposed here that an algorithm published by a different group, which uses a LMS method to determine a best-fit plane to 3-D plots of s-parameters in order to determine a demultiplexing matrix, could be used to demultiplex packets or bursts modulated with polarisation-multiplexed DDPSK. The implementation of this LMS method with M^{th} power DDPSK in coherent optical packet/ burst scenarios is a novel undertaking and results in the lowest reported waiting times of blind polarisation demultiplexing algorithms in a switching scenario using QPSK constellations (without the use of additional hardware).

Chapter 7 provides conclusions and proposes future research directions for this work.

Chapter 2

Optical Packet Switched Networks

This chapter introduces the fundamental concepts behind optical networks, provides the motivation for investigating coherent optical packet switched networks, and provides detail on the key devices used in coherent optical packet switched networks.

2.1 Optical Networks

There has been an enormous increase in the bit rates available to internet users, where global internet protocol (IP) traffic (GBytes/s) versus year is shown in Figure 2.1 using data from [1]. There are indications that this trend will continue, such as the possible replacing of television broadcast channels with internet catch-up services [2]. At the same time as the demands on the optical networks are increasing, the non-linear Shannon capacity limit of fibre is being reached [3]. In addition, there is also evidence to suggest that a large proportion of energy consumption in optical communications is in the electronic routing equipment used in networks as opposed to the wavelength division multiplexed links [4].

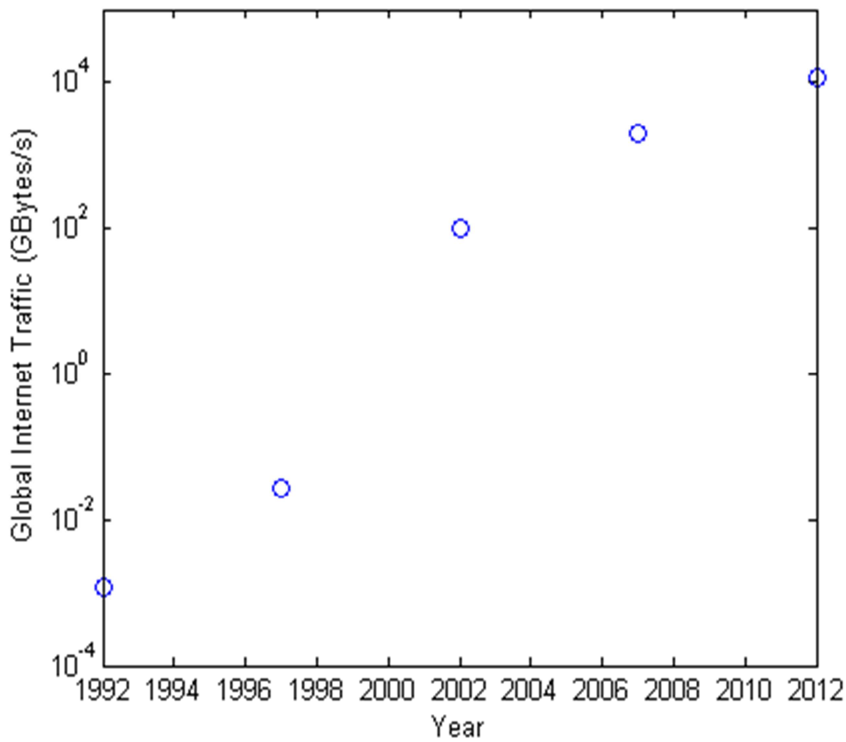

Figure 2.1: Global internet traffic versus year [1].

The optical network is typically divided into three sections (i) the access network (ii) the metro network and (iii) the core network. The access network is where the customer or end user connects to, and it provides access to a metro network. Access networks can have a tree-like network structure [5]. The data from customers is aggregated and if needs be is passed onto the metro network. The metro network services a metropolitan size area and connects access networks together. Metro networks can often take the form of a ring network where SONET/SDH rings are used [5] (SONET= “Synchronous Optical Network”, SDH= “Synchronous Digital Hierarchy”). Note that SONET, SDH and also OTN (“Optical Transport Network”) are fibre transmission systems/protocols [6]. Various metro networks are then connected together in a core network which is often of the form of a mesh network which can be justified as large traffic demands on the core network can be expected [5]. Core networks generally send large amounts of information over long distances. Note that the focus of this thesis will be on metro networks with a description of current and possible future metro networks given in the following sections.

2.1.1 Wavelength Division Multiplexing

In metro networks data is typically multiplexed by wavelength where this paradigm is referred to as wavelength division multiplexing (WDM), where an example WDM link is shown in Figure 2.2.

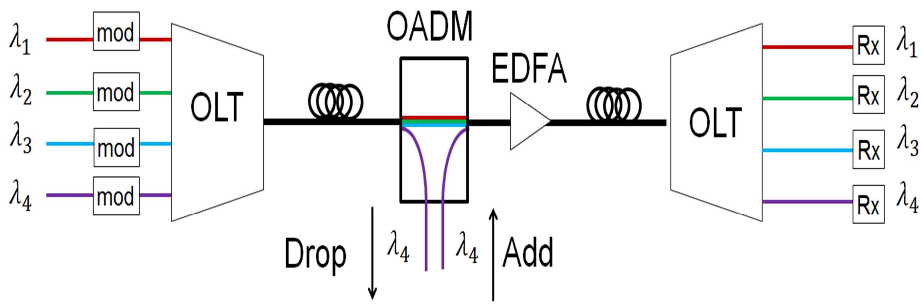

Figure 2.2: WDM transmission system.

Metro networks are described in [5, 7] . In this scheme, carriers are modulated with data signals of 10Gbit/s, 40Gbit/s or even up to 100Gbit/s and multiple carriers at different wavelengths are sent down the fibre simultaneously. Optical line terminals (OLTs) can be used to join different data sources at different wavelengths together and also separate them at their destination. With appropriate design, the carriers can remain independent of each other. Using devices such as optical add/drop multiplexers (OADMs) it is possible to remove specific wavelengths at points along a link and to also add wavelengths with local data to the link. It can be seen that since the data is multiplexed using different wavelengths it is relatively straightforward to manage and route data using filters and OADMs. Routing data through a network based on wavelength is known as wavelength routing. The optical power of the signal will be attenuated if the signal travels over long distances (even with attenuation coefficients which can be below 0.2dB/km [8]). Depending on the link length and other considerations it may be necessary to amplify the optical signal which can be done by deploying one or more erbium doped fibre amplifiers (EDFAs) along the link. The paths that are end-to-end connections between source and destination are referred to as lightpaths [7, 9]. Initially, optical communications used only basic modulation formats to encode data onto optical carriers such as on-off keying (OOK). However, it is possible to further increase spectral efficiency in optical networks by transmitting data using higher-order modulation formats such as M-ary quadrature amplitude modulation (QAM) and polarisation-multiplexed transmission systems.

2.1.2 Possible Future Metro Networks

As discussed in the previous section, data can be routed between two points in a metro network via wavelength. These lightpaths can be fixed or varied dynamically. When these lightpaths are fixed or varied with long reconfiguration times, this is referred to as optical circuit switching (OCS).

When lightpaths are varied on the order of microseconds or nanoseconds it is referred to as either optical burst switching (OBS) or optical packet switching (OPS). Advantages associated with OBS and OPS are that the virtual circuits in the network can be reconfigured very quickly with changing data patterns. In addition, OBS and OPS allow for data not destined for a node to pass through intermediate nodes which will eliminate converting the data into the electrical domain, processing it and converting it back into the optical domain to be sent onto the next node in the ring, with similar arguments made in [10]. This reduction in processing could potentially lead to a reduction in the power consumption of the network. Here are two key distinguishing factors between OPS and OBS. Firstly, OBS tends to send bursts of aggregated packets together while OPS tends to send packets of finer granularity. Secondly, OPS headers are contained within the packet while OBS does not require headers to be sent with the bursts but instead OBS reserves bandwidth by sending its control data before sending the payload burst [11].

While the focus of the thesis will be on ring metro networks, it is worth mentioning that OBS networks can be potentially implemented in a general mesh network in the following manner. OBS networks can operate on the basis that headers are sent out before the payload, with the headers being processed at the nodes so that the nodes can be configured in advance to process the data and also to reserve bandwidth/ time slots with the node [12]. It may be necessary to use buffers in the network, usually of the form of optical delay lines, in case two or more bursts are being sent to the same node at the same time. This approach can reduce the number of times the payload will need to be converted into the electrical domain with only the header needing to be processed electronically. This reduces power consumption in the network by having less electronic processing functions taking place in the network. Note that another different application in which switching tuneable lasers and burst receivers could be used is with arrayed waveguide gratings to create routers which use optical switch fabrics instead of electrical switch fabrics, which could potentially reduce power consumption and costs [13]. However, in this work the focus will be on implementing OBS or OPS in a ring network which allows for a simplified network architecture where it is possible to have all the electronic processing occurring only at the source and destination of the optical packets and not at any of the intermediate nodes. This type of network will be explained more fully next.

2.1.2.1 Description of Optical Packet/ Burst Switched Ring Networks

Shown in Figure 2.3 below is an example of an optical packet/ burst switched ring network.

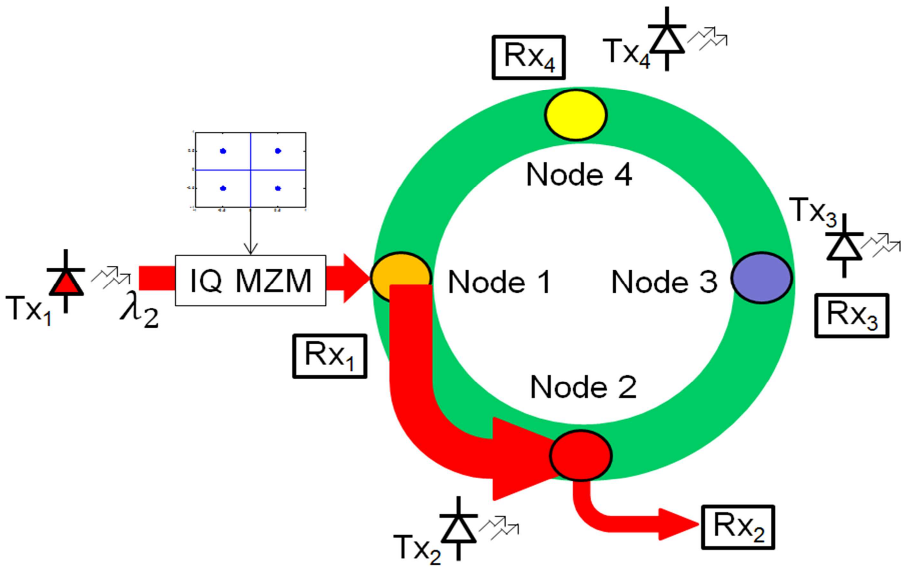

Figure 2.3: Optical packet/ burst switched ring network.

At each node is a tuneable laser transmitter (labelled "Tx"), a modulator and a receiver (labelled "Rx"). In order to send data to a particular node, the transmitter changes its wavelength to the wavelength associated with the destination node when the destination's wavelength becomes free (i.e. is not being used by another transmitter). The transmitter carrier is then modulated at this new wavelength. The modulated signal is then sent into the ring network. At the destination some form of OADM can be used to drop the required wavelength. In the case of direct detection, each receiver will decode data at a fixed wavelength. Initially, intensity modulation, such as non-return-to-zero (NRZ) [14-16], was typically used with tuneable lasers in order to transmit data. This means that issues due to variations in the frequency of the transmitter would not have had as severe an impact on performance as would be the case for phase modulated data. This simplifies the receiver design where the receiver can potentially consist of simply a photodiode, some method of chromatic dispersion compensation and some additional electronics to cope with optical power variations. In addition, the modulator required would be just a single Mach-Zehnder modulator (MZM) which is described in section 2.2.3.1. However, a key limitation with using OOK is its poor spectral efficiency.

2.1.2.2 Higher-Order Modulation Formats in Optical Packet/ Burst Switched Networks

In this thesis, external modulation is used to send some form of coherent modulation format such as differential quadrature phase shift keying (DQPSK) or dual-polarisation DQPSK (DP-DQPSK) to further increase spectral efficiency and throughput. Instead of using an OADM to tap off the signal from the ring network, a splitter can be used to tap off some power where the polarisation-diverse coherent receiver selects data at the wavelength at approximately equal to the wavelength of the local oscillator (LO) used in the polarisation-diverse coherent receiver. However, a method of filtering out the selected wavelength would need to be employed to prevent it from continuing through the ring. The polarisation-diverse coherent receiver down-converts the received optical signal to a baseband electrical signal, since the LO and transmitter are expected to be at approximately the same wavelength (details of the polarisation-diverse coherent receiver are given in a section 2.2.4.2). Some residual frequency offset is expected to still remain and this needs to be compensated. Digital signal processing (DSP) is then performed on the received signal in order to remove and mitigate the effects caused by channel impairments such as chromatic dispersion.

The architecture used here has a tuneable transmitting laser and a fixed wavelength LO. Note that an alternative architecture is to have a switching tuneable laser at the LO which can select data from particular wavelengths where the data is transmitted using fixed wavelength lasers [10]. The choice of which architecture to use may be influenced by the protocol systems preferred at higher levels where perhaps having both tuneable transmitters and tuneable receivers might be preferred. In any case, the work undertaken in this thesis (i.e. characterising phase dynamics of tuneable lasers after switching, compensating for large/ changing frequency offsets and fast polarisation demultiplexing) applies to all these architectures. However, in this work tuneable transmitters and fixed receivers will be used as this architecture provides a clear mechanism for the transmitter to route data to its destination.

There are two challenges with using phase modulation with fast switching tuneable lasers. Firstly, there are frequency transients after a switch which, if not dealt with correctly, can result in errors. Secondly, there is a need to use DSP which is able to mitigate channel impairments quickly after receiving a burst. The first challenge is dealt with in chapter 5. With regard to the second challenge, it was stated in [4] that the length of IP packets at 40 Gbit/s can vary between 13ns and 500ns (equivalent to between 520 bits and 20,000 bits). Waiting times after a switching event for dual-polarisation quadrature phase shift keying (DP-QPSK) have been published and these are prohibitively large for IP packets over these time scales. In one example [10], the system has variable convergence times (maximum convergence time is 200ns or 44,800 bits with a bit rate of 224 Gbit/s). In another example [17], the maximum convergence time is approximately 410ns or 45,920 bits with a bit rate of 112 Gbit/s. This waiting time issue is dealt with in this thesis by using a 40 Gbit/s dual-polarisation doubly differential quadrature phase shift keying (DP-DDQPSK) system where a waiting time of 30ns or 1,200 bits is achieved [18]. This greatly improves the efficiency of coherent OPS systems and is discussed in detail in chapter 6. If packets are aggregated together in a coherent OBS system, the efficiency improvements achieved here become less significant as burst sizes increase.

2.2 Devices

In order to implement a coherent OPS/ OBS network, it is necessary to use (i) tuneable lasers, (ii) external modulators and (iii) polarisation-diverse coherent receivers. These three device categories are relevant to the advances reported in this thesis and the background behind these devices will be explained next. It will be assumed that the reader has basic knowledge and familiarity with other devices such as filters and EDFAs (with many of these devices discussed in [7]).

2.2.1 Lasers

A laser is a light source which produces a spectrally pure source of light. Lasers are devices which typically have the following features: (i) a cavity for feedback (ii) a gain medium (iii) a method of filtering light. Lasers which are typically used in telecommunications are semiconductor lasers which are known for their ruggedness, low cost and small size [19].

2.2.1.1 Wavelength

It is important to understand the factors which determine the output wavelength of a laser. A simple example of a laser is a Fabry-Pérot resonator [20]. Consider a Fabry-Pérot resonator, where the cavity provides both gain, g (gain per unit length) and attenuation, α_s (loss per unit length) as shown in Figure 2.4 [20]. The two mirrors of the cavity have reflection coefficients r_1 and r_2 for mirror 1 and mirror 2 respectively. As shown in the diagram, the field will have reflection coefficients multiplying with it. Also, gain and attenuation terms will need to be taken into consideration as well as the phase term relating to the propagation constant, β.

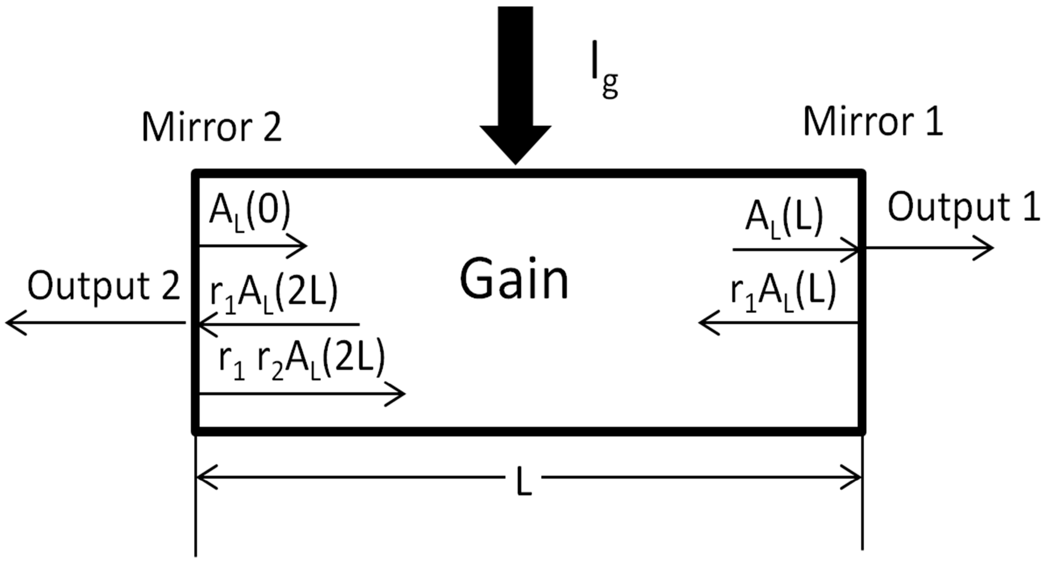

Figure 2.4: Simple example of a laser [20].

The plane wave moving through the cavity, $E(t,x)$, is given as (similar to that given in [20]):

$$E(t,x) = A_L(x)e^{j\omega t} \tag{2.1}$$

where $A_L(x)$ is given by[20]:

$$A_L(x) = Ae^{(-(\alpha_s - g)x/2)}e^{-j\beta x} \tag{2.2}$$

where ω is the angular frequency of the wave, x is the distance from the left mirror, A is the amplitude of the wave at x=0 and t is time.

In [20], it is shown that the wavelengths of light, λ, which will be generated are given by equation (2.3):

$$\lambda = \frac{2nL}{m_1} \tag{2.3}$$

where n is the refractive index of the cavity, L is the length of the cavity and m_1 is a non-zero, positive integer. A value of λ which satisfies equation (2.3) is referred to as a mode. Note also the difference in wavelength between adjacent modes will be [20]:

$$\Delta\lambda = \frac{\lambda^2}{2nL} \tag{2.4}$$

In order to use lasers in conjunction with EDFAs the wavelength of the laser will need to be within the 35nm bandwidth of the EDFA in the 1550nm region of the spectrum [7].

2.2.1.2 Side-Mode Suppression Ratio

Single-mode operation of a laser is preferred in telecommunication applications in order to reduce the effects of dispersion. Hence, only one lasing mode should be produced with the others suppressed. The parameter side-mode suppression ratio (SMSR) is the power ratio between the dominant mode and the next highest power mode. For the sampled grating distributed Bragg reflector (SG-DBR) laser, which will be discussed in section 2.2.2.4, an SMSR in excess of 50dB can be achieved [21]. One method of supressing modes is to use a Bragg grating.

2.2.1.3 Bragg Gratings

Bragg gratings are essentially multiple partially reflecting mirrors which, when combined, result in a strongly reflecting mirror [20]. In practice, this can be achieved by using a periodically varying refractive index of the medium used [22], similar to what is shown in Figure 2.5.

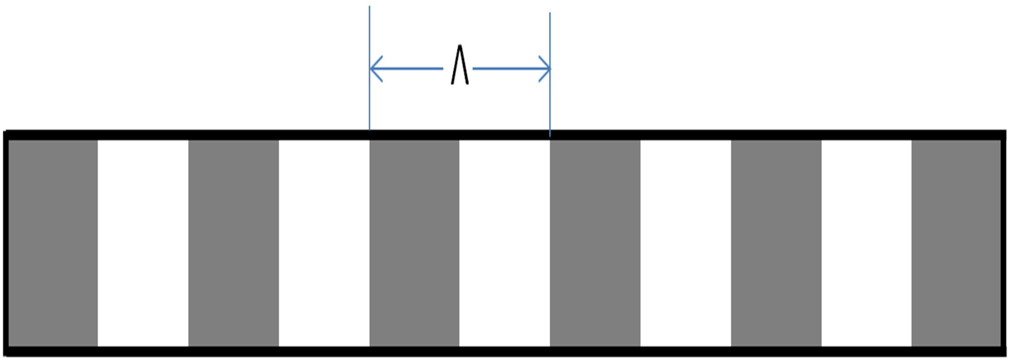

Figure 2.5: Schematic diagram of a Bragg grating with grey and white sections indicating different refractive indices (similar to a figure in [22]).

For an incident angle, θ_i, the refracted angle, θ_r, is given by [22]:

$$\sin\theta_i - \sin\theta_r = \frac{m\lambda}{\bar{n}\Lambda} \quad (2.5)$$

where m is the order of Bragg diffraction, λ is the wavelength of light, $\bar{n}$ is the average refractive index and Λ is the spacing between two planes of equal refractive index [22]. For normal incident light, with $\theta_i = \pi/2$ and $\theta_r = -\pi/2$, equation (2.5) reduces to:

$$2\bar{n}\Lambda = m\lambda \quad (2.6)$$

where any λ satisfying equation (2.6) is a reflected wavelength. Hence, the use of a Bragg grating in a laser cavity such as in a distributed feed-back (DFB) laser or distributed Bragg reflector (DBR) laser will mean that only modes which satisfy equation (2.6) will be produced. This will result in suppression of other modes, thereby achieving high SMSR. It is clear that by tuning the refractive index then the reflecting wavelengths in equation (2.6) can be changed. This will be important when tuneable lasers are discussed in later sections.

2.2.1.4 Output Power

Another parameter which is important is output power. High output power can potentially reduce the number of EDFAs used in a transmission link and, due to the use of external modulators which typically have loss, high output power from the transmitting laser is required. Laser output power will be dependent on the efficiency of the laser to convert the injected carriers into photons. An analytic expression for the output power, P, is given in [23]:

$$P = \eta_{in} \frac{h\nu}{e} \frac{\alpha_{mir}}{\alpha_{tot}} (I - I_{th}) \ , \ (\text{for } I > I_{th}) \tag{2.7}$$

where h is Plank's constant, ν is the frequency of light, e is the charge of an electron, α_{mir} is the mirror loss (α_{mir}=(1-r)), α_{tot} is the loss in the cavity plus the mirror loss, I is the laser current, I_{th} is the threshold current and η_{in} is the internal quantum efficiency. As an example, the SG-DBR laser can produce output power levels of +2.6dBm and +4.0dBm [21].

2.2.2 Noise in Lasers

2.2.2.1 Relative Intensity Noise

In a semiconductor laser, or indeed in any laser, the three main processes controlling the field (and amplitude) of the laser are: (i) absorption, (ii) stimulated emission and (iii) spontaneous emission, which are explained in [7] but in the context of amplifiers. Absorption is where a carrier is excited to a higher energy by a photon arriving at an appropriate frequency but the photon is then lost/absorbed [7]. Stimulated emission is where a carrier drops from a higher energy to a lower energy after being "stimulated" by a photon of an appropriate frequency which results in the emission of an additional photon of the same energy as the input photon [7]. Spontaneous emission is when a carrier drops to a lower energy independent of any external radiation and is termed as an incoherent process as the resulting photon has a random direction, phase and polarisation [7]. This is unlike stimulated emission where the resulting photon has the same phase, direction of propagation and polarisation as the incident photon [7]. The stimulated emission process is crucial in order to generate a spectrally pure output.

Spontaneous emissions result in noise that appears on the output of a laser, causing randomly varying amplitude and phase [20]. The field of the output of the laser, $E(t)$, can be expressed as (similar to that given in [20]):

$$E(t) = A[1 + n_a(t)].\cos[\omega t + \Phi_n(t)] \tag{2.8}$$

where A is the amplitude of the field, ω is the angular frequency of the field, $n_a(t)$ is the amplitude noise and $\Phi_n(t)$ is the phase noise.

Relative intensity noise (RIN), is a measure of the amplitude noise and is defined as [20]:

$$R_n = 10\mathrm{Log}_{10}[\zeta] \tag{2.9}$$

Where R_n is the RIN, ζ is the power spectral density of $2n_a(t)$, where ζ has units of 1/Hz. A good laser would have a RIN better than -165 dB/Hz [20]. Note that as losses increase from external sources, e.g. during transmission, shot noise has an increasing effect on the detected RIN [24].

2.2.2.2 Phase Noise

The phase noise, $\Phi_n(t)$, from equation (2.8) above, is typically modelled as a Wiener process. A Wiener process, $f(t)$, is where the power spectral density (PSD) of the derivate of $f(t)$ (i.e. $\dot{f}(t)$) is a zero-mean white Gaussian process and that [16]:

$$f(t) = \int_0^t \dot{f}(\tau).d\tau \tag{2.10}$$

The PSD of $\dot{\varphi}_n(t)$, the derivative of $\Phi_n(t)$, in the case of a laser is expressed as:

$$PSD[\dot{\Phi}_n(t)] = 4\pi\Delta\nu \tag{2.11}$$

where $\Delta\nu$ is called the linewidth or full-width half-maximum (FWHM) linewidth [20]. It was shown in [25] that an analytic formula for the linewidth can be given as:

$$\Delta\upsilon = \frac{v_g^2.h.\nu.g.n_{sp}.\alpha_m.(1+\alpha^2)}{8\pi P_0} \tag{2.12}$$

where v_g is the group velocity, h is Plank's constant, ν is the frequency of light, g is gain per unit length, n_{sp} is the spontaneous emission factor, α_m is the difference between gain and loss per unit length, α is the coupling factor between changes in the real and imaginary refractive indices ($\Delta n'/\Delta n''$) and P_0 is the output power per facet. The origin of the linewidth is from spontaneous emissions as discussed above, however, the phase noise is exacerbated by coupling between the intensity and phase changes caused by spontaneous emission events which lead to the linewidth enhancement factor $(1+\alpha^2)$ in equation (2.12). It is also clear from equation (2.12) that higher output powers can reduce the linewidth of the laser.

Note that linewidth is a key limiting factor in coherent communications using phase modulation, e.g. a BER of 10^{-3} for a DQPSK system at 10GBaud requires a linewidth of less than 3MHz to have a penalty of less than 0.1dB [26].

Two examples of a semiconductor laser are DFB lasers and DBR lasers [20]. DFB lasers have the gain medium covering the entire length of the cavity and a Bragg reflector covering the same region except for a small length equal to one quarter of the wavelength [20]. The DBR laser separates the gain section and Bragg reflector sections. One advantage of the DFB over the DBR is that DFBs are easier to fabricate as they do not have separate active and passive sections [24]. However, the DFB laser cannot vary its gain and grating sections separately since these sections overlap. The DBR by contrast can vary the gain and grating sections independently.

2.2.2.3 Tuneable lasers

Tuneable lasers are lasers where the wavelength of the output light can be varied. This is useful from the point of view of inventory, where only one type of laser needs to be kept in reserve in case lasers in the network fail, therefore, providing a useful function for OCS networks. As can be seen from the discussion on networks, tuneable lasers are an essential component in the OBS/ OPS networks in order to provide dynamic wavelength paths. A comprehensive discussion on tuneable lasers can be found in [27].

There are many different mechanisms which can be used to tune the output wavelength. Firstly, mechanical methods [27] can be used such as in an external cavity laser (ECL) [28]. Secondly, thermal variations [27] change the refractive index of the laser cavity, which leads to variations in the mode wavelength (see equation (2.3)) and, hence, changes the output wavelength. Also, by changing the electronic current going through the sections of the laser [28] the refractive index of one (or more) sections of the tuneable laser can be varied resulting in a change in wavelength. Physical descriptions of how this occurs are given in [29] which discusses the free-plasma effect. Since changing electronic currents can be done in the order of nanoseconds, this type of tuning mechanism is a suitable candidate for optical packet switched network applications.

2.2.2.4 SG-DBR Lasers

The tuneable laser which was used throughout the experiments performed in this thesis was the SG-DBR laser. The tuning mechanism used in SG-DBR lasers is current tuning. It should be noted that the SG-DBR laser used in the experiments in this thesis did not have a semiconductor optical amplifier (SOA) section or any gain section other than the gain section between the phase and front mirror sections as shown in Figure 2.6 [27]. An advantage of having an SOA section is that the amplitude of light from the laser can be controlled more easily [27]. The phase section is used for additional control of the wavelength [27], where the phase section can make precise wavelength adjustments. SG-DBR front and back mirrors consist of sampled Bragg gratings which are periodically placed in these sections [30]. These result in a periodic reflection spectrum which can be tuned by varying the currents applied to these sections which changes refractive index.

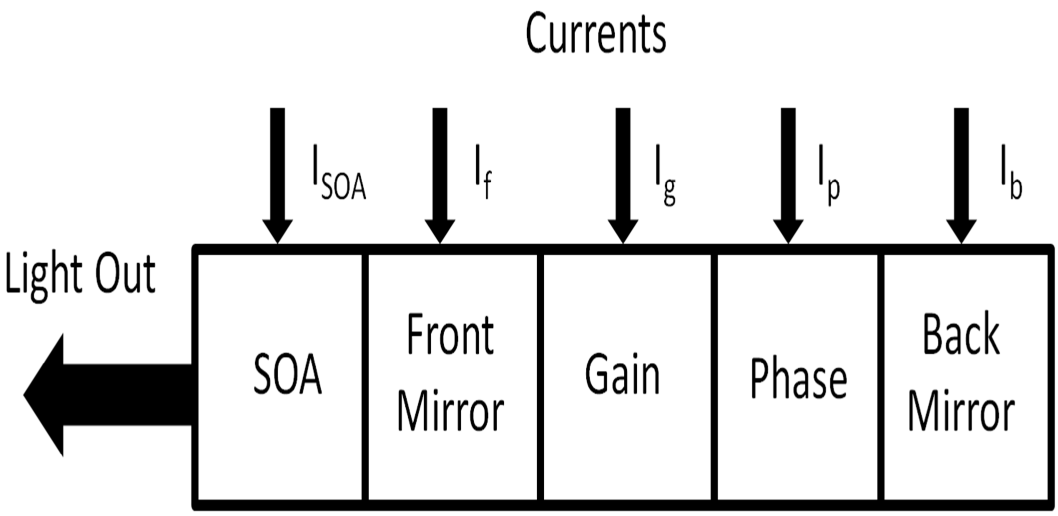

Figure 2.6: Laser schematic diagram of a typical SG-DBR [27].

It should be noted that while current tuning on its own provides a limited tuning range, the tuning range of the SG-DBR can be extended by appropriate design of the front and back mirrors as will be described next. A key aspect of the SG-DBR laser is that front mirror and back mirrors have different spaces between reflectivity peaks. In addition, only wavelengths which are reflected by the front and back mirrors will be continuously amplified in the cavity. This means that the only wavelengths which can be lasing wavelengths must have coinciding reflection peaks at the front and back mirrors. The fact that mirror peak reflection peaks have different spaces means that there are a large number of possible wavelengths to tune to. This is sometimes referred to in the literature as the Vernier effect [27]. The Vernier effect allows for a much larger tuning range in spite of the limited range achievable by current tuning alone. As is shown in [31], it possible to tune to 85 different wavelengths with 50GHz spacing and SMSR values greater than

40dB, demonstrating a large tuning range, with a spectrum of possible wavelength channels given in [31] presented here in Figure 2.7 (Figure 2.7 is taken from [31]).

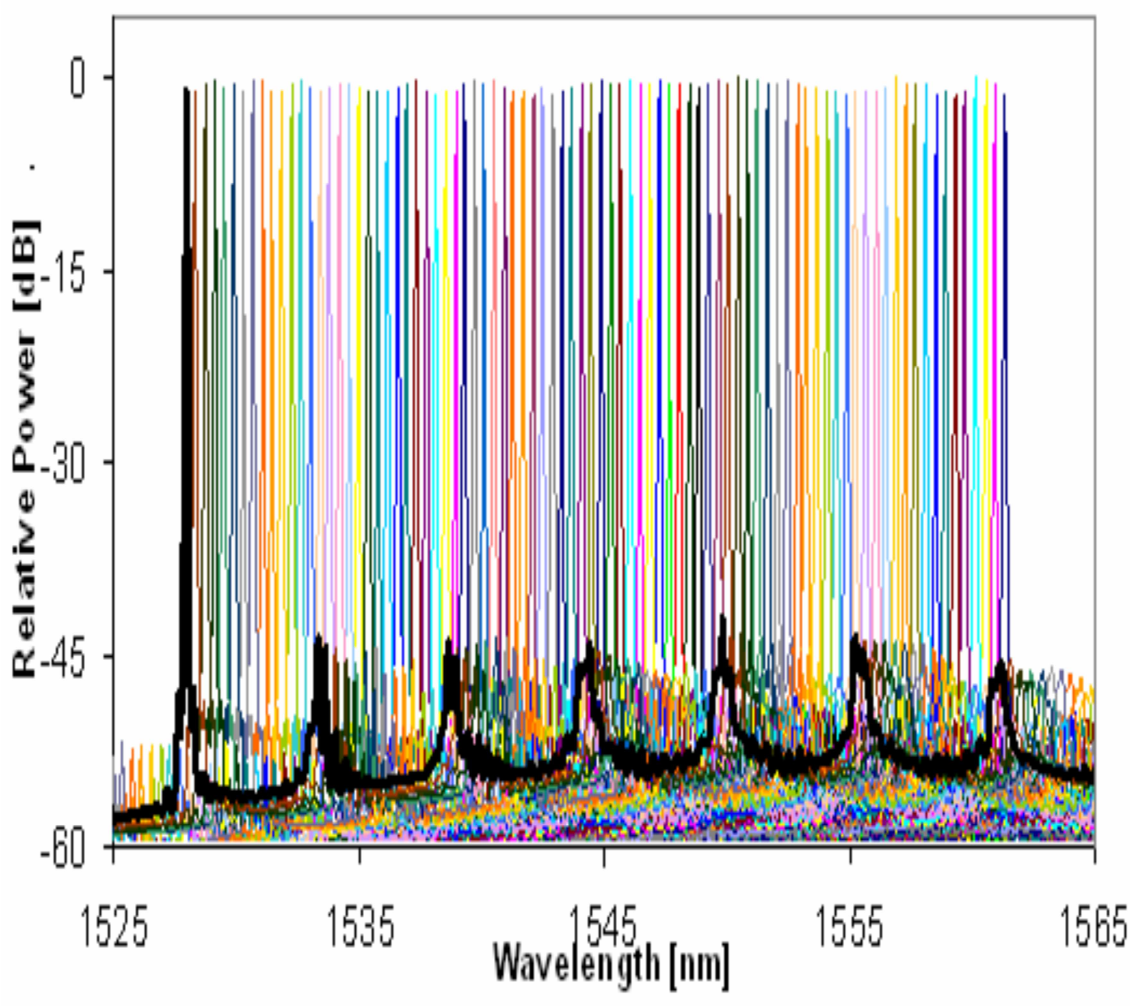

Figure 2.7: Overlapping spectra of different possible wavelength channels for an SG-DBR laser, consisting of 85 channels separated by 50GHz, and with SMSR values greater than 40dB (this figure was taken from [31]).

In terms of performance, the SG-DBR laser is capable of producing SMSRs greater than 50dB at output powers greater than 2.6dBm but may have large variations in linewidth, with linewidths of 4.6MHz and 19.8 MHz both possible at the same wavelength but with different bias settings [21]. It is also possible to quickly switch between wavelengths using the SG-DBR laser. However, frequency transients can occur directly after a switching event which affects the performance of phase modulation schemes. This is A switching transient occurs when the back section of the SG-DBR laser has a square wave applied to it as presented in Figure 2.8 [32].

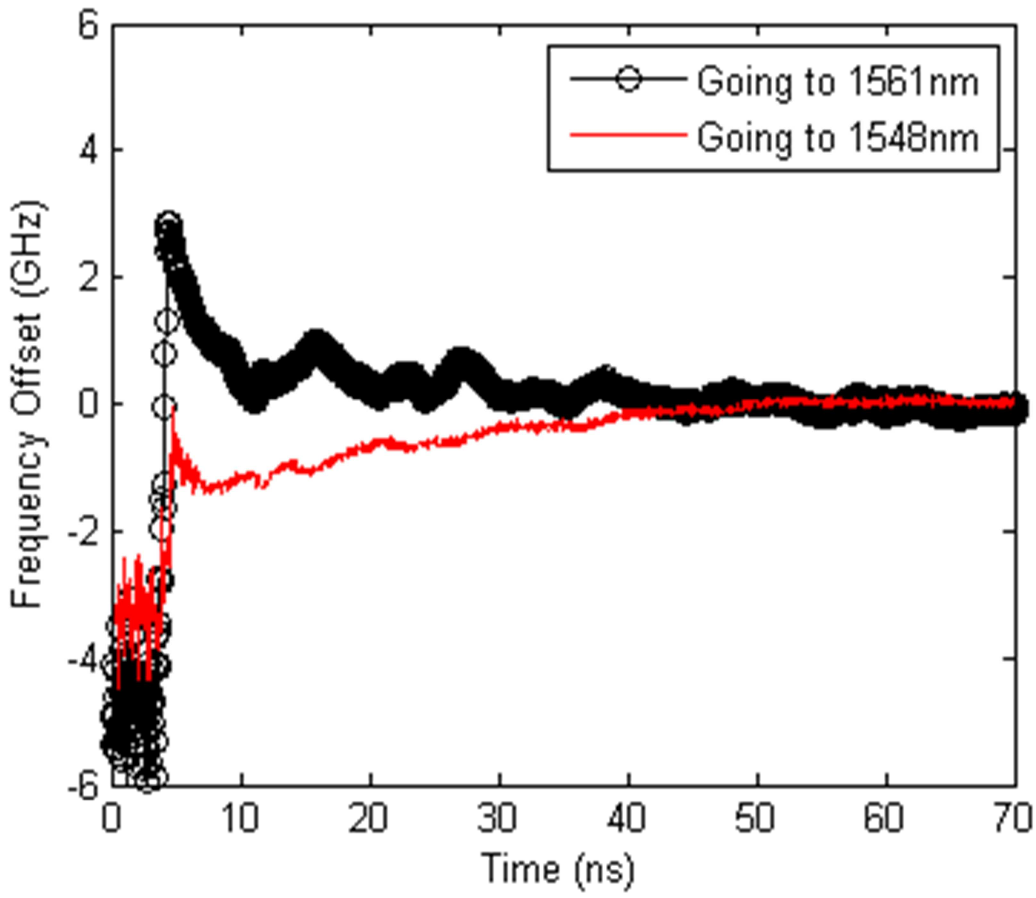

Figure 2.8: Switching frequency offset versus time for switching SG-DBR (slight alteration of the figure in [32]).

Among the key concerns when performing fast switching with a multi-section tuneable laser, like the SG-DBR, are the excitation of other unwanted modes, the frequency transients directly after switching, and increases in phase noise after switching. Simulations of the effects of switching on output power and SMSR have also been carried out [30] which demonstrate the potential for other modes to appear during the switching process as well as a settling time being required to allow the laser output to stabilise at the destination mode. Therefore, it may be necessary to introduce a blanking period immediately after a switch to ensure that spurious modes are not transmitted.

A scheme to reduce the transients in fast switching tuneable lasers has been suggested in [33]. By applying switching voltages with pre-emphasis to the rear section of a digital supermode distributed Bragg reflector (DS-DBR) laser and by applying compensating transient signals to the phase section, the laser will settle sooner after switching. This scheme has been shown to result in large decreases in frequency transients [33] , allowing for dual-polarisation quadrature phase shift keying (DP-QPSK) data to be decoded within 125ns after switching (100ns wait after the switching plus 25ns constant modulus algorithm (CMA) convergence time). However, there is added complexity in terms of calibrating the pre-emphasis signals and applying pre-emphasis signals to the phase and rear-mirror sections.

Also, characterisations of the variations in linewidth after a switching event suggest that the linewidth of the SG-DBR laser decreases to less than an order of magnitude from its steady-state value within 15ns after a switching event [34] (note that this work was done contemporaneously with the research published here). However, more analysis on the frequency and phase noise dynamics will be provided in a later chapter.

2.2.3 Modulation

In order to transmit data, the laser light must be modulated. This means that properties of the light generated by the laser, such as its power, phase or polarisation must be varied in response to electrical data, and so that these variations can be interpreted at the receiver to determine the original message. Two types of modulation in optical communication are direct modulation and external modulation. In direct modulation, the laser's currents are typically varied in order to change the output laser frequency or power [19], e.g. high power to indicate a "1" and low power to indicate a "0". A key advantage of this method is lower equipment cost compared with using external modulation devices. A key disadvantage of direct modulation is that it typically introduces frequency chirp which can result in large penalties from dispersion [7]. Frequency chirp is defined as variations in the instantaneous frequency as a function of time. Direct modulation can be used to implement higher-order modulation formats as demonstrated recently [35], however, this requires the use of more than one laser. External modulation, which will be described next, can be used without requiring a full characterisation of a laser's frequency response, can be implemented using only a single transmitting laser, does not have the severe frequency chirp issue and, due to the fact that the transmitting laser will be switching wavelengths, external modulation is a more straightforward method of performing the modulation process. Two disadvantages of external modulation are the costs of having an additional external modulation device and also the loss in optical power after going through an external modulation device such as a Mach-Zehnder modulator (MZM).

2.2.3.1 External Modulation and the Mach-Zehnder Modulator

External modulation can be performed by various different devices. In this thesis, the key device used for performing external modulation is the Mach-Zehnder modulator (MZM), with a schematic diagram of the MZM shown in Figure 2.9 below. A MZM is typically made of Lithium Niobate [36], where its refractive index can be altered by applying a voltage across it, with a linear relationship between refractive index and voltage. The phenomenon exploited is known as the Pockels effect [36]. When light enters to the MZM, it is split into two paths. By varying the refractive index in one or both paths, the delay the wave(s) experience varies. This can result in constructive or destructive interference when the waves are recombined.

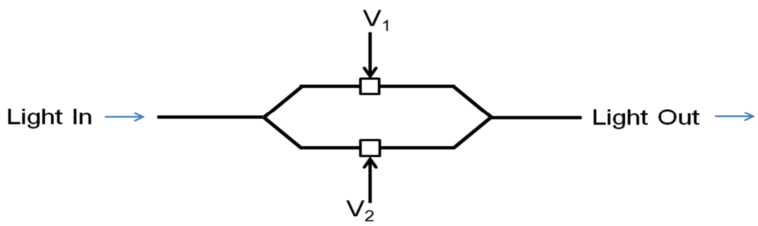

Figure 2.9: Schematic diagram of a MZM [8].

The transfer function of the MZM, $T_{MZM}(V_1,V_2)$, (i.e. the output field divided by the input field) is given by (similar to equation (1) in [8] but including an insertion loss term, α_{MZM}):

$$T_{MZM}(V_1,V_2) = \alpha_{MZM}\, e^{j(\Phi(V_1)+\Phi(V_2)+\psi)/2} \\ .\mathrm{Cos}\left[(\Phi(V_1)-\Phi(V_2))/2-\psi/2\right] \tag{2.13}$$

where V_1 and V_2 are the applied voltages shown in Figure 2.9, ψ is a constant phase delay and the phase delay function, $\Phi(V)$, is governed by [8]:

$$\Phi(V) = \kappa V \tag{2.14}$$

where κ is a constant. By appropriate electrode design it is possible to drive the modulator with only one signal and have $V_1(t)=-V_2(t)$ so that chirp-free performance can be achieved [8]. An important parameter, denoted as V_π, is the change in voltage required in a single arm to give a π phase change in that arm [8]. Letting:

$$\Delta V = V_1 - V_2 \tag{2.15}$$

V_π is the change in ΔV necessary to go from maximum to minimum optical output power. $2V_\pi$ is required to switch between two maximum transmission peaks but with a π phase difference between the two output fields. The MZM shown in Figure 2.9, using only one drive signal and having $V_1(t)$=-$V_2(t)$, can modulate a laser with OOK and binary phase shift keying (BPSK).

Two MZMs can be combined to form an IQ modulator as shown in Figure 2.10 below. This modulator is capable of performing quadrature phase shift keying (QPSK) modulation as the phase in the lower arm is shifted by 90^o as well as M-QAM. Other possible modulator configurations for generating constellations such as 16-QAM are suggested in [37]. In addition to this it is possible to combine two IQ modulators to modulate two polarisations of light using a polarisation multiplexed IQ modulator as shown in Figure 2.11. Note that in Figure 2.10, a DC bias voltage is used on each arm to essentially compensate for the ψ in equation (2.13) and the V_{RFI} and V_{RFQ} inputs are the high speed data signals modulating the data. Note that in Figure 2.11 only the RF signals are shown and the DC bias voltages are omitted.

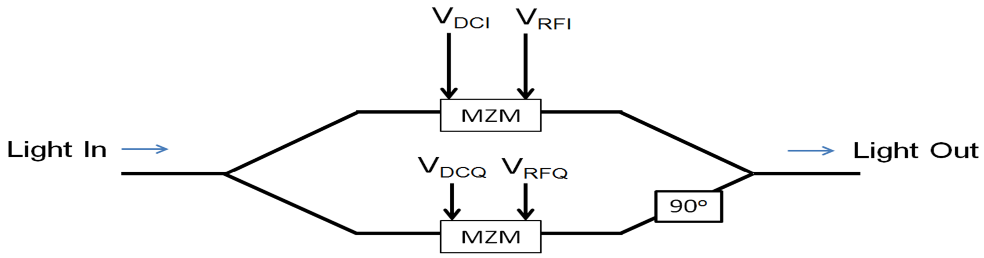

Figure 2.10: Schematic diagram of an IQ modulator [8].

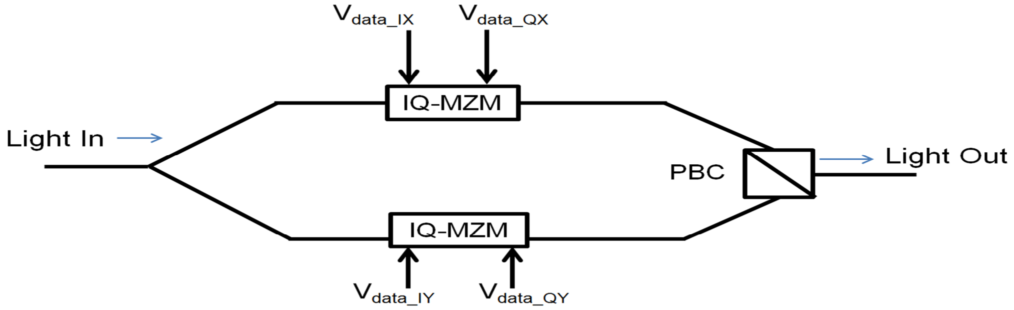

Figure 2.11: Schematic diagram of a polarisation multiplexed IQ modulator [38].

2.2.3.2 Higher Order Modulation Formats

Using the modulators described in section 2.2.3.1, different modulation formats can be generated. In optical communications, information can be sent by varying one or all or the following; amplitude, phase and polarisation. Frequency (or wavelength) is used to multiplex data as described above in the WDM paradigm. However, small frequency deviations can be used to implement frequency shift keying.

The modulator shown in Figure 2.9 is known as an intensity modulator but is also essentially an amplitude modulator since it can reduce the input field by an arbitrary amount and can also make the sign of the wave to be positive or negative. When the amplitude of the field is modulated so that it either has zero amplitude, or a particular non-zero amplitude, this is referred to as OOK. When the field is modulated so that it has the same power for both 1 and 0 but has either a 0^o or 180^o phase shift this is referred to as BPSK. Both these modulation formats only send one bit per symbol. These two modulation formats are illustrated using constellation diagrams that are shown in Figure 2.12 below. The number of bits per symbol, M_b, is calculated via:

$$M_b = \log_2\left(N_{sym}\right) \tag{2.16}$$

where N_{sym} is the number of symbols used in the modulation format.

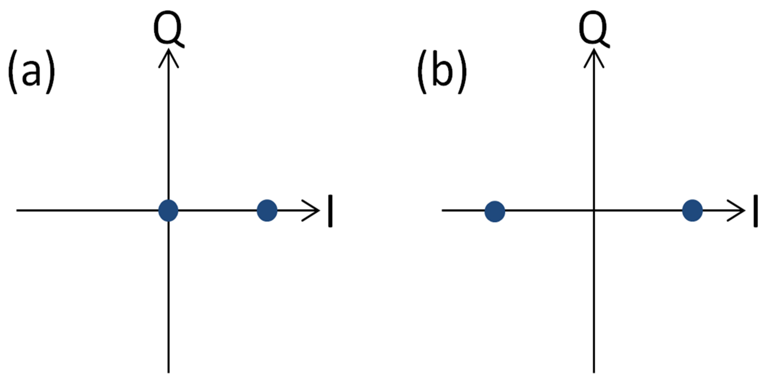

Figure 2.12: Constellation diagrams of (a) OOK and (b) BPSK.

Since the modulation formats shown in Figure 2.12 only send one bit per symbol, it is of interest to look at modulation formats which send a larger number of bits per symbol as this can be used to increase spectral efficiency. The IQ modulator shown in Figure 2.10 above modulates a sine wave and cosine wave independently which means there is an extra degree of freedom compared with the intensity modulator in Figure 2.9. Examples of the modulation formats which can be generated with this modulator are QPSK and 16-QAM as shown in Figure 2.13 below and it can be seen the number of bits per symbol are 2 and 4 respectively.

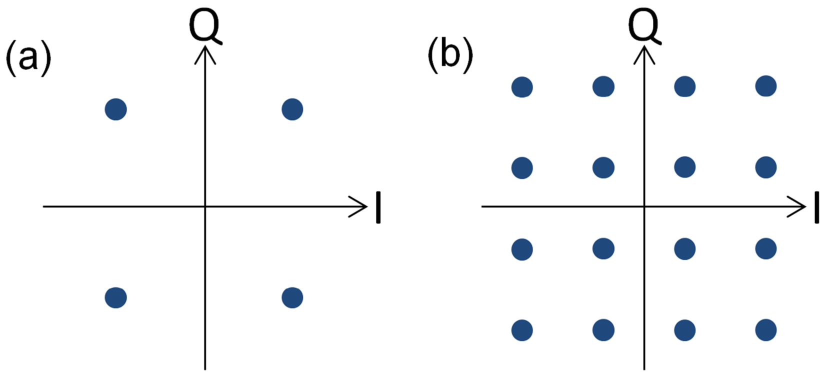

Figure 2.13: Constellation diagrams of (a) QPSK and (b) 16-QAM.

In addition, it is possible to add another degree of freedom by modulating data on two different polarisations by using a polarisation-multiplexing-IQ-modulator as shown in Figure 2.11 above. Modulation formats such as DP-QPSK or dual-polarisation 16-QAM can be generated which have 4 bits per symbol and 8 bits per symbol respectively. Phase recovery for general M-QAM is presented in [39]. It is also possible to generate polarisation QAM modulation systems which not only use polarisation multiplexing both also take advantage of the ability to send QAM signals on single polarisations to increase throughput [40].

All these modulation formats will experience various impairments as they travel through a fibre optic cable such as attenuation, chromatic dispersion, polarisation rotations, etc. Hence, it is a key function of the receiver to compensate/mitigate the effects of these impairments on the received signals so that the data can be correctly recovered.

2.2.4 Optical Communication Receivers

The key device for receiving optical communication data is the photodiode. The photodiode converts received photons into electrons which allows for either direct determination of the data sent, in the case of OOK, or can be used in conjunction with other optical devices, other photodiodes and DSP to demodulate data transmitted using amplitude, phase and/or polarisation modulation. In this thesis, phase modulation and polarisation modulation will be the key focus. Two widely used methods for demodulating phase shift keying (PSK) data are (1) delay interferometers and (2) coherent receivers. These methods will be described next.

2.2.4.1 Delay Interferometers

An example of a delay interferometer receiver setup is shown in Figure 2.14 below [41]. Note that this receiver is designed to demodulate signals that use differential binary phase shift keying (DBPSK), where data is encoded on phase changes. Here, the incoming signal field, $E_{RX}(t)$, is split into two parts, where one arm is delayed in time, then both parts are recombined and have their coupled outputs detected by balanced photodiodes. The electrical signal, $I_{PD}(t)$ is given by [41] (assuming that the amplifier has a finite, but high common mode rejection ratio, the following equation will apply):

$$I_{PD}(t) = \mathrm{Re}[K.E_{RX}(t)E^{*}_{RX}(t-T)] \tag{2.17}$$

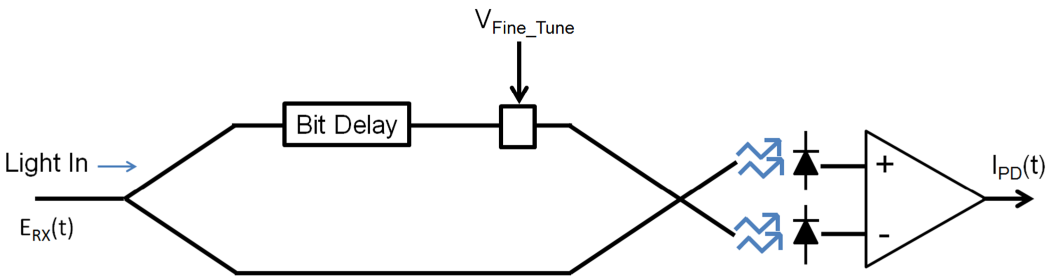

Figure 2.14: Delay interferometer receiver [41].

where T is the relative time delay between the upper and lower arms and K is a proportionality term that will be present (however K is not included in [41]). Not considering noise terms, $E_{RX}(t)$ will be of the form:

$$E_{RX}(t) = Ae^{j\omega t + \Phi_{mod}(t)} \tag{2.18}$$

where A is amplitude, ω is angular frequency and $\Phi_{mod}(t)$ is the phase modulation. Hence, it can be show that equation (2.17) now becomes:

$$I_{PD}(t) = KA^2 \cos[\omega T + \Phi_{mod}(t) - \Phi_{mod}(t-T)] \tag{2.19}$$

In Figure 2.14, the “Bit Delay” refers to a coarse delay which is set to be equal to the bit period of the received DBPSK signal. The precise delay, set by V_{fine_tune}, must implement a very small and precise time delay change, of the order of femtoseconds so that the ωT term in equation (2.19) is equal to a multiple of 2π. As a result of this, $I_{PD}(t)$ gives a positive value for zero phase changes and a negative value for π phase changes resulting in correct demodulation of DBPSK. It is then possible to combine and configure various delay interferometers in order to demodulate differential M-ary PSK signals. Note that the “Bit Delay” should then be set to the symbol period for M-ary PSK demodulation. One key advantage of this system is that it does not require a LO as in the case of the coherent receiver. One key disadvantage of this scheme is that the signal is being mixed with itself which approximately doubles the amount of noise in the system and results in an optical signal to noise ratio (OSNR) penalty with respect to the coherent case. Note that the reasons for using coherent detection over direct detection are discussed at the start of the next chapter.

2.2.4.2 Polarisation Diverse Coherent Receiver

When decoding dual-polarisation phase shift keyed signals, a polarisation-diverse coherent receiver can be used [42]. A diagram of a polarisation diverse coherent receiver is shown in Figure 2.15 below [42]. The receiver consists of polarisation beam splitters (PBSs) and 90^o optical hybrids. 90^o optical hybrids produce four outputs which are proportional to the sum of the LO input delayed by one of [0^o, 90^o, 180^o, 270^o] and the signal field (as can be seen from the equations in [42]). This receiver allows for the in-phase and quadrature components of the received waves, on both polarisations, to be decoded.

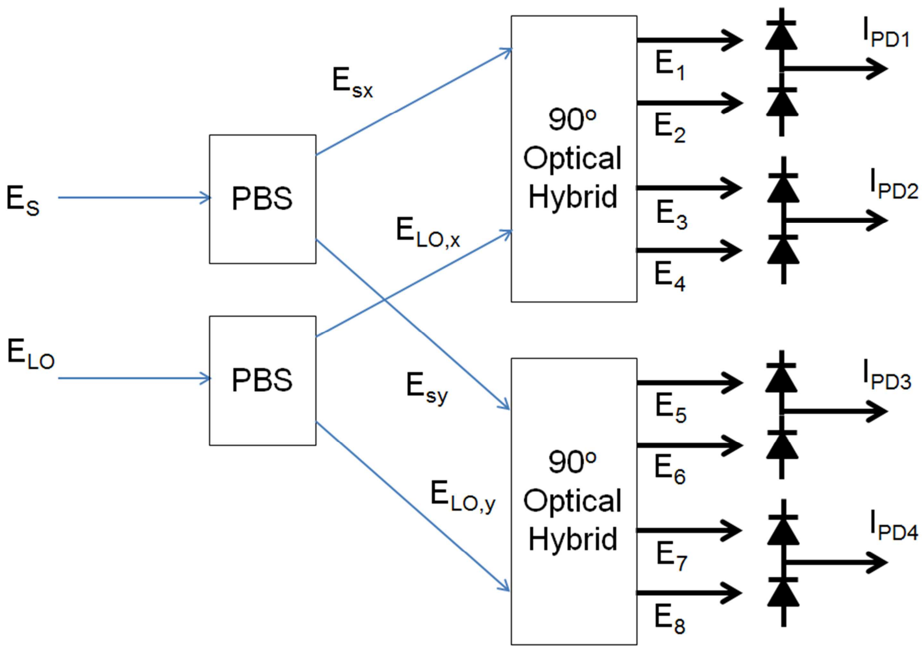

Figure 2.15: Polarisation-diverse coherent receiver [42].

If the signal wave's polarisation components, $E_{sx}(t)$ and $E_{sy}(t)$, and the LO wave's components, $E_{LO,x}(t)$ and $E_{LO,y}(t)$, are represented as:

$$E_{sx}(t) = \sqrt{\alpha_{pol}\ P_s}\, e^{j\delta}.e^{j\theta_s(t)}.e^{j\omega_s t} \tag{2.20}$$

$$E_{sy}(t) = \sqrt{(1-\alpha_{pol})P_s}\,.e^{j\theta_s(t)}.e^{j\omega t} \tag{2.21}$$

$$E_{LO,x}(t) = \sqrt{\frac{P_{LO}}{2}}.e^{j\theta_{LO}(t)}.e^{j\omega_{LO} t} \tag{2.22}$$

$$E_{LO,y}(t) = \sqrt{\frac{P_{LO}}{2}}.e^{j\theta_{LO}(t)}.e^{j\omega_{LO} t} \tag{2.23}$$

then the output currents, where $\omega_s=\omega_{LO}$, are given as [42]:

$$I_{PD1} = R\sqrt{\frac{\alpha_{pol}P_S P_{LO}}{2}}\cos[\theta_s(t) - \theta_{nLO}(t) + \delta] \tag{2.24}$$

$$I_{PD2} = R\sqrt{\frac{\alpha_{pol}P_S P_{LO}}{2}}\sin[\theta_s(t) - \theta_{nLO}(t) + \delta] \tag{2.25}$$

$$I_{PD3} = R\sqrt{\frac{(1-\alpha_{pol})P_S P_{LO}}{2}}\cos[\theta_s(t) - \theta_{nLO}(t)] \tag{2.26}$$

$$I_{PD4} = R\sqrt{\frac{(1-\alpha_{pol})P_S P_{LO}}{2}}\sin[\theta_s(t) - \theta_{nLO}(t)] \tag{2.27}$$

where R is the responsivity of the photodiodes, P_s is the power of the signal, P_{LO} is the power of the LO, α_{pol} is the proportion of the signal power going into the coherent receiver in the x-polarisation, δ is the phase difference between the two polarisation components of the signal, $\theta_S(t)$ is the phase modulation of the signal (with transmitter phase noise also being present), and $\theta_{nLO}(t)$ is the phase noise of the LO. However, equations (2.24) to (2.27) relate to a homodyne receiver, where $\omega_s=\omega_{LO}$, while in this thesis the focus will be on intradyne receivers where a non-zero angular frequency term $(\omega_s - \omega_{LO})t$ will be included in the argument of the cosine and sine terms of equations (2.24) to (2.27). The currents can then be sent through electronic DSP to remove distortions caused by chromatic dispersion, polarisation rotations, and frequency offset [43].

2.3 Summary

In this chapter, the motivations behind this work and the key devices used to implement this work have been described. It was described how using an optical packet/ burst switched network with coherent detection can reduce the electronic processing used in networks. By using higher-order modulation formats more bits per symbol/ higher spectral efficiency can be achieved. A key component of the coherent OPS and OBS networks is the fast switching tuneable laser and the main points of interest with respect to this device were discussed. The wavelength tuning mechanism which appears to be most suitable is current tuning due to its fast tuning times. The SG-DBR laser is a very suitable laser for coherent OPS/OBS networks as it is current tuned and can access a large range of wavelengths. It was shown that MZM architectures can implement coherent modulation formats by varying amplitude, phase and polarisation. Finally, polarisation-diverse coherent receivers were introduced with their fundamental equations provided. Before presenting detailed descriptions of the novel characterisation and transmission systems developed in this work, a review of the standard laser phase noise/ frequency transient characterisation techniques, standard DSP encoding for transmission and standard DSP for demodulating signals detected with a polarisation-diverse coherent receiver will be presented.

References

1. Cisco VNI, "The Zettabyte Era—Trends and Analysis *(29/05/2013)*," http://www.cisco.com/c/en/us/solutions/collateral/service-provider/visual-networking-index-vni/VNI_Hyperconnectivity_WP.html.

2. Daily Mail, "Traditional television channels could soon disappear and be replaced by internet catch-up services says BBC boss," http://www.dailymail.co.uk/news/article-2690098/BBC-boss-Traditional-television-channels-soon-disappear.html.

3. A. D. Ellis, Jian Zhao, and D. Cotter, "Approaching the Non-Linear Shannon Limit," Journal of Lightwave Technology **28,** 423-433 (2010).

4. R. S. Tucker, "Optical and electronic technologies for packet switching," in *Optical Fiber Telecommunications VB: Systems and Networks,* I. P. Kaminow, L. Tingye, and A. E. Willner, eds. (Academic Press, 2006), pp. 695-738.

5. R. Doverspike and P. Magill, "Commercial optical networks, overlay networks and services," in *Optical Fiber Telecommunications VB: Systems and Networks,* I. P. Kaminow, L. Tingye, and A. E. Willner, eds. (Academic Press, 2008), pp. 511-560.

6. M. Carroll, J. Roese, and T. Ohara, "The Operator's View of OTN Evolution," IEEE Communications Magazine **48,** 46-52 (2010).

7. R. Ramaswami and K. N. Sivarajan, *Optical Networks A Practical Perspective, 2nd Edition* (Academic Press, 2002).

8. P. J. Winzer and R. J. Essiambre, "Advanced Optical Modulation Formats," Proceedings of the IEEE **94,** 952-985 (2006).

9. T. S. El-Bawab, "Preliminaries and Terminologies," in *Optical Switching,* T. S. El-Bawab, ed. (Springer, 2006), pp. 3-35.

10. J. E. Simsarian, J. Gripp, A. H. Gnauck, G. Raybon, and P. J. Winzer, "Fast-Tuning 224-Gb/s Intradyne Receiver for Optical Packet Networks," in *Optical Fiber Communication Conference and Exposition,* (IEEE, 2010), pp. PDPB5.

11. J. P. Jue, W. H. Yang, Y. C. Kim, and Q. Zhang, "Optical packet and burst switched networks: a review," IET Communications **3,** 334-352 (2009).

12. Y. Chen, C. Qiao, and X. Yu, "Optical Burst Switching: A New Area in Optical Networking Research," IEEE Network **18,** 16-23 (2004).

13. J. Gripp, M. Duelk, J. E. Simsarian, A. Bhardwaj, P. Bernasconi, O. Laznicka, and M. Zirngibl, "Optical Switch Fabrics for Ultra-High-Capacity IP Routers," Journal of Lightwave Technology **21,** 2839-2850 (2003).

14. B. Puttnam, M. Dueser, B. Thomsen, and P. Bayvel, "Burst mode operation of a DS-DBR widely tunable laser for wavelength agile system applications," in *Optical Fiber Communication Conference,* (OFC, 2006), pp. OWI86.

15. E. Connolly, A. Kaszubowska-Anandarajah, and L. P. Barry, "Cross Channel Interference due to Wavelength Drift of Tuneable Lasers in DWDM Networks," in *International Conference on Transparent Optical Networks,* (IEEE, 2006), pp. Mo.P.13.

16. H. Okamoto, K. Sato, H. Yasaka, Y. Yoshikuni, K. Oe, K. Kishi, Y. Kondo, and M. Yamamoto, "Fast wavelength switching for 10Gbit/s NRZ signal with a tunable duplex integrated light source," Electronics Letters1274-1276 (1995).

17. R. Maher, D. S. Millar, S. J. Savory, and B. C. Thomsen, "Widely Tunable Burst Mode Digital Coherent Receiver With Fast Reconfiguration Time for 112 Gb/s DP-QPSK WDM Networks," Journal of Lightwave Technology **30,** 3924-3930 (2012).

18. A. J. Walsh, J. Mountjoy, A. Fagan, C. Browning, A. D. Ellis, and L. P. Barry, "Reduced Waiting Times Using a Fast Switching Dual-Polarization DDQPSK Receiver in a Packet Switched Network," in *European Conference and Exhibition on Optical Communication,* (IEEE, 2014), pp. P.4.2.

19. J. R. Barry and E. A. Lee, "Performance of Coherent Optical Receivers," Proceedings of the IEEE **78,** 1369-1394 (1990).

20. L. Kazovsky, S. Benedetto, and A. Willner, "Basic Optical Fiber Communications Components (Chapter 1)," in *Optical Fiber Communications Systems,* Boston, ed. (Artech House, 1996), pp. 1-100.

21. K. Shi, F. Smyth, P. M. Anandarajah, D. Reid, Y. Yu, and L. P. Barry, "Linewidth of SG-DBR laser and its effect on DPSK transmission," Optics Communications **283,** 5040-5045 (2010).

22. G. P. Agrawal, "Chapter 1, Fiber Gratings," in *Applications of Nonlinear Fiber Optics,* (Academic Press, 2001), pp. 1-61.

23. C. Ye, *Tunable External Cavity Diode Lasers* (World Scientific, 2004).

24. L. A. Coldren, S. W. Corzine, and M. L. Masanovic, *Diode Lasers and Photonic Integrated Circuits* (Wiley, 2012).

25. C. H. Henry, "Theory of the Linewidth of Semiconductor Lasers," IEEE Journal of Quantum Electronics **18,** 259-264 (1982).

26. S. Savory and A. Hadjifotiou, "Laser Linewidth Requirements for Optical DQPSK Systems," IEEE Photonics Technology Letters **16,** 930-932 (2004).

27. L. A. Coldren, G. Fish, Y. Akulova, J. Barton, L. Johansson, and C. Coldren, "Tunable semiconductor lasers: A tutorial," J. Lightwave Technol. **22,** 193 (2004).

28. M. Larson, "Widely tunable semiconductor lasers," in *Optical Fiber Communication Conference,* Optical Society of America, ed. (OFC, 2014), pp. Tu2H. 1.

29. M. Aman and J. Buus, *Tunable Laser Diodes* (Artech House, 1998).

30. K. Shi, Y. Yu, R. Zhang, W. Liu, and L. P. Barry, "Static and dynamic analysis of side-mode suppression of widely tunable sampled grating DBR (SG-DBR) lasers," Optics Communications **282,** 81-87 (2009).

31. F. Smyth, "Investigation of Performance Issues Affecting Optical Circuit and Packet Switched WDM Networks (PhD Thesis, Dublin City University)," (2008).

32. A. J. Walsh, T. N. Huynh, J. Mountjoy, A. Fagan, A. D. Ellis, and L. P. Barry, "Employing DDBPSK in optical burst switched systems to enhance throughput," in *39th European Conference and Exhibition on Optical Communication,* (Optical Society of America, 2013), pp. P.3.17.

33. J. E. Simsarian, J. Gripp, S. Chandrasekhar, and P. Mitchell, "Fast-Tuning Coherent Burst-Mode Receiver for Metropolitan Networks," IEEE Photonics Technology Letters **26,** 813-816 (2014).

34. K. Shi, R. Watts, D. Reid, T. N. Huynh, C. Browning, P. M. Anandarajah, F. Smyth, and L. P. Barry, "Dynamic Linewidth Measurement Method via an Optical Quadrature Front End," IEEE Photonics Technology Letters **23,** 1591-1593 (2011).

35. J. Kakande, R. Slavík, R. Phelan, J. O'Carroll, B. Kelly, and D. J. Richardson, "Tunable QAM Transmitter Based on Direct Modulation Laser," in *Optical Fiber Communication Conference and Exposition,* (OFC, 2014), pp. W1J.3.

36. H. Okayama, "Lithium Niobate Electro-Optic Switching," in *Optical Switching,* T. S. El-Bawab, ed. (Springer, 2006), pp. 39-82.

37. M. Seimetz, "Performance of Coherent Optical Square-16-QAM-Systems based on IQ-Transmitters and Homodyne Receivers with Digital Phase Estimation," in *Optical Fiber Communication Conference and Exposition,* (IEEE, 2006), pp. NWA4.

38. T. I. Xia and A. Wellbrock, "Commercial 100-Gbit/s Coherent Transmission Systems," in *Optical Fiber Telecommunications VIB: Systems and Networks,* I. P. Kaminow, L. Tingye, and A. E. Willner, eds. (Academic Press, 2013), pp. 45-82.

39. T. Pfau, S. Hoffmann, and R. Noé, "Hardware-Efficient Coherent Digital Receiver Concept With Feedforward Carrier Recovery for M-QAM Constellations," Journal of Lightwave Technology **27,** 989-999 (2009).

40. H. Bülow, "Polarization QAM Modulation (POL-QAM) for Coherent Detection Schemes," in *Optical Fiber Communication Conference and Exposition,* (IEEE, 2009), pp. OWG2.

41. X. Liu, S. Chandrasekhar, and A. Leven, "Self-coherent optical transport systems," in *Optical Fiber Telecommunications VB: Systems and Networks,* I. P. Kaminow, T. Li, and A. E. Willner, eds. (Academic Press, Oxford, 2008), pp. 131-178.

42. K. Kikuchi, "Coherent optical communication systems," in *Optical Fiber Telecommunications VB: Systems and Networks,* I. P. Kaminow, T. Li, and A. E. Willner, eds. (Academic Press, Oxford, 2008), pp. 95-130.

43. A. Leven, N. Kaneda, U. -V. Koc, and Y. -K. Chen, "Frequency Estimation in Intradyne Reception," IEEE Photonics Technology Letters **19,** 366-368 (2007).

Chapter 3

Coherent Optical Communication

In this chapter, the theory and standard techniques of coherent optical communications will be explored. A description of a standard coherent optical transmission system will be discussed. This chapter will then focus on the key impairments associated with coherent optical communications in back-to-back scenarios which are: (i) additive white Gaussian noise (AWGN), (ii) frequency offset, (iii) phase noise, and (iv) polarisation rotations. In addition, standard techniques to characterise the phase noise of static lasers and previously published techniques to characterise frequency chirp and time-resolved phase noise of switching lasers will be reviewed. The limitations of these techniques will also be discussed which will motivate the need for the novel approaches developed in this work in order to overcome these limitations. This thesis does not focus on impairments which are associated with long distance transmission such as chromatic dispersion, polarisation mode dispersion (PMD) and non-linear impairments since the issues associated with back-to-back transmission need to be fully resolved before long distance transmission problems of coherent optical packets are considered. The standard techniques to overcome the back-to-back impairments will be discussed as well as their limitations which will motivate the need for the novel DSP strategies developed in this thesis which can overcome these limitations. Finally, BER versus signal to noise ratio per bit (SNR_b) relationships for different decoding systems will be explored.

3.1 Coherent Optical Communication System Overview

Shown in Figure 3.1 is a typical coherent optical communication system. The transmitter is typically a low linewidth laser with a wavelength near 1550nm. The transmitter laser output is then passed through a polarisation controller (PC) which is varied so that the light entering the modulator has the correct polarisation for that modulator. Note that the modulator may be a single-polarisation modulator or a dual-polarisation modulator. The modulator then puts data onto the carrier of the light entering the modulator by varying one or more of the carrier's parameters; amplitude, phase or polarisation. The channel through which the modulated carrier passes through is typically a long length of optical fibre which may have EDFAs used in order to provide enough power at the receiver.

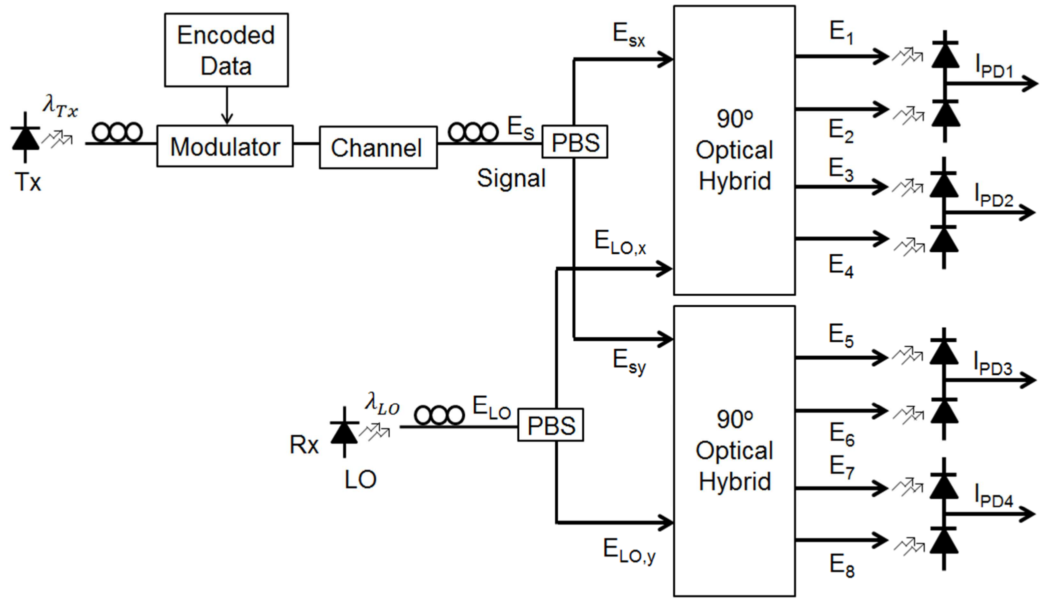

Figure 3.1: Typical coherent optical communications system setup, where the modulator could be a single or dual-polarisation modulator.

One receiver which can decode carriers using a combination of amplitude, phase and polarisation modulation is the polarisation-diverse coherent receiver. The key functions of a polarisation-diverse coherent receiver are: (i) to convert the carrier and data modulation of the received signal from the optical domain to the electrical domain, (ii) to down-convert the optical carrier from a value greater than 190THz to an electrical carrier that is only a few gigahertz and (iii) to output the in-phase and quadrate components of a signal for both the x and y polarisation. More details of the polarisation-diverse coherent receiver are provided in [1]. The essential components of a polarisation-diverse coherent receiver are shown in Figure 3.1. After going through an optional PC (which is useful for laboratory experiments) the input signal, $E_s(t)$, goes through a PBS where each output polarisation component goes to a different 90^o optical hybrid. The LO is a laser which is separate from the polarisation-diverse coherent receiver which goes through a PC. Then, it goes through a PBS with each output polarisation component going to a separate 90^o optical hybrid. The output polarisation components from the PBSs with the same state of polarisation go to the same 90^o optical hybrid. As explained in the previous chapter, a 90^o optical hybrid has four outputs with each output proportional to the sum of the LO input delayed by one of [0^o, 90^0, 180^0, 270^0] and the signal input. The outputs of the 90^0 optical hybrids are detected by balanced photodiodes as shown in Figure 3.1. Balanced photodiodes prevent optical power from one of the two coupler outputs being lost/wasted (balanced photodiodes are discussed in [2]). The four outputs from the balanced photodiodes are the in-phase and quadrature components of each of the x and y polarisations. The equations for these four outputs were given at the end of the previous chapter.

The key purpose of the LO is to down-convert the received signal from a carrier of high frequency, greater than 190THz, to a carrier which is only a few gigahertz. The LO and the transmitter laser need to have a difference in frequency which is less than the bandwidth of the receiver electronics or else the beat signal will not be observed. The current outputs from the polarisation-diverse coherent receiver will have to go through DSP in order to remove impairments such as residual frequency offset between the transmitter and LO lasers and to reverse any precoding performed at the transmitter in order to recover the data. The DSP used in coherent optical communications for M-ary PSK data will be described in more detail in section 3.4.

In back-to-back scenarios, the distance of fibre travelled is at most of the order of meters with the main impairments being: (i) amplified spontaneous emission (ASE) noise from amplifiers, (ii) polarisation rotations, (iii) frequency offsets between the transmitter and LO lasers, and (iv) phase noise from the transmitter and LO lasers. These impairments must first be dealt with before transmission impairments such as chromatic dispersion and PMD are investigated. As stated above, only back-to-back impairments are considered in this thesis.

3.1.1 Reasons to Use Coherent Optical Communication Systems

Besides coherent detection of signals, it is also possible to receive signals by using “direct detection” where the signal is detected simply by a photodiode or using a combination of delay interferometers and photodiodes. The use of delay interferometers was discussed in the previous chapter. While direct detection systems are often simpler to implement than coherent systems where little or no DSP may be required they have shortcomings compared with coherent detection systems:

(1) Coherent detection becomes shot-noise limited in terms of the receiver sensitivity by increasing the LO power which makes all other noise terms negligible compared with shot-noise [2]. However direct-detection systems do not have this capability. It is further elaborated in [2] that power penalty difference between a direct detection scheme for OOK limited by the “quantum limit” and the shot-noise limited coherent BPSK scheme is 3.5dB.

(2) Coherent systems are able to filter out closely spaced signals in a WDM setting in the electrical domain [1], which can eliminate the need for additional narrowband optical filters.

3.2 Back-to-Back Channel Impairments

This section identifies various important back-to-back impairments and provides mathematical descriptions of these impairments.

3.2.1 Additive White Gaussian Noise

It is typical in the theory of communications to measure the performance of a proposed data transmission system in terms of its performance in the presence of AWGN. AWGN is defined as a random process whose PSD is the same constant value at each frequency, where its value indicates the severity of the AWGN. A sample AWGN process is shown in Figure 3.2 (a) and the PSD of this AWGN process is shown in Figure 3.2 (b).

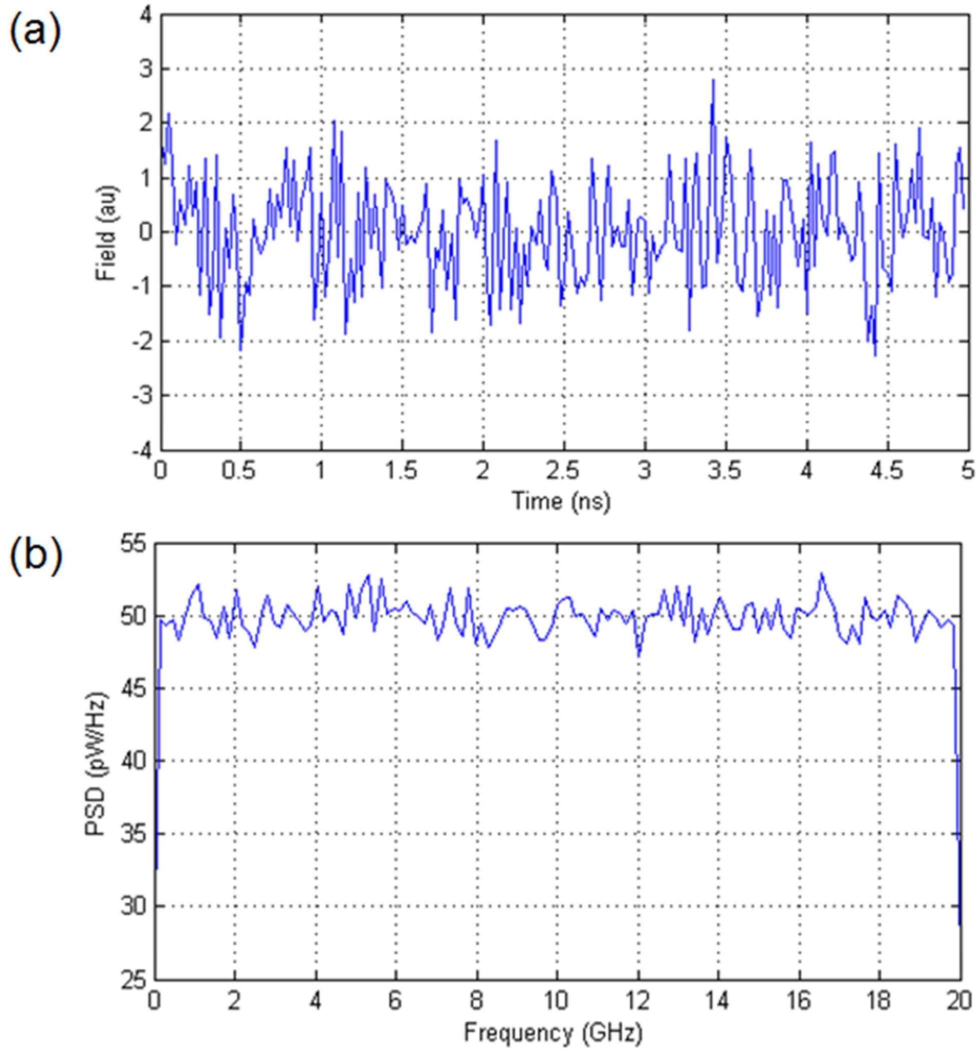

Figure 3.2: Plot of (a) AWGN vs. time (b) PSD of AWGN.

A measure of the quantity of noise in a signal is given by the SNR_b which is defined as the ratio of the signal energy per bit to twice the PSD of the unwanted noise (which is often AWGN in theoretical analysis) [3]. Optical signal to noise ratio (OSNR) is a parameter which is often measured in optical communications systems in order to determine the level of noise in a system. OSNR is related to SNR_b via the formula [4]:

$$\mathrm{OSNR} = \frac{R_B SNR_b}{2B_{ref}} \tag{3.1}$$

where R_B is the bitrate of the system being measured (containing the sum of the bit rates in both polarisations), B_{ref} is the bandwidth resolution (with units of frequency) of the optical spectrum analyser (OSA) and SNR_b is the signal to noise ratio in one polarisation. Since R_B is the sum of the bit rates in both polarisations the 2 in the denominator remains for both single-polarisation systems and dual-polarisation systems. Note that in experiments where ASE noise from an EDFA (with no input) is added to a signal in order to vary its OSNR, the spectrum of the added ASE noise within the bandwidth of the signal is not always flat. Variations in the ASE spectrum within the bandwidth of the signal can be flattened by using an optical bandpass filter.

3.2.2 Polarisation Rotations

When light propagates through a fibre, polarisation rotations occur. This means that the components of light oscillating in different planes will vary in power and relative phase delay. This, in the simplest case, is characterised by a multiplication with a unitary matrix (given in [5]):

$$\begin{bmatrix} Ex_{out} \\ Ey_{out} \end{bmatrix} = \begin{bmatrix} \cos^2\psi_1 e^{-j.(\Gamma/2)} + \sin^2\psi_1 e^{j.(\Gamma/2)} & -j\sin(\Gamma/2)\sin 2\psi_1 \\ -j\sin(\Gamma/2)\sin 2\psi_1 & \cos^2\psi_1 e^{j.(\Gamma/2)} + \sin^2\psi_1 e^{-j.(\Gamma/2)} \end{bmatrix} \begin{bmatrix} Ex_{in} \\ Ey_{in} \end{bmatrix} \tag{3.2}$$

where Γ and ψ_1 are the phase retardation and azimuth angle respectively [5].

3.2.3 Frequency Offset

Frequency offset impairments occur as a result of the transmitter and LO lasers having different frequencies. This impairment must be removed in the case of M-ary PSK signals since the presence of the frequency offset will affect phase changes which can either reduce the performance of the system or make recovery of the data impossible. It has been discussed in the previous chapter that fast switching tuneable lasers will exhibit frequency transients directly after they switch wavelengths. This will consequently result in frequency offset transients at the start of a packet or burst in a switching scenario if a tuneable laser is at the transmitter and/ or at the receiver's LO. This motivates the search for a robust frequency offset compensation algorithm to cope with large and varying frequency offsets. A key issue with frequency offset compensation algorithms is that the frequency offset needs to be determined even though the signal contains data. If this data affects the phase of the signal, such as in the case of M-ary PSK, then issues can arise. A situation will be assumed where a coherent receiver has detected a signal which is then correctly downsampled to one sample per symbol and sampled in the optimum position, resulting in a downsampled M-ary PSK signal with a frequency offset present. If the amplitude is assumed to be constant then the resulting phase of the received signal, $\Phi_{rec}(t)$, can be expressed as:

$$\Phi_{rec}(kT) = \omega kT + \Phi_{mod}(kT) + \Phi_n(kT) + \Phi_0 \qquad (3.3)$$

where ω is the angular frequency offset, assumed to be constant in this case, $\Phi_{mod}(t)$ is the M-ary PSK phase modulation at different points in time, $\Phi_n(t)$ is the Wiener phase noise, Φ_0 is the initial phase, n is the sample index and T is the symbol period. For the purposes of understanding frequency offset issues, the Wiener phase noise will be assumed to be negligible. $\Phi_{mod}(kT)$ for an M-ary PSK signal can be expressed as:

$$\Phi_{mod}(kT) = \frac{2\pi}{M} k_n \qquad (3.4)$$

where k_n is a random integer in the range [0,M-1].

Observing equations (3.3) and (3.4), it can be seen that it would be impossible to distinguish whether a $2\pi/M$ change in $\Phi_{rec}(t)$, was due to a frequency offset equal to $2\pi/(MT)$ with zero phase modulation or was due to a $2\pi/M$ change from data modulation with zero frequency offset. This ambiguity will be present for frequency offsets outside the $\pm\pi/(MT)$ range, where some form of frequency offset correction is employed. Therefore, ambiguity with respect to estimating frequency offset will always be present in the above paradigm where the frequency offset is sufficiently large and the received phase has been downsampled to one sample per symbol.

3.2.4 Phase Noise

Phase noise is where the laser's instantaneous phase has a Wiener phase noise process added to it resulting in phase shifts over time. Wiener phase noise ultimately limits the number of phase states possible in a phase modulated data transmission system. The instantaneous phase noise of a laser, $\Phi_n(t)$, considering only Wiener noise, is typically governed by the following rule [6]):

$$\left\langle \left(\Phi_n\left(t + T_{int}\right) - \Phi_n\left(t\right)\right)^2 \right\rangle = 2\pi\Delta\nu T_{int} \tag{3.5}$$

where T_{int} is a time interval and $\Delta\nu$ is called the "linewidth". It is possible to derive the Lorentzian PSD of the optical field using the assumption of only a Wiener phase noise process, where this derivation is provided in [2]. The PSD of the optical field, $S_x(\omega)$, is given as [2]:

$$S_x\left(\omega\right) = \frac{\left(\dfrac{2P_1}{\pi\Delta\upsilon}\right)}{1 + \left(\dfrac{\omega - \omega_0}{\pi\Delta\upsilon}\right)^2} \tag{3.6}$$

where ω is angular frequency, P_1 is the average power of the field and ω_0 is the angular frequency of the field. This Lorentzian PSD is utilised in the measurement of linewidth as is described in section 3.3.1. Note that a Lorentzian curve, $L(x)$ is of the form [7]:

$$L\left(x\right) = \frac{1}{\pi}\left(\frac{\dfrac{1}{2}\Gamma}{\left(x - x_0\right)^2 + \left(\dfrac{1}{2}\Gamma\right)^2}\right) \tag{3.7}$$

where x is the independent variable, with x_0 and Γ being constants.

3.3 Phase Noise Measurement Schemes

Measuring the level of phase noise in a laser output is critical to predicting the performance of a system that uses that laser, with different levels of performance depending on the modulation format and the symbol rate used. A number of phase noise characterisation techniques will be discussed in the following section. These will consist of static linewidth/ phase noise measurement techniques as well as time-resolved frequency chirp/ phase noise measurement techniques.

3.3.1 Delayed-Self Heterodyne Phase Noise Measurement

The delayed self-heterodyne setup is shown in Figure 3.3 (with a similar setup shown in [8]). The laser under test is split into two parts by a 50/50 coupler, where one part is sent through a fibre delay line and the other part is frequency shifted by driving a phase modulator with a 2GHz sine wave. A polarisation controller is used to optimise the polarisation going into the phase modulator. Both parts are recombined with a 50/50 coupler with one output of the coupler going to a photodiode, then amplified electrically and, finally, the amplified signal is measured by a radio frequency spectrum analyser (RFSA). The RFSA will detect a spectrum which is expected to have a Lorentzian profile. If the frequency noise is a zero-mean white Gaussian process, this will imply that the phase noise will be a Wiener process which will result in the power spectral density of the field having a Lorentzian profile as derived in [2]. By fitting a Lorentzian curve to the measured spectrum it will be possible to determine the FWHM linewidth from the fit, which then needs to be divided by 2 as the phase noise of the combined signal after the 50/50 coupler, used for measurement, is double the phase noise of the laser under test.

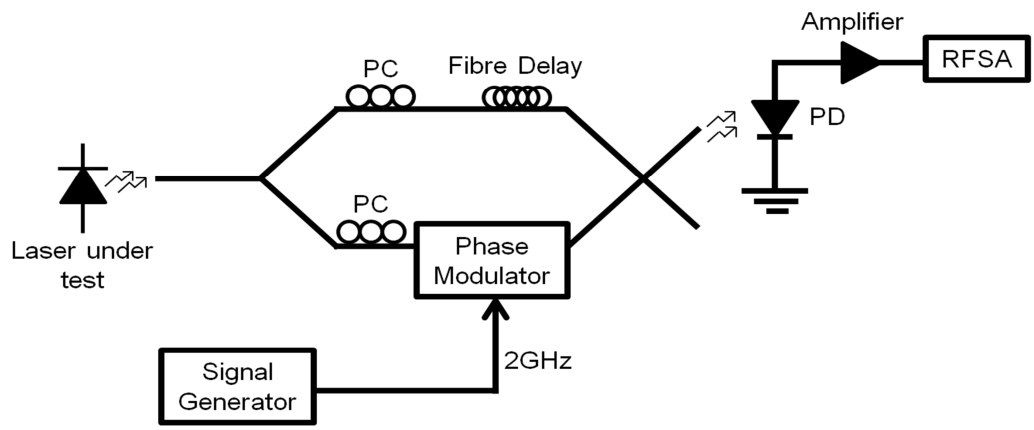

Figure 3.3: Delayed Self-Heterodyne setup for measuring linewidth (PD= "Photodiode") (similar to setup in [8]).

3.3.2 Coherent Receiver Phase Noise Measurement

Another method used to characterise phase noise is to use a coherent receiver phase noise measurement scheme, such as the one shown in Figure 3.4, as suggested in [6]. Note the linewidth of the LO input should be much lower than the laser under test. The LO models used in experiments and their specified linewidths will be given for each experiment.

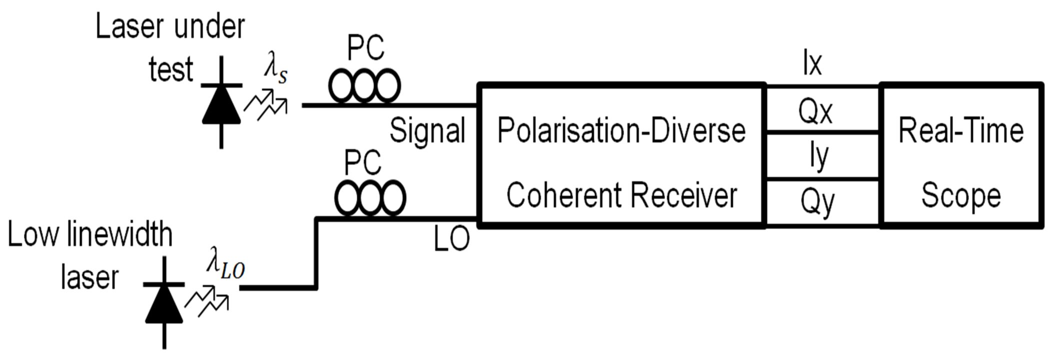

Figure 3.4: Coherent receiver method of measuring phase noise.

If each PC is set appropriately so that the beat signals will be concentrated on the x polarisation, then by using the real-time scope and offline DSP it is possible to determine the instantaneous phase difference, $\Phi_{diff\_x}(t)$ between the laser under test and the low linewidth laser:

$$\Phi_{\mathrm{diff\_x}}(t) = \mathbf{UNWRAP}\left[\mathbf{ATAN2}\left[\mathrm{Ix}, \mathrm{Qx}\right]\right] \tag{3.8}$$

where Ix and Qx are the x-polarisation beat signals from the coherent receiver as shown in Figure 3.4. **`ATAN2[p,q]`** is the MATLAB command for the two argument arctan where p is the cos input and q is the sin input (its output is in the range (-π, π]). **`UNWRAP[x]`** is the MATLAB unwrap function which interprets any phase changes greater than or equal π to be the result of the phase drifting outside the (-π,π] range where an appropriate 2π phase addition is made to ensure a continuous phase trajectory. Using the polarisation-diverse coherent receiver equations from chapter 2:

$$\mathrm{I_x} = \mathrm{R}\sqrt{\frac{\mathrm{P_S P_{LO}}}{2}}\cos[\theta_s(t) - \theta_{LO}(t) + \delta] \tag{3.9}$$

$$\mathrm{Q_x} = \mathrm{R}\sqrt{\frac{\mathrm{P_S P_{LO}}}{2}}\sin[\theta_s(t) - \theta_{LO}(t) + \delta] \tag{3.10}$$

where P_s is the power entering the signal port (power of the laser under test), P_{LO} is the power entering the LO port (power of the low linewidth laser), $\theta_s(t)$ is the instantaneous phase of the signal port input (laser under test), $\theta_{LO}(t)$ is the instantaneous phase of the LO port (low linewidth laser), R is the responsivity of the photodiodes and δ is an arbitrary phase offset (δ is phase difference between x and y detected fields but only the x-field is being used here). Substituting equations (3.9) and (3.10) into (3.8) and simplifying yields:

$$\begin{aligned}\Phi_{diff\_x}(t) = \mathrm{unwrap}[\mathrm{atan2}[&\cos[\theta_s(t) - \theta_{LO}(t) + \delta] \\ &, \sin[\theta_s(t) - \theta_{LO}(t) + \delta]]]\end{aligned} \tag{3.11}$$

The instantaneous phase of the laser under test and the low linewidth laser can be given as:

$$\theta_s(t) = \omega_s t + \theta_{ns}(t) + \theta_{0s} \tag{3.12}$$

$$\theta_{LO}(t) = \omega_{LO} t + \theta_{nLO}(t) + \theta_{0LO} \tag{3.13}$$

where the ω_s and ω_{LO} terms represent angular frequencies of the signal and LO respectively; $\theta_{ns}(t)$ and $\theta_{nLO}(t)$ terms represent phase noise processes of the signal and LO respectively, and θ_{0s} and θ_{0LO} terms represent initial phases of the signal and LO respectively. Hence, equation (3.11) will contain a frequency offset term, $((\omega_s - \omega_{LO})t)$, the difference in phase noise between the two lasers, $(\theta_{ns}(t) - \theta_{nLO}(t))$, (this essentially increases the phase noise since phase noise is a random process) and an initial phase term. The frequency offset term can be removed by doing a linear regression fit of $\Phi_{diff\_x}(t)$ against t and removing the estimated slope from $\Phi_{diff\_x}(t)$ which should leave only the instantaneous phase noise plus a constant phase term. From equation (3.5), it can be seen that if a linear fit of variance of the differential phase over a time difference, T_{int}, versus T_{int} is calculated then the linewidth can be estimated. The contribution of the phase noise from the low linewidth laser to the estimated linewidth should be small enough in comparison to the phase noise of the laser under test in order for it be considered to be negligible. It will be shown in the next chapter that the method of calculating the variance of the differential phase over a time T_{int} is critical to correctly calculating the linewidth.

3.3.3 Time-Resolved Frequency Chirp/ Phase Noise Measurements

As this thesis is concerned with fast switching tuneable lasers, it will be important to estimate the phase noise dynamics and frequency chirp dynamics of a fast switching tuneable laser as a function of time just after a switching event. This will indicate what type of frequency offset compensation scheme needs to be employed as well as the limitations placed on the type of modulation which can be used as a result of the time-varying phase noise.

One method of calculating time-resolved phase noise is to take limited resolution spectra of the field of a beat signal between the switching laser and a low linewidth laser a number of times immediately after the switching event [9]. This method can be problematic as there will be a bandwidth resolution/ time resolution trade-off to be made. Another method uses a coherent receiver to calculate instantaneous frequency and calculates the variance of frequency deviations over a particular time-period to estimate linewidth [10]. A key limitation of this method is that it has a limited time resolution (in [10] it is 25.6ns) and, also, it is not clear to what degree deterministic frequency chirp for a given switching event will be interpreted as phase noise (this will be discussed in more detail in the next chapter). A method which has finer time resolution is suggested in [11], where time-resolved linewidth measurements are performed with a temporal resolution of 1ns using a delayed self-homodyne technique. However, this technique assumes a Wiener phase noise process directly after the switch and, also, separates deterministic frequency chirp from dynamic phase noise. It will be shown in the next chapter that the separation of frequency chirp from dynamic phase noise is unnecessary and that assumptions do not have to be made about what type of random process the phase noise exhibits.

Measurements which show the frequency chirp of a switching laser with a wavelength locker have also been performed in [12] using a detuned filter and power meter to implement a frequency discriminator. While this method can perform frequency chirp measurements, it is important to perform both frequency chirp and phase noise measurements simultaneously after a switching event and to do this in a coherent manner in order to accurately and precisely to predict performance of data transmission during this transient. This will be fully described in the next chapter.

3.4 DSP for Compensating Back-to-back Impairments

DSP is applied to M-ary PSK single carrier data detected by the real-time scope to recover the transmitted data. M-ary PSK data will be focused on here as this is a key modulation format type used in the experimental work of this thesis. The DSP flow diagram used to recover M-ary PSK single carrier data is shown in Figure 3.5.

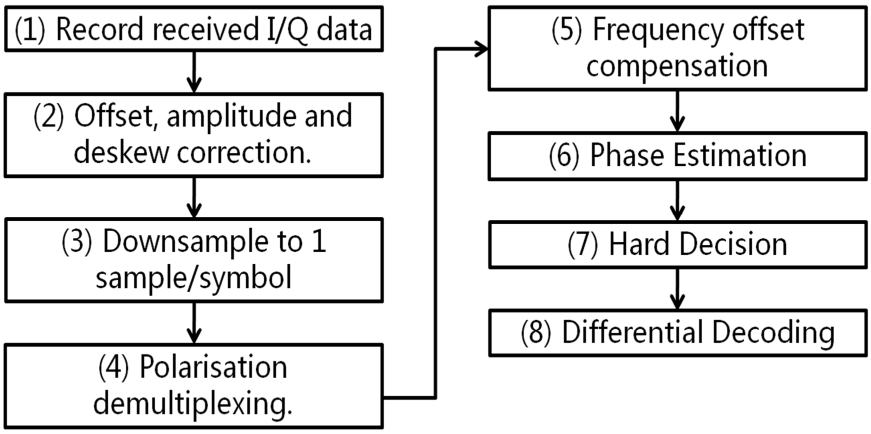

Figure 3.5: DSP flow diagram for recovering M-ary PSK single carrier data.

The outputs from the polarisation diverse coherent receiver are sampled by a real-time oscilloscope. After the sampling process, the I and Q signals from both polarisations have their offsets removed, their amplitudes normalised, IQ deskews corrected and delays between x and y detected signals corrected. Note that the IQ deskews of the coherent receiver were measured before data transmission experiments were performed and in the case of dual-polarisation experiments the delays between the X and Y channels of the polarisation diverse coherent receiver were also measured and corrected. Then, the sampled complex field is downsampled to one sample per symbol. After downsampling, the recorded I/Q data for either of the polarisations, $E_{in\_sample}(t)$, will be of the form:

$$E_{in\_sample}(kT_s) = A(kT_s).e^{j(\omega kT_s + \Phi_{mod}(kT_s) + \Phi_n(kT_s) + \Phi_0)} \tag{3.14}$$

where T_s is the sampling period and k is the sampling index. The next step is to correct for the effects of polarisation rotations. The techniques to do this are different for single-polarisation data and for dual-polarisation data. After this, the frequency offset term, ω, will be removed. Then, the Wiener phase noise term, $\Phi_n(t)$, will be estimated and this estimate will be used to mitigate the effects of phase noise. The effects of phase noise are not fully compensated for using the systems used in this work. VPI TransmissionMaker V8.7 simulations of 10GBaud differentially encoded QPSK show that the BER versus OSNR performance gets worse as linewidth increases, with noise floors appearing. Note that VPI TransmissionMaker V8.7 (or "VPI" for short) is a simulation tool used to simulate telecommunication systems where individual components used in the simulator can operate in the optical domain or the electrical domain. The simulations results showed a minimum error floor of $9*10^{-4}$ when the linewidth was set to 100MHz. After the Wiener phase noise is mitigated, it is expected that a constellation diagram of M phase states will appear at which point a hard decision (deciding whether a given phase value is closest to 0, $2\pi/M$, $4\pi/M$, etc.) will be made in order to determine what the transmitted data symbols were. Then, single differential decoding of the phase is performed on the hard decision symbols if single differential encoding was implemented at the transmitter or possibly doubly differential decoding if doubly differential encoding was used. The resulting data symbols are then converted to data bits using Gray coding.

It is also possible to perform single differential decoding on the phase after frequency offset compensation and before the hard decision to give the original data symbols, assuming some form of differential encoding is performed at the transmitter (note that when doubly differential decoding is performed before the hard decision frequency offset compensation is not strictly necessary). A hard decision is then applied and the resulting decoded symbols can then be mapped to data (assuming Gray coding). However, this will result in worse BER versus OSNR performance compared with performing differential decoding after the hard decision as will be discussed in section 3.5. The individual sections of the DSP will now be described in detail.

3.4.1 Output Correction and Downsampling

In experiments, the outputs from the polarisation diverse coherent receiver are sampled by a real-time scope. The outputs then have their amplitude offsets removed, their amplitudes normalised and already measured deskews between the coherent receiver's outputs corrected. The next task is to downsample the signals to one sample per symbol. It is important to do this in order to efficiently perform signal processing on the received data. In order to do downsampling to one sample per symbol, the correct sampling phase (i.e. position in the symbol period) must be selected. One way to do this is to select the sampling phase with the highest average magnitude as this will most likely be correlated with the most open part of the eye-diagram. This can be done in a relatively straightforward manner if there is a whole number of samples per symbol used. Other slightly different approaches to utilising the shape of the eye-diagram to achieve downsampling/ clock recovery are: (i) differentiating the received field to detect the edges of a NRZ PSK pulse to do clock recovery, as suggested in [1], and (ii) using an error function to maximise the square modulus of the downsampled signal [13].

3.4.2 Polarisation Channel Impairments Correction: Constant Modulus Algorithm

If the transmitter sends data on only one polarisation, then decoding the data at the receiver can be done in a straightforward manner in terms of compensating channel polarisation rotation, by combining the received X and Y polarisations in the manner described in [1], which is essentially a feed-forward method.

However, if both polarisations are used at the transmitter to send data, then decoding is typically done using the constant modulus algorithm (CMA) [13], with a diagram of the CMA filters given in Figure 3.6 (similar diagram in [14]).

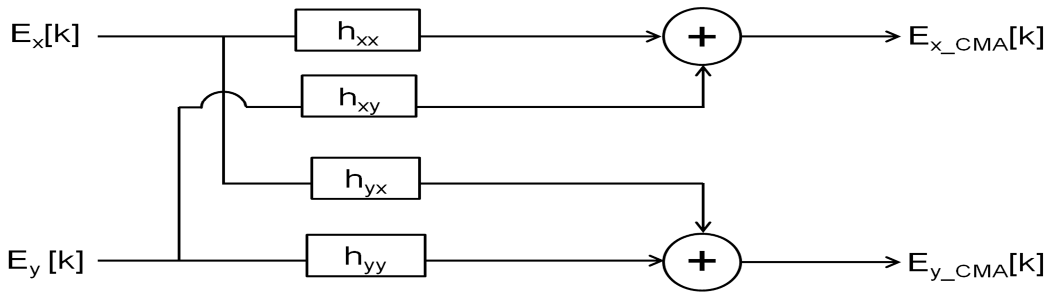

Figure 3.6: CMA filters applied to received signals (similar to part of diagram in [14]).

Unlike the single-polarisation demultiplexing case [1] which uses a feed-forward algorithm, CMA involves feedback. It is possible that the performance of the CMA will be affected by the state of polarisation of the received signal in burst scenarios resulting in variable convergence times [15]. Even worse, the CMA can potentially result in what is known as a singularity, meaning only data from one polarisation will be recovered [16]. Different methods have been proposed to prevent singularities [16, 17] and to reduce convergence times [18]. Another method of performing polarisation demultiplexing using an alternative feed-forward algorithm which does not have the singularity problem will be discussed in a later chapter on polarisation multiplexing in switching scenarios and further details of the CMA will also be given in that chapter.

3.4.3 Frequency offset: M^{th} Power Frequency Offset

There are numerous frequency offset correction algorithms in the literature, with some examples available at [15, 19, 20]. One key metric for a frequency offset compensation algorithm is the range of frequencies it can correct for. As discussed in section 3.2.3, frequency offset in the presence of M-ary PSK data results in a fundamental frequency offset ambiguity. It will be shown in chapter 5, which introduces doubly differential phase shift keying (DDPSK), that this ambiguity can be eliminated by suitable encoding. Note that it is possible to use some form of training symbols or known symbols in order to initially determine the frequency offset in order to overcome this ambiguity, where this was briefly discussed in [21]. It also suggested appropriate unwrapping to track the frequency offset. The use of training symbols may, however, not be suitable in switching environments where the frequency offset varies greatly since if the frequency offset is incorrectly tracked the frequency ambiguity problem will re-emerge unless more training symbols are sent. Also, the application of a pilot tone removes phase noise [22, 23] and eliminates the frequency offset issue; however, this will result in either part of the spectrum being occupied by the pilot tone or one polarisation being occupied by the pilot tone leading to a loss in spectral efficiency.

A commonly used approach that algorithms use to compensate for frequency offset in the presence of M-ary PSK data is to raise the received field to the power of M [15, 24]. A standard algorithm which does this and will be compared with DDPSK algorithms in this work will be described next. Shown in Figure 3.7 below is an M^{th} power frequency offset compensation method [24].

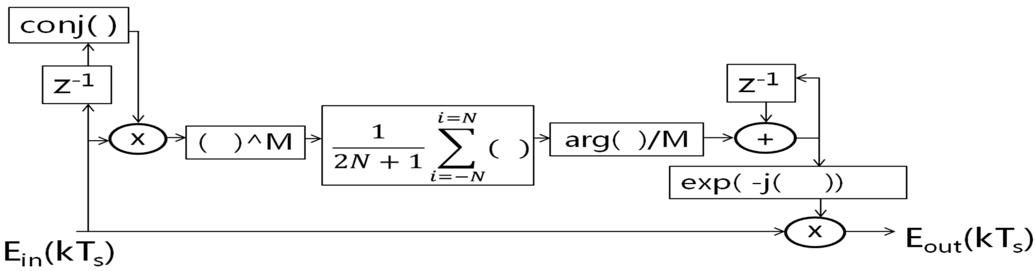

Figure 3.7: M^{th} power frequency offset compensation algorithm (diagram from [26], method from [24]).

In order for this algorithm to operate correctly it is necessary to ensure that the absolute value of the frequency offset is always less than $\pm R_s/(2M)$, where R_s is the symbol rate [25]. This avoids issues to do with frequency offset ambiguity. The downsampled field, $E_{in}(kT_s)$, is multiplied by its delayed complex conjugate:

$$E_1(kT_s) = E_{in}(kT_s)E_{in}^*((k-1)T_s) \qquad (3.15)$$

where $E_1(kT_s)$ is the output of this product. From equation (3.14) and equation (3.15), it can be seen that $E_1(kT)$ can be written as:

$$E_1(kT_s) = A(kT_s)A((k-1)T_s) \\ .e^{j(\omega T_s + \Phi_{mod}(kT_s) - \Phi_{mod}((k-1)T_s) + \Phi_n(kT_s) - \Phi_n((k-1)T_s))} \tag{3.16}$$

$E_1(t)$ is then raised to the power of M to give $E_2(t)$:

$$E_2(kT_s) = E_1^M(kT_s) \tag{3.17}$$

$$E_2(kT_s) = A^M(kT_s)A^M((k-1)T_s) \\ .e^{j(M\omega T_s + M\Phi_{mod}(kT_s) - M\Phi_{mod}((k-1)T_s) + M\Phi_n(kT_s) - M\Phi_n((k-1)T_s))} \tag{3.18}$$

Note that all $\Phi_{mod}(t)$ terms when multiplied by M will result in multiples of 2π and, hence, are removed:

$$E_2(kT_s) = A^M(kT_s)A^M((k-1)T_s).e^{j(M\omega T_s + M(\Phi_n(kT_s) - \Phi_n((k-1)T_s))} \tag{3.19}$$

It should be noted that since $\Phi_n(t)$ is a Wiener noise process, it is clear that $(\Phi_n(kT_s) - \Phi_n((k-1)T_s))$ is Gaussian variable with zero mean and variance of $2\pi\Delta\nu T_s$, where $\Delta\nu$ is the sum of the linewidths of the transmitter and LO. The next stage is a moving average filter which operates on $E_2(t)$. If $A(kT_s)$ has a constant mean and variance and since $(\Phi_n(kT_s) - \Phi_n((k-1)T_s))$ is a Gaussian noise process, then with a large enough moving average filter the noise terms, equation (3.19) can be reduced to $E_{MA}(t)$, which is given by:

$$E_{MA}(kT_s) \approx A_{mean}^{2M}.e^{j(M\omega_{est}T_s)} \tag{3.20}$$

where A_{mean} is the average value of $A(kT_s)$. The size of the moving average depends on the system under consideration. The next step is to take the angle of $E_{MA}(t)$ and to divide this by M to give $\Delta\Phi_{est}(t)$:

$$\Delta\Phi_{est}(kT_s) = (\mathrm{mod}(M\omega_{est}T_s + \pi, 2\pi) - \pi)/M \tag{3.21}$$

Since it was assumed that the frequency offset was less than $1/(2MT_s)$, this implies that:

$$\omega_{est} = \pm 2\pi(1/(2MT_s) - \delta_1) \tag{3.22}$$

where ω_{est} is the estimated angular frequency and $0 < \delta_1 \leq 1/(2MT_s)$. From this it can be proven that:

$$\Delta\Phi_{est}(kT_s) = \omega_{est} T_s \tag{3.23}$$

where details of the proof are given in Appendix B. $\Delta\Phi_{est}(t)$ is then accumulated to give the phase trajectory $\Phi_{traj\_freq}(t)$:

$$\Delta\Phi_{traj\_freq}(kT_s) \approx n\omega_{est} T_s + \Phi_{traj\_0} \tag{3.24}$$

where Φ_{traj_0} is the initial value of $\Phi_{traj\_freq}(kT_s)$. $\Phi_{traj\_freq}(kT_s)$ is put into complex form and removed from $E_{in}(kT_s)$ to give the output, $E_{out}(kT_s)$, from the frequency offset compensation scheme:

$$E_{out}(kT_s) = A(kT_s)e^{j\left(kT_s(\omega-\omega_{est})+\Phi_{mod}(kT_s)+\Phi_n(kT_s)+\Phi_0\right)} \tag{3.25}$$

If $\omega \approx \omega_{est}$, then $E_{out}(kT_s)$ will be:

$$E_{out}(kT_s) \approx A(kT_s)e^{j\left(\Phi_{mod}(kT_s)+\Phi_n(kT_s)+\Phi_0\right)} \tag{3.26}$$

Hence, the Mth power frequency offset algorithm shown in Figure 3.7 and described in [24] can remove frequency offsets from M-ary PSK data.

3.4.4 Phase Noise Mitigation: Mth Power Phase Estimation

After frequency offset compensation, it is necessary to perform phase estimation. Note that pilot tone systems can allow for large linewidths to be tolerated [27] but they reduce the maximum possible spectral efficiency. Phase estimation is used to eliminate, as much as possible, the presence of the Wiener phase noise from the received field. This can be achieved by performing Mth power phase estimation as shown in Figure 3.8 below.

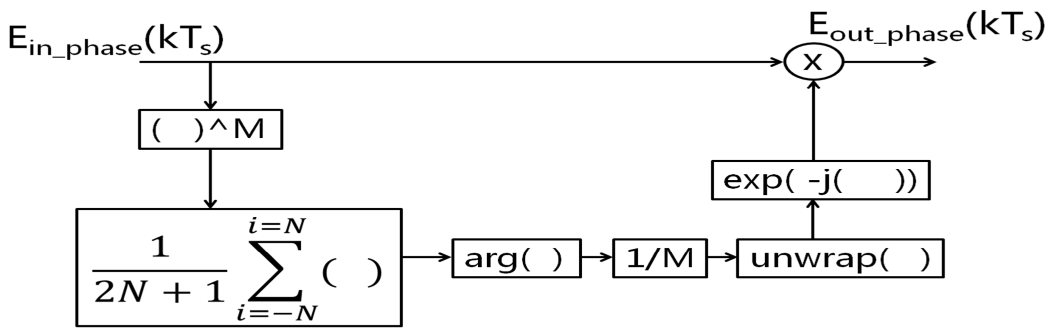

Figure 3.8: Mth power phase estimation (concept from [24]).

For the purposes of clarification, the Mth power algorithm used in frequency offset estimation is focused on using differential phase values while the Mth power algorithm used in phase estimation is focused on using the phase without any differential operation. Here, $E_{in\_phase}(kT_s)$ is simply the output field from the frequency offset compensation stage. The frequency offset will be assumed to have been fully removed so the equation used for the input field will be equation (3.26). $E_{in\_phase}(kT_s)$ is given as:

$$E_{in\_phase}(kT_s) = A(kT_s)e^{j(\Phi_{mod}(kT_s)+\Phi_n(kT_s)+\Phi_0)} \tag{3.27}$$

Firstly, the field is raised to the power of M to give $E_{M\_phase}(kT_s)$ which, as discussed already, removes all $\Phi_{mod}(kT_s)$ terms:

$$E_{M\_phase}(kT_s) = A^M(kT_s)e^{j(M\Phi_n(kT_s)+M\Phi_0)} \tag{3.28}$$

The next stage is the application of a moving average filter to get $E_{MA\_phase}(kT_s)$ in order to get a short term estimate of the phase of the field:

$$E_{MA\_phase}(kT_s) = A^M_{mean\_phase}(kT_s)e^{j(M\Phi_{n\_mean}(kT_s)+M\Phi_0)} \tag{3.29}$$

where $A^M{}_{mean\_phase}(kT_s)$ and $\Phi_{n\_mean}(kT_s)$ are averaged values (not necessarily arithmetic mean values) resulting from the application of the moving average filter, averaging $E_{M\_phase}(kT_s)$ from $((k\text{-}N)T_s)$ to $((k+N)T_s)$. If the size of the moving average (i.e. N) is too large, the average will include uncorrelated phase terms and will lead to inaccuracies. Hence, the size of N needs to be balanced as it needs to be large enough to reduce the influence of additive noise but not too large as to include uncorrelated phase terms. N must be tuned for each given system. Then the angle of $E_{MA\_phase}(kT_s)$ is found and divided by M to give $\Phi_{phase\_est}(kT_s)$:

$$\Phi_{phase\_est}(kT_s) = (\mathrm{mod}(M\Phi_{n\_mean}(kT_s) + M\Phi_0 + \pi, 2\pi) - \pi)/M \tag{3.30}$$

Note that $\Phi_{n\_mean}(kT_s)$ and Φ_0 can be any real number. Hence:

$$\Phi_{phase\_est}(kT_s) = ((M\Phi_{n\_mean}(kT_s) + M\Phi_0 + \pi + 2a_1[k]\pi) - \pi)/M \tag{3.31}$$

where $a_1[k]$ is an integer.

$$\Phi_{phase\_est}(kT_s) = (\Phi_{n\_mean}(kT_s) + \Phi_0 + 2a_1[k]\pi/M) \tag{3.32}$$

$\Phi_{phase\_est}(kT_s)$ can have sudden jumps due to $a_1[k]$ having arbitrary values. These sudden jumps result from $\Phi_{n\_mean}(kT_s)$ changing its value so that the argument of the modulus in equation (3.30) goes into another 2π range. These sudden jumps are mitigated by using an unwrapping function which corrects for sudden jumps which exceed a particular value and this is performed in the following manner (as described in [1]):

$$\begin{aligned}\Phi_{phase\_unwrap}(kT_s) = {} & \Phi_{phase\_est}(kT_s) \\ & + (2\pi/M).f\left[\Phi_{phase\_est}(kT_s) - \Phi_{phase\_est}((k-1)T_s)\right]\end{aligned} \tag{3.33}$$

where,

$$f[x] = \begin{cases} +1, & x < -\pi/M \\ 0, & |x| \leq \pi/M \\ -1, & x > \pi/M \end{cases} \tag{3.34}$$

This results in the unwrapped phase, $\Phi_{phase\_unwrap}(kT_s)$, not having sudden $2\pi/M$ jumps. After this, $\Phi_{phase\_unwrap}(kT_s)$ is removed from $E_{in\_phase}(kT_s)$ in order to mitigate the Wiener phase noise. Note that the unwrapping function assumes that phase jumps due to noise greater than π/M will not occur and in instances where this is not true catastrophic bursts of errors can occur as a constant phase will be added to the estimated phase. These events are known as cycle slips, where a slightly different description of the equivalent event is given in [28].

3.4.5 Hard Decision and Differential Decoding

A key purpose of phase estimation is to ensure that the resulting constellation resembles an M-ary PSK constellation where a hard decision (or slicing) can be performed in order to convert the constellation into discrete data symbols or bits. A problem which remains is determining the absolute phase of the phase data after the hard decision is made. One way to solve this issue is to send known symbols so that the absolute phase offset can be determined. However, if cycle slips occur then there will be large bursts of errors due to loss of absolute phase information. Therefore, it is necessary to regularly send training symbols in case cycle slips occur, which leads to a loss in throughput and increased system complexity. Another method to solve the phase offset issue is to use differential encoding. Here, the phase data at the transmitter, $\theta_{data}[k]$, is differentially encoded to give the encoded phase data, $\theta_{encoded}[k]$:

$$\theta_{encoded}[k] = \theta_{encoded}[k-1] + \theta_{data}[k] \quad (3.35)$$

At the receiver, after the hard decision, the estimated data, $\hat{\theta}_{data}[k_1]$, is calculated:

$$\hat{\theta}_{data}[k_1] = \theta_{rec}[k_1] - \theta_{rec}[k_1 - 1] \quad (3.36)$$

where $\theta_{rec}[k_1]$ is the phase after the hard decision. This will eliminate the need to know the absolute phase offset between the transmitter and receiver and will protect against larger bursts of errors if cycle slips occur since only relative phase changes are required to determine the data sent. Encoding using DDPSK will be explained in a later chapter. Note that some form of forward error correction (FEC) is typically used with data transmission in order to achieve very low BERs. An example forward error correction (FEC) scheme which is able to reduce BERs from $3.2*10^{-3}$ to 10^{-12} using only 6.69% redundancy is given in [29]. Throughout this thesis target BERs of less than or equal to 10^{-3} will be used using the assumption that these BERs can be greatly reduced by using appropriate FEC. In addition, it should be noted that for transmission experiments in the work BERs will invariably be measured using error counting although statistical approaches can also be used such as error vector magnitude or Q-factor [30].

3.5 Penalties for Different Decoding Systems

It should be noted that there are different OSNR penalties associated with different methods of transmitting and decoding M-ary PSK data. Considering the case of single carrier QPSK, the BER versus SNR_b relationship for QPSK is given by [24]:

$$BER\_QPSK = \frac{1}{2}\text{erfc}\left(\sqrt{SNR_b}\right) \quad (3.37)$$

Where BER_QPSK is the BER of QPSK and $\text{erfc}(x)$ is the complementary error function defined as [3]:

$$\text{erfc}(x) = \frac{2}{\sqrt{\pi}}\int_x^{\infty} e^{-t^2}.dt \quad (3.38)$$

Equation (3.37) relates to a system which has no differential encoding (use of known transmitted symbols is assumed), no frequency offsets and no phase noise.

If single differential phase decoding is performed after the hard decision there will be a doubling of errors [1] (due to additive AWGN). This is due to the fact that a single error from AWGN in the hard decision will result in two errors appearing in the decoded phase, once for the $\theta_{rec}[k_1]$ term and once for the $\theta_{rec}[k_1-1]$ term as seen from equation (3.36) (the case where the symbol is detected in the quadrant π radians away, due to noise, is not considered). If single differential decoding for QPSK is done before the hard decision, the BER versus SNR_b for DQPSK without frequency offset and phase noise is given by [3]:

$$\mathrm{BER\_DQPSK} = Q_1(a,b) - \frac{1}{2} I_0(ab) e^{-\left(\frac{a^2+b^2}{2}\right)} \tag{3.39}$$

where $Q_1(a,b)$ is the Marcum Q function given by[3]:

$$Q_1(a,b) = \int_b^{\infty} x e^{-\left(\frac{a^2+x^2}{2}\right)} I_0(ax) dx \tag{3.40}$$

where $I_0(x)$ is the “modified Bessel function of order zero” [3] and is given as [3]:

$$I_0(x) = \sum_{k=0}^{\infty} \left(\frac{x^k}{2^k k!}\right)^2 \tag{3.41}$$

a and b are given as [3]:

$$a = \sqrt{2SNR_b\left(1-\sqrt{\frac{1}{2}}\right)} \tag{3.42}$$

$$b = \sqrt{2SNR_b\left(1+\sqrt{\frac{1}{2}}\right)} \tag{3.43}$$

It is expected that doing differential decoding before the hard decision will result in approximately a 2.4dB penalty with respect to QPSK. Note that the BER versus SNR_b performance associated with doubly differential decoding will be dealt with in a later chapter.

3.6 Summary

It has been shown in this chapter what the main back-to-back impairments to coherent optical communication systems are, along with models used to characterise them. Phase noise characterisation techniques were described. DSP used to mitigate back-to-back impairments along with other necessary DSP steps were described. Finally, the BER versus SNR_b performance of different demodulation systems for QPSK were shown, illustrating the difference between differential decoding before and after the hard decision as well as performance without using differential decoding. The next chapter will focus on improvements which can be made to both static linewidth measurements and switching phase noise/ frequency chirp measurements with the later proving critical for a more complete characterisation of the phase dynamics of fast switching tuneable lasers. The two chapters after that will focus on developing suitable DSP strategies to overcome some of the limitations of standard static coherent system DSP and their variants currently used for coherent optical packet switched networks.

References

1. K. Kikuchi, "Coherent optical communication systems," in *Optical Fiber Telecommunications VB: Systems and Networks,* I. P. Kaminow, T. Li, and A. E. Willner, eds. (Academic Press, Oxford, 2008), pp. 95-130.

2. J. R. Barry and E. A. Lee, "Performance of Coherent Optical Receivers," Proceedings of the IEEE **78,** 1369-1394 (1990).

3. J. G. Proakis and M. Salehi, *Digital Communications, Fifth Edition* (McGraw-Hill, 2008).

4. R. Essiambre, G. Foschini, P. Winzer, and G. Kramer, "Capacity Limits of Fiber-Optic Communication Systems," in *Optical Fiber Communication Conference and Exposition,* (Optical Society of America, 2009), pp. OThL1.

5. A. Yariv, *Optical Electronics in Modern Communications, Fifth Edition* (Oxford University Press, 1997).

6. K. Kikuchi and K. Igarashi, "Characterization of Semiconductor-Laser Phase Noise with Digital Coherent Receivers," in *Optical Fiber Communication Conference and Exposition,* (Optical Society of America, 2011), pp. OML3.

7. Eric W. Weisstein, From MathWorld--A Wolfram Web Resource, "Lorentzian Function." (Accessed 28/04/2015), http://mathworld.wolfram.com/LorentzianFunction.html.

8. K. Shi, F. Smyth, P. M. Anandarajah, D. Reid, Y. Yu, and L. P. Barry, "Linewidth of SG-DBR laser and its effect on DPSK transmission," Optics Communications **283,** 5040-5045 (2010).

9. A. K. Mishra, A. D. Ellis, L. P. Barry, and T. Farrell, "Time-resolved linewidth measurements of a wavelength switched SG-DBR laser for optical packet switched

networks," in *Optical Fiber Communication Conference and Exposition,* (Optical Society of America, 2008), pp. OTuC4.

10. R. Maher and B. Thomsen, "Dynamic linewidth measurement technique using digital intradyne coherent receivers," Optics Express **19,** B313-B322 (2011).

11. K. Shi, R. Watts, D. Reid, T. N. Huynh, C. Browning, P. M. Anandarajah, F. Smyth, and L. P. Barry, "Dynamic Linewidth Measurement Method via an Optical Quadrature Front End," IEEE Photonics Technology Letters **23,** 1591-1593 (2011).

12. J. E. Simsarian and L. Zhang, "Wavelength Locking a Fast-Switching Tunable Laser," IEEE Photonics Technology Letters **16,** 1745-1747 (2004).

13. S. J. Savory, "Digital Coherent Optical Receivers: Algorithms and Subsystems," IEEE Journal of Selected Topics in Quantum Electronics **16,** 1164-1179 (2010).

14. S. J. Savory, "Digital filters for coherent optical receivers," Optics Express **16,** 804-817 (2008).

15. R. Maher, D. S. Millar, S. J. Savory, and B. C. Thomsen, "Widely Tunable Burst Mode Digital Coherent Receiver With Fast Reconfiguration Time for 112 Gb/s DP-QPSK WDM Networks," Journal of Lightwave Technology **30,** 3924-3930 (2012).

16. J. E. Simsarian, J. Gripp, A. H. Gnauck, G. Raybon, and P. J. Winzer, "Fast-Tuning 224-Gb/s Intradyne Receiver for Optical Packet Networks," in *Optical Fiber Communication Conference and Exposition,* (IEEE, 2010), pp. PDPB5.

17. L. Liu, Z. Tao, W. Yan, S. Oda, T. Hoshida, and J. C. Rasmussen, "Initial Tap Setup of Constant Modulus Algorithm for Polarization De-multiplexing in Optical Coherent Receivers," in *Optical Fiber Communication Conference and Exposition,* (IEEE, 2009), pp. OMT2.

18. J. Gripp, J. E. Simsarian, S. Corteselli, and T. Pfau, "Wavelength-Tunable Burst-Mode Receiver with Correlation-Based Polarization Separation," in *European Conference and Exhibition on Optical Communication,* (IET, 2013), pp. Th.2.A.3.

19. I. Tselniker, A. Tolmachev, and M. Nazarathy, "Multiplier-Free Joint Carrier Recovery for 16-QAM Synchronous or Agile Burst Receivers," IEEE Photonics Technology Letters **25,** 2133-2136 (2013).

20. J. C. M. Diniz, E. S. Rosa, V. B. Ribeiro, J. C. R. F. Oliveira, and A. C. Bordonalli, "Wide-Range Frequency Offset Estimator for DSP-based Optical Coherent Receivers," in *International Microwave & Optoelectronics Conference,* (IEEE, 2011), pp. 710-713.

21. A. Leven, N. Kaneda, U. -V. Koc, and Y. -K. Chen, "Frequency Estimation in Intradyne Reception," IEEE Photonics Technology Letters **19,** 366-368 (2007).

22. T. N. Huynh, L. Nguyen, V. Vujicic, and L. P. Barry, "Pilot-Tone-Aided Transmission of High-Order QAM for Optical Packet Switched Networks," Journal of Optical Communications and Networking **6,** 152-158 (2014).

23. S. Shinada, M. Nakamura, Y. Kamio, and N. Wada, "16-QAM Optical Packet Switching with Real-time Self-homodyne Detection using Polarization-multiplexed Pilot-carrier," in *European Conference and Exhibition on Optical Communications,* (IEEE, 2012), pp. We.2.A.2.

24. X. Liu, S. Chandrasekhar, and A. Leven, "Self-coherent optical transport systems," in *Optical Fiber Telecommunications VB: Systems and Networks,* I. P. Kaminow, T. Li, and A. E. Willner, eds. (Academic Press, Oxford, 2008), pp. 131-178.

25. Y. Gao, A. P. T. Lau, and C. Lu, "Residual Carrier-Aided Frequency Offset Estimation for Square 16-QAM Systems," in *OptoElectronics and Communications Conference/ International Conference on Photonics in Switching,* (IEEE, 2013), pp. TuPR-8.

26. A. J. Walsh, H. Shams, J. Mountjoy, A. Fagan, J. Zhao, L. P. Barry, and A. D. Ellis, "Demonstrating Doubly-Differential Quadrature Phase Shift Keying in the Optical Domain," IEEE Photonics Technology Letters **25,** 1054-1057 (2013).

27. M. Nakamura, Y. Kamio, and T. Miyazaki, "Linewidth-tolerant 10-Gbit/s 16-QAM transmission using a pilot-carrier based phase-noise cancelling technique," Optics Express **16,** 10611-10616 (2008).

28. E. Ibragimov, B. Zhang, T. J. Schmidt, C. Malouin, N. Fediakine, and H. Jiang, "Cycle Slip Probability in 100G PM-QPSK Systems," in *Optical Fiber Communication Conference and Exposition,* (Optical Society of America, 2010), pp. OWE2.

29. K. Seki, K. Mikami, A. Katayama, S. Suzuki, N. Shinohara, and M. Nakabayashi, "Single-chip FEC codec using a concatenated BCH code for 10 Gb/s long-haul optical transmission systems," in *Proceedings of the IEEE Custom Integrated Circuits Conference,* (IEEE, 2003), pp. 279-282.

30. F. Zhang, Y. Luo, Y. Wang, L. Li, L. Zhu, Z. Chen, and C. Wu, "Experimental Comparison of Different BER Estimation Methods for Coherent Optical QPSK Transmission Systems," IEEE Photonics Technology Letters **23,** 1343-1345 (2011).

Chapter 4

Characterising Static and Switching Laser Phase Dynamics to Aid Coherent System Design

In this chapter, laser phase dynamics characterisation techniques (frequency chirp as well as static and dynamic laser phase noise) for both static and switching lasers will be described. The laser phase dynamics investigated can be considered to be phase impairments to coherent optical communications systems. The effects of laser phase impairments on the transmission performance of phase modulated data will be investigated. Novel work concerning the simultaneous characterisation of both transient frequency offsets and dynamic laser phase noise of a fast switching tuneable laser will be presented. Independent confirmation of the validity of this approach will be provided where expected time-resolved BER curves from the laser phase dynamics characterisation will be compared with measured time-resolved BER curves from a transmission experiment using the same fast switching tuneable laser with very close matching observed. The motivation of characterising these phase dynamics is to aid coherent optical communication system design, in particular, for coherent optical packet/ burst scenarios.

4.1 Independent Differential Phase Values for Correct Calculation of Wiener Phase Noise

It was explained in the previous chapter in section 3.32 that the instantaneous phase of a laser, $\Phi(t)$, can be acquired using a polarisation diverse coherent receiver, where the laser under test is the signal input to the polarisation diverse coherent receiver and a low linewidth static laser is the LO input, which is typically an ECL in this work. The polarisation controllers are set so as to maximise the power appearing on one polarisation output from the polarisation diverse coherent receiver, denoted here as the x-polarisation. The frequency offset between the laser under test and the low linewidth stable laser is reduced to a value that is below the bandwidth of the electronics. This is achieved by tuning the frequency of the low linewidth laser and any remaining constant frequency offset is removed in DSP.

To begin with, the linewidth of a static laser will be characterised. Re-iterating a key equation here in relation to Wiener phase noise, the variance of the differential phase noise, $\sigma_{\Phi}^{2}(T_{int})$, is given as [1] (using slightly different notation to [1]):

$$\sigma_{\Phi}^{2}\left(T_{int}\right) = 2\pi\Delta\nu T_{int} \tag{4.1}$$

Where $\Delta\nu$ is the linewidth and T_{int} is the time interval between two phases used to calculate the differential phase. $\sigma_{\Phi}^{2}(T_{int})$ can be expressed as:

$$\sigma_{\Phi}^{2}\left(T_{int}\right) = \left\langle \left(\Phi_{n}\left(t + T_{int}\right) - \Phi_{n}\left(t\right)\right)^{2} \right\rangle \tag{4.2}$$

where $\Phi_n(t)$ is the instantaneous phase noise with all constant frequency offset removed. It is assumed that the phase noise from the low linewidth laser is negligible compared with the phase noise of the laser under test.

The coherent receiver method of calculating linewidth, explained in the previous chapter, utilises equations (4.1) and (4.2). Here we show, for the first time, that the method used to select phase noise points to calculate the variance of the differential phase noise is critical to determining the correct value of the linewidth. Shown in Figure 4.1 below are two different methods for selecting phase noise points to determine differential phase values. These values are used to calculate the variance of the differential phase in order to determine a plot of variance of differential phase noise versus time interval so that the linewidth can be calculated using equation (4.1).

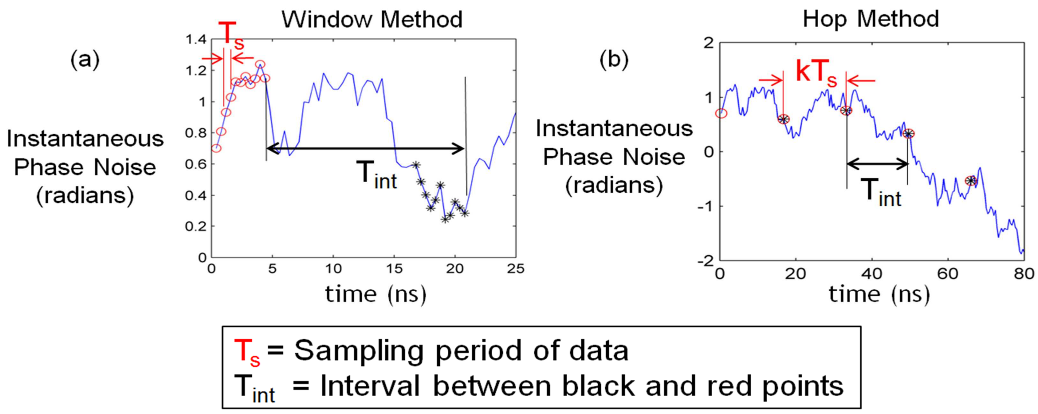

Figure 4.1: Different methods of selecting differential phase values to calculate static linewidth, designated as (a) the "Window Method" and (b) the "Hop Method" using simulation data, for a linewidth of 10MHz and a sampling period of 400ps (k is a positive integer).

For the “Window Method” shown in Figure 4.1 (a), the $\Phi_n(t)$ terms (red circles) are all selected serially with only the sample period between them and the $\Phi_n(t+T_{int})$ terms (black stars) are determined by the particular value of time interval, T_{int}, used. As can be seen from Figure 4.1 (a), for large time intervals, the interval between any $\Phi_n(t+T_{int})$ and $\Phi_n(t)$ pair will have a large common overlap with the interval between any other $\Phi_n(t+T_{int})$ and $\Phi_n(t)$ pair, meaning the instantaneous phase noise trajectories used by different pairs will have some parts identical to each other. Hence, it should be expected that the variance of $(\Phi_n(t+T_{int})-\Phi_n(t))$ calculated using the “Window Method” will not, on average, be statistically correct for large time intervals. The second method is the “Hop Method”, illustrated in Figure 4.1 (b) where the values of $\Phi_n(t)$ are selected so that the time difference between any two selected $\Phi_n(t)$ points is equal to the time interval being used and the values of $\Phi_n(t+T_{int})$ are determined by the particular value time interval. This will mean that the intervals between $\Phi_n(t+T_{int})$ and $\Phi_n(t)$ will always be statistically independent and, hence, will correctly calculate of the variance. Example curves of the variance of the differential phase noise versus time interval are given in Figure 4.2 below using simulation data, four runs of each method are shown.

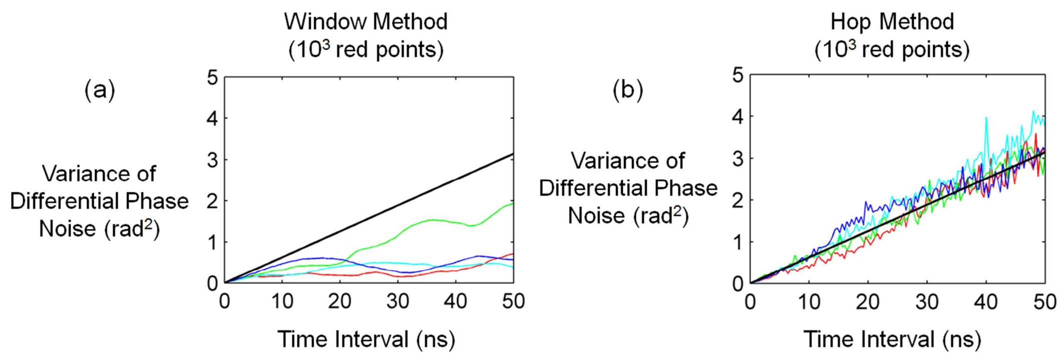

Figure 4.2: Plots of variance of differential phase noise versus delay for (a) the "Window Method" and (b) the "Hop Method" using simulation data with linewidth calculated over 50ns. The black lines indicate the expected relationship and the other colours show different simulation runs of calculated variance of differential phase noise versus delay.

The linewidth of the laser under test in the simulation was 10MHz. It can be seen from Figure 4.2 (a) that the “Window Method” did not result in a straight line relationship between variance and delay for large time intervals. The curve is linear for small time intervals but eventually starts to vary randomly. The “Hop Method” results are shown in Figure 4.2 (b) which had very straight lines. This is attributed to the fact that all the pairs of $\Phi_n(t+T_{int})$ and $\Phi_n(t)$ used to calculate the variance did not have overlapping intervals which meant that all the values used to calculate the variance were statistically independent. Using the data shown in Figure 4.2, the correlation coefficient for the “Window Method” was in one curve as low as 0.4780, while all the correlation coefficients for the “Hop Method” were greater than 0.9685. In order to reduce error in the calculated curves and the calculated linewidths, a longer phase noise trajectory should be acquired so that more points can be used to calculate the variance. Hence, it has been clearly demonstrated that the method of selecting points to calculate the differential phase is critical to ensuring that the correct linewidth value is calculated. While the “Window method” can produce approximately linear curves from small time intervals it is not guaranteed to do so for larger time intervals while the “Hop method” will produce linear curves for both small and large time intervals. Shown in Figure 4.3 is an example of both methods being applied to experimental data measuring the linewidth of the largest mode of a multi-mode laser. The linewidths calculated were 4.6MHz using the “Window method” (red curve) and 9.5 MHz using the “Hop Method” (blue curve). For Figure 4.3, the low linewidth LO used was an ECL (Agilent Technologies “N7711A Tunable Laser Source” with a specified typical linewidth of less than 100kHz).

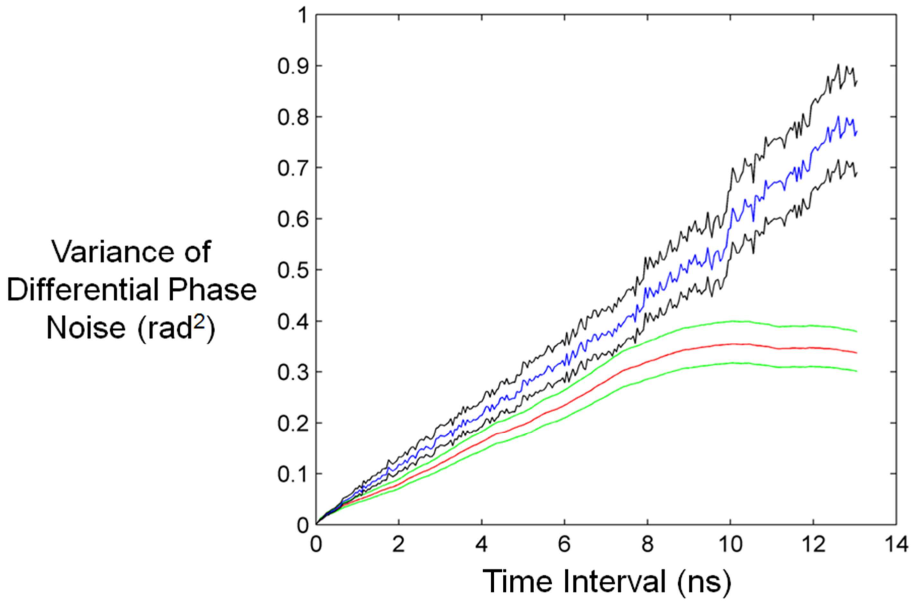

Figure 4.3: Plot of variance of differential phase noise versus time delay using the “Window Method” (red), and the "Hop Method" (blue) using experimental data, with the green and black lines indicating the 99% confidence intervals for the “Window Method” and “Hop Method” respectively.

Similar to the simulation results, the "Hop Method" was linear while the "Window Method" was not linear for large time intervals. It is possible to put confidence intervals on each individual variance of the differential phase noise point by using the method in [2] which is based on using the Chi-square distribution. For estimates which use more than 101 values to calculate the variance, the 99% confidence limits (divided by the sample estimated variance) are approximately given by (based on information in [2]):

$$\frac{c_1}{s^2} = \frac{2(N-1)}{\left(\sqrt{(2N-3)} - 2.58\right)^2} \tag{4.3}$$

$$\frac{c_2}{s^2} = \frac{2(N-1)}{\left(\sqrt{(2N-3)} + 2.58\right)^2} \tag{4.4}$$

where c_1 is the upper confidence limit, s^2 is the sample estimated variance, N is the number of sample values used and c_2 is the lower confidence limit. For $N=10^3$, the confidence interval is given as $CONF_{99}\{0.8934*s^2 < \sigma_{\Phi}^2(T_{int}) < 1.1257*s^2\}$, where s^2 is an estimated sample variance. This confidence interval for $N=10^3$ applies to Figure 4.2 and Figure 4.3 which both use 10^3 samples for each variance calculation. Confidence intervals are shown in Figure 4.3 for with green curves for the "Window Method" and black curves for the "Hop Method".

4.2 Time-Resolved Phase Impairment Characterisation

As discussed in the previous chapter, various time-resolved phase noise measurement schemes have been developed. Separately, time-resolved frequency chirp can also be measured. However, there are three key limitations associated with the current state of the art of characterising time-resolved phase impairments of a tuneable laser which is switching wavelengths. Firstly, the phase noise characterisation techniques usually assume a Wiener phase noise process which may not necessarily be the case. Secondly, it will be shown that it is necessary to consider both phase noise and frequency chirp together rather than separately in order to correctly predict performance in a switching scenario. Thirdly, there can potentially be ambiguity in distinguishing between frequency chirp and varying phase noise directly after a laser has switched wavelengths and having a method that jointly describes both frequency chirp and dynamic phase noise will help avoid this ambiguity as will be shown. In this work, both limitations will be overcome through the use of time-resolved 3-dimensional (3D) complementary cumulative distribution functions (CCDFs) of the differential phase.

A CCDF of a random variable is 1 minus the distribution function of the random variable. By building up the CCDF of the differential phase, the frequency chirp and phase noise are simultaneously taken into account. The mean differential phase at a particular point in time can be interpreted as being equivalent to the deterministic frequency chirp at that particular time, while the shape and variance of the distribution at that particular time is determined by the phase noise present at that particular time. It will be shown that the CCDF of the differential phase can calculate expected errors of DQPSK systems during a switching event, due to the presence of both frequency chirp and phase noise. Note that many details of this novel CCDF work were published in [3]. The flow diagram shown in Figure 4.4 provides a general overview of the DSP processes involved.

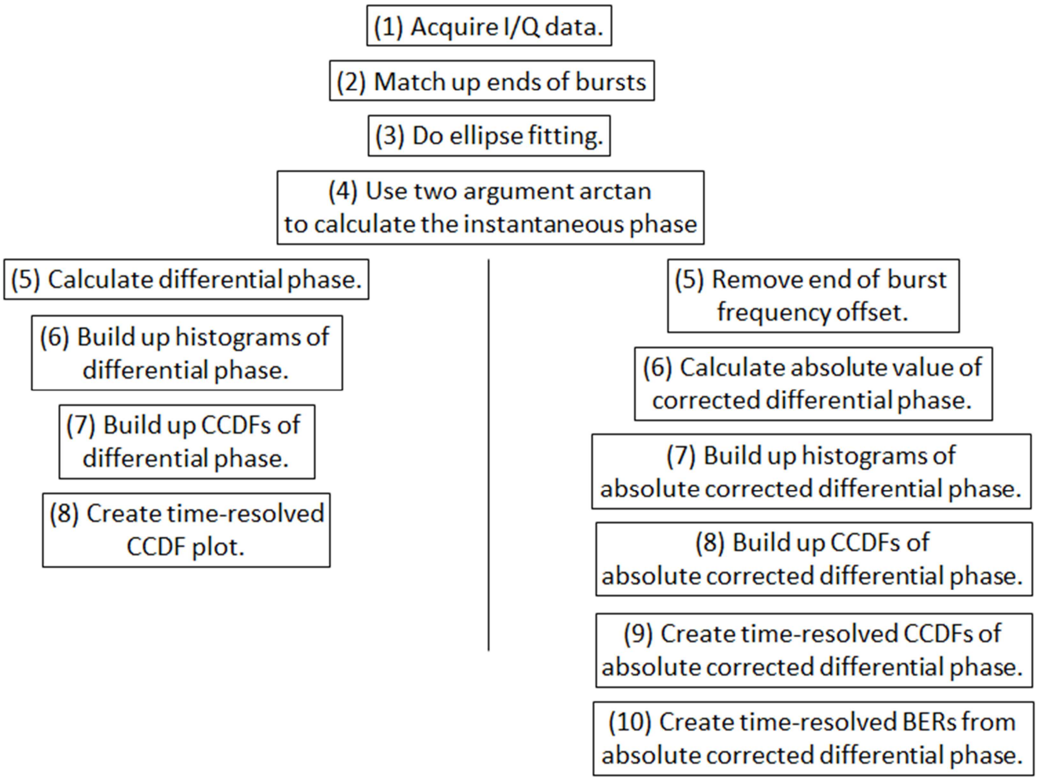

Figure 4.4: Flow diagram of the DSP processes involved with calculating time-resolved CCDFs, where steps (5) to (8) on the left are followed in order to determine the CCDF of the differential phase while (5) to (10) on the right are followed if the CCDF of the absolute corrected differential phase is required along with the CCDF calculated time-resolved BER.

4.2.1 Acquiring and Aligning Bursts

The switching laser which was tested was an SG-DBR laser which was switched between 1548nm and 1560nm by applying a switching signal to the back section of the SG-DBR where the switching signal had a period of 149.5ns (frequency 6.7 MHz). The low linewidth laser used at the LO was an ECL, (Agilent Technologies "N7711A Tunable Laser Source" with a specified typical linewidth of less than 100kHz). The ECL was set to 1548nm so that the switching wavelength near this would be the one characterised. The phase dynamics of only one polarisation was characterised. The coherent receiver provided Ix, Qx, Iy and Qy outputs, where only the Ix and Qx values were recorded (both with the same polarisation). 80 of the switches (consecutive switches) which were recorded by the real-time scope in a single screen shot were used and 127 screen shots were used in [3]. It was necessary to analyse multiple switches in order to build up a distribution of the differential phase at a particular time after a switching event. It was therefore critical that different switches be aligned together correctly (i.e. identify a marker in time for each burst which designates the end of a burst). This was achieved by finding the first sample point when the Ix current falls below 10mV (approximately 50% of the amplitude during a switch) for each switch and aligning switches based on when this drop occurs. It was decided that it was more accurate to align the switches with the ends of the bursts rather than the beginnings as the amplitude transitions at the ends of the bursts were much sharper than at the beginnings of the bursts. There is an error associated with aligning the bursts with this method since the point which drops below 10mV will be determined with a resolution limited by the period of the beat signal at the end of a burst. For increased accuracy, a linear fit of these end points in a given screen shot was calculated as the end points were expected to be periodic. It was expected that by using linearly fitted points, this would reduce the error associated with having a resolution limited by the period of the beat signal (discussed above) and reduce errors associated with the noise of the beat signal. A plot showing Ix with the linearly fitted burst end points is shown in Figure 4.5. Amplitude offsets, power differences and timing skews present in Ix and Qx were then corrected in DSP by fitting the Ix, Qx parameter plots to an ellipse and using the ellipse fit parameters to fix Ix and Qx, where the ellipse fitting code was from [4] with the mathematics coming from [5] and [6]. The values of Ix and Qx are then then used in a two argument arctan whose output is unwrapped in order to produce an instantaneous phase trajectory for a given burst, $\Phi_{coh}(t)$, where t is the time after the start of the burst.

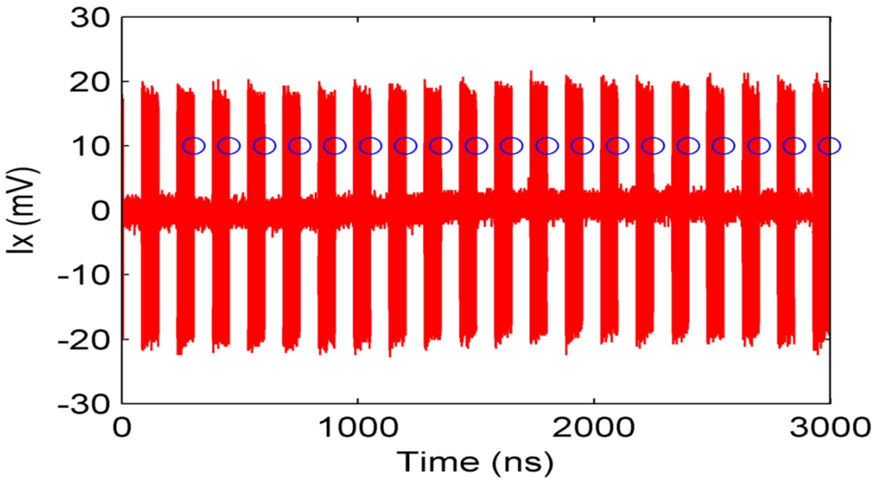

Figure 4.5: Plot of Ix versus time (red) with the linearly fitted locations of the end points (blue circles). Note that the first drop is excluded in case the burst is not entirely captured.

4.2.2 Analysis of the Instantaneous Phase of a Switching Laser

Assuming the ECL phase noise is negligible compared with the phase noise of the switching SG-DBR laser, the phase noise from the ECL will not need to be considered in the analysis The measured instantaneous phase of the SG-DBR, $\Phi_{coh}(t)$, is given as:

$$\Phi_{coh}(t) = \omega(t).t + \Phi_n(t) + \Phi_0 \qquad (4.5)$$

where t is the time after the start of a switching event. $\omega(t)$ is the instantaneous frequency offset between the switching SG-DBR and the ECL. $\Phi_n(t)$ is the phase noise of the switching SG-DBR. Φ_0 is the initial phase. The instantaneous frequency offset can be written as:

$$\omega(t) = \omega_{SG-DBR\_chirp}(t) + \left(\omega_{SG-DBR\_const} - \omega_{ECL}\right) \qquad (4.6)$$

where $\omega_{SG-DBR\_chirp}(t)$ represents the time-varying angular frequency chirp of the SG-DBR, which will be in the range: $(\omega_{SG-DBR\_chirp}(t)/2\pi)\epsilon$[-5GHz, 5GHz]. Any laser which exhibits frequency chirp outside this range would be considered unsuitable for coherent OPS or coherent OBS. ω_{SG-DBR_const} represents the constant angular frequency component. ω_{SG-DBR_const} will be in a similar range to the C-band: $(\omega_{SG-DBR\_const}/2\pi)$ ϵ [191.6 THz, 195.9 THz]) with the C-band wavelength range given in [7]. ω_{ECL} represents the ECL constant angular frequency, where $(\omega_{ECL}/2\pi)$ will be within 10GHz of $(\omega_{SG-DBR\_const}/2\pi)$.

The value which was characterised in this work was the differential phase of the SG-DBR laser, $\Delta\Phi_{coh}(t)$, which is given by:

$$\Delta\Phi_{coh}(t) = \Phi_{coh}(t) - \Phi_{coh}(t - T_{int}) \quad (4.7)$$

If equations (4.5) and (4.6) are substituted in equation (4.7), this yields:

$$\begin{aligned}\Delta\Phi_{coh}(t) &= \left(\omega_{SG-DBR\_chirp}(t) - \omega_{SG-DBR\_chirp}(t - T_{int})\right).t \\ &+ T_{int}\omega_{SG-DBR\_chirp}(t - T_{int}) + \left(\omega_{SG-DBR\_const} - \omega_{ECL}\right)T_{int} \\ &+ \Phi_n(t) - \Phi_n(t - T_{int})\end{aligned} \quad (4.8)$$

In this analysis, $T_{int}=2T_s$, where T_s is the sampling period of the real-time scope which is 50ps resulting in T_{int}=100ps. Examples of the measured instantaneous phase and calculated differential phase are shown in Figure 4.6. The 0ns time represents the start of the switch while the 74.8ns time represents the end of the switch.

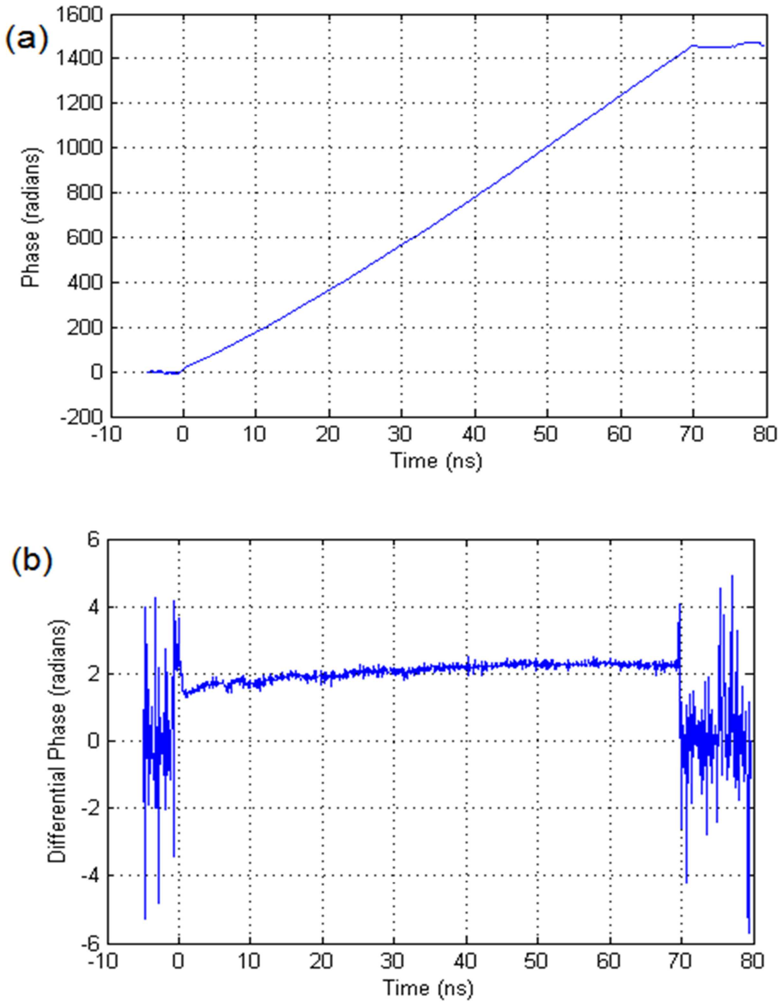

Figure 4.6: Plots of (a) instantaneous phase of the switching SG-DBR versus time and (b) differential phase of the switching SG-DBR versus time. There is no light present at 1548nm at the edges of the measurements making results before 0ns and after 70ns unreliable.

4.2.3 Creating Distributions of the Differential Phase

The next step was to build up distributions of the differential phase. Note that residual frequency offset between the SG-DBR steady-state frequency and the ECL frequency was observed over the 50ns to 65ns section with a maximum frequency error of 160 MHz which corresponds to a maximum phase error of 0.1005 radians over 100ps. Shown in Figure 4.7 is a histogram of the differential phase 5.1ns after a tuneable laser has switched wavelengths. Also shown in Figure 4.7 is the CCDF of the differential phase 5.1ns after the switch. Note that the differential phase is calculated over 100ps (two samples per symbol), which is the time resolution of this measurement scheme (the time resolution can be made finer by using only one sample per symbol or by increasing the sampling rate).

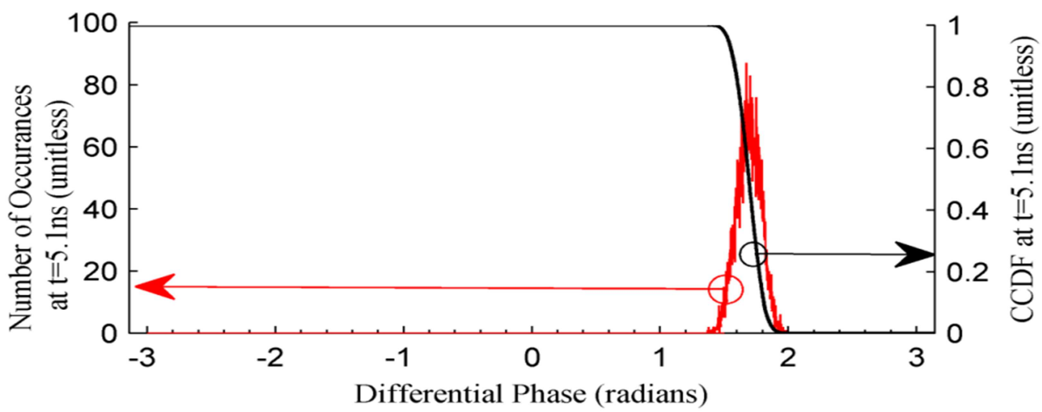

Figure 4.7: Plot showing both a histogram (red) and CCDF (black) of the differential phase 5.1ns after a switching event [3].

If a number of CCDF plots of the differential phase are connected together in time it is possible to create a time-resolved 3D CCDF plot of the differential phase as shown in Figure 4.8. The x-axis is time, where zero represents the start of the switch, the y-axis is the differential phase in radians and the colour represents the probability of the differential phase being greater than the differential phase at that particular point and at that particular time (whose corresponding probability values are given by the colour-bar on the right of the plot). Hence, Figure 4.8 fully captures all of the phase dynamics, both frequency and phase noise, of a fast switching tuneable laser directly after a switching event, which is exactly what is required to determine the performance in a coherent transmission system. Note that the vertical white line at 5.1ns in Figure 4.8 is a single CCDF slice that is shown by the black CCDF curve in Figure 4.7. It can be seen in Figure 4.8 that the average differential phase (or frequency chirp, which is approximately the green colour in the 3D plot) varies greatly in the first 20ns and starts to settle after about 45ns. It also appears that the phase noise (interpreted as the spread of the distribution) appears on visual inspection to be relatively constant after 5ns and this is further evidenced by the plot of the interquartile range of the distribution of the differential phase versus time in Figure 4.9. The interquartile range is the change in differential phase between the 0.25 and 0.75 probability points in a CCDF and it gives an indication of the spread of the distribution.

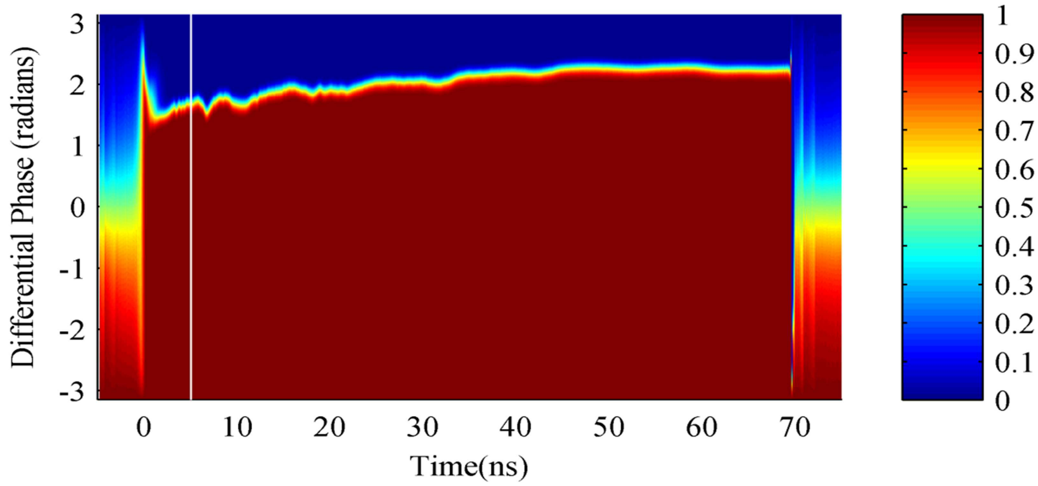

Figure 4.8: Plot of a time-resolved CCDF of the differential phase at the 1548nm wavelength after a switching event where the vertical white line indicates the position of the CCDF in Figure 4.7 and the colour-bar indicates the probability that the differential phase exceeds a particular value at a particular time [3].

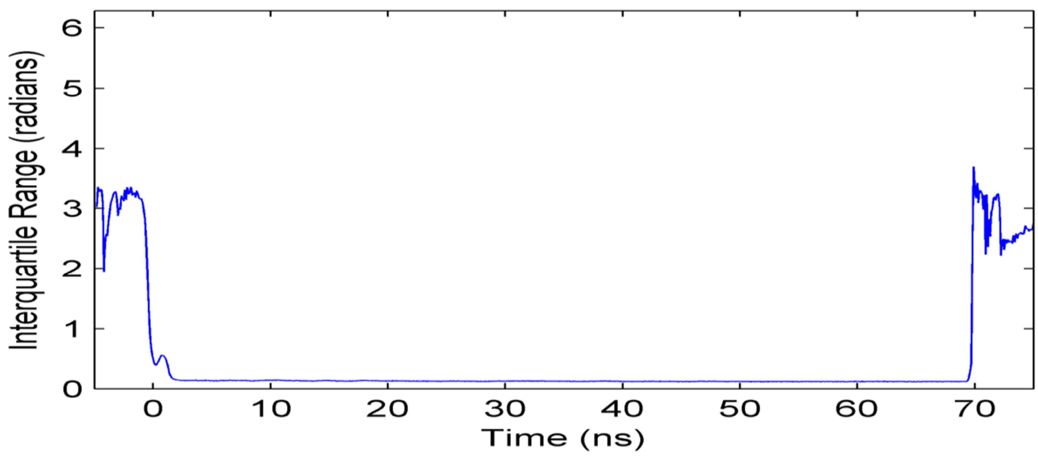

Figure 4.9: Plot of the interquartile range of the distribution of the differential phase versus time at the 1548nm wavelength. There is no light present at 1548nm at the edges of the measurements making results before 0ns and after 70ns unreliable.

4.2.4 Verifying Accuracy of 3D CCDF of the Differential Phase

The next step was to verify the accuracy of this method and to verify that it did capture all of the phase dynamics of the switching tuneable laser. One way to do this was to calculate the expected time-resolved BER of DQPSK using CCDFs of the differential phase and to then compare this to a measured time-resolved BER from a transmission experiment which uses the same switching laser to transmit DQPSK. For a DQPSK system, the BER due to phase impairments only (frequency offset and phase noise but not taking into account amplitude noise) can be determined from the probability distribution function of the differential phase using the following equation [3]:

$$\mathrm{BER}(t) = \frac{1}{2}\mathrm{P}\left(\frac{3\pi}{4} > \left|\Delta\Phi_{\mathrm{coh-cor}}(t)\right| \geq \frac{\pi}{4}\right) + \mathrm{P}\left(\left|\Delta\Phi_{\mathrm{coh-cor}}(t)\right| \geq \frac{3\pi}{4}\right) \qquad (4.9)$$

where $\mathrm{BER}(t)$ is the time-resolved BER, $\Delta\Phi_{\mathrm{coh\text{-}cor}}(t)$ is the "corrected differential phase" of the SG-DBR where the average of the slopes of the instantaneous phase from 50ns to 65ns, i.e. the steady-state frequency offset, has been removed before calculating the differential phase. The justification for (4.9) is that the left bracket is the probability that that the absolute corrected differential phase will cause a DQPSK symbol to appear in an adjacent quadrant. This means that the absolute corrected differential phase is greater than or equal to $\pi/4$ and less than $3\pi/4$. Due to Gray coding, this will only result in one of the two bits of the symbol having an error, hence, the multiplication by 1/2. The right bracket is the probability that the absolute corrected differential phase will result in the symbol shifting to the non-adjacent quadrant. Hence, the absolute corrected differential phase will be greater than or equal to $3\pi/4$. Due to Gray coding, this will cause two bit errors for that symbol and, therefore, the BER for this event is the same as the probability of this event.

After removing the frequency offset at the end of the burst from the instantaneous phase using DSP to get the corrected instantaneous phase, the corrected differential phase was calculated. Then, histograms of the absolute value of the corrected differential phase, $|\Delta\Phi_{\mathrm{coh\text{-}cor}}(t)|$, were calculated, from which CCDFs of the absolute value of the corrected differential phase could be calculated. This allowed for a time-resolved CCDF of the absolute corrected differential phase to be determined as shown in Figure 4.10. The white horizontal lines indicate the CCDF values required to calculate $\mathrm{BER}(t)$ using equation (4.9) as they are at $3\pi/4$ and $\pi/4$. The right hand side probability of equation (4.9) is equal to the values at the $3\pi/4$

horizontal line and left hand side probability is equal to the values at the $\pi/4$ white line minus the values at the $3\pi/4$ white line with the result multiplied by 1/2. The net result of this calculation is given by the red line in Figure 4.11. The next step is to explain how the time-resolved BER of DQPSK transmission was directly measured. This was required so that a comparison between the CCDF time-resolved BER and the directly measured time-resolved BER could be made. By making this comparison, it was possible to ascertain the accuracy of characterising phase dynamics using a time-resolved CCDF of the differential phase.

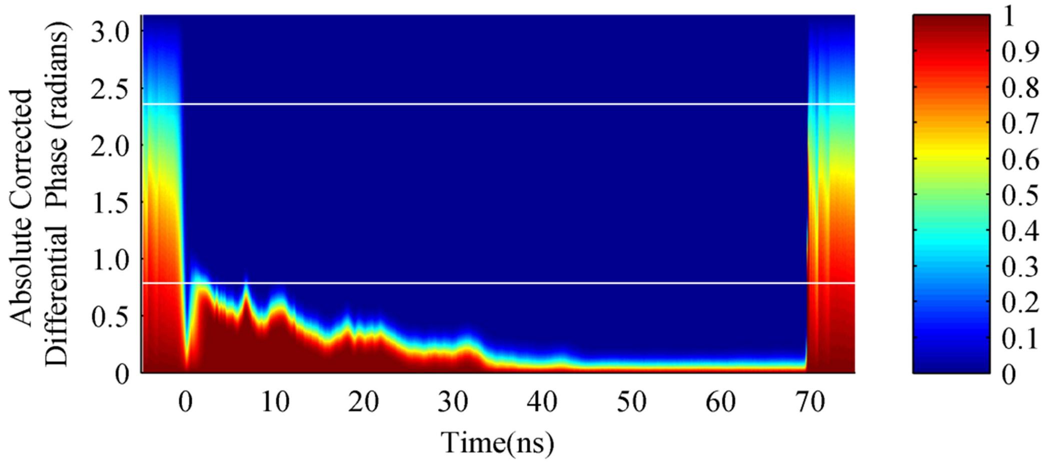

Figure 4.10: Plot of the time-resolved CCDF of the absolute corrected differential phase after a switching event where the horizontal white lines indicate the $\pi/4$ and $3\pi/4$ values which are required for calculating the time-resolved BER [3].

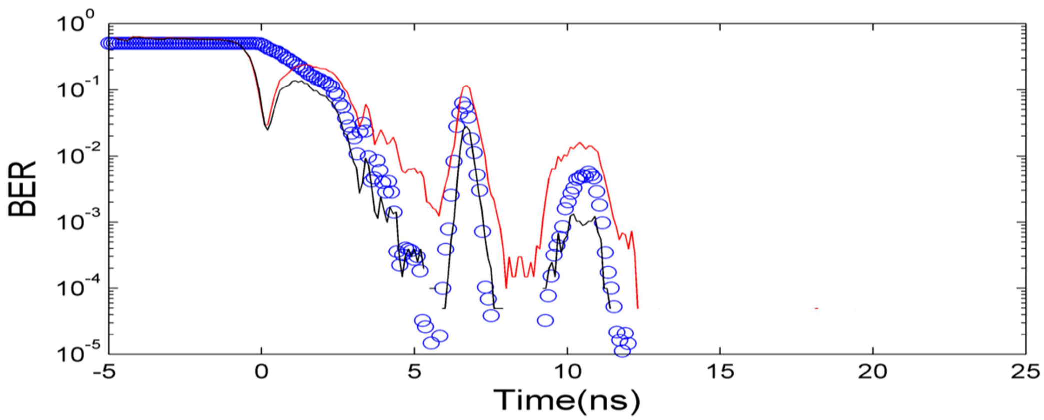

Figure 4.11: Plot of the time-resolved BER using direct error counting [8] (blue circles), using the CCDF in Figure 4.10 (red line) and using a CCDF with an optimised steady-state frequency offset removed to match the direct error counting BER (black line) [3]. For this time-resolved BER plot, the ECL was near 1548nm.

4.2.4.1 Time-Resolved BER Measurement Using Direct Error Counting

Previous work on time-resolved BER measurements using direct error counting includes a time-resolved BER measurement scheme which used a gating system to observe BER values within 2ns sections of the switching event, giving it a resolution of approximately 21 symbols [9]. This 2ns window could be moved with a resolution of approximately 1 symbol (100ps). However, time-resolved BER measurements of tuneable laser switching events have a highest possible resolution in time, which is equal to the symbol rate of the data transmission. In addition, the method in [9] would be time-consuming to use in practice due to the need to move the 2ns gating position many times in order to build up a time-resolved BER profile. Maximum time resolution and fast acquisition time can both be achieved using a field-programmable gate array (FPGA) approach as described in [10] (Note that this FPGA measured Time-Resolved BER work was mainly carried out by John A. O'Dowd and Vivian M. Bessler). This system worked on the basis that the FPGA acted as a pattern generator and a bit error rate tester (BERT). The errors that were recorded by the FPGA were assigned to different points in time (or bit slots) relative to the start of a switching event as the FPGA had access to the signal that switched the wavelength of the SG-DBR laser. The FPGA compared the number of errors to the number of transmitted bits in a given time slot to calculate the BER in each time slot of the burst length. This resulted in a time-resolved BER system being achieved where time-resolved BERs were measured for switching lasers using phase modulation schemes such as differential phase shift keying (DPSK) [10] and DQPSK [8] where in both cases a delay interferometer was used in the receiver.

As was seen from chapter 2, the output current from a delay interferometer, $I_{PD}(t)$, is given by:

$$I_{PD}(t) = \mathrm{Re}[K.E_{RX}(t)E^{*}_{RX}(t - T_{int})] \tag{4.10}$$

where $E_{RX}(t)$ is the field before it enters the interferometer, T_{int} is the relative delay between the two arms (usually set to be equal to the symbol period) and K is a constant. Note that K is positive. For a fast switching tuneable laser the field will be given as:

$$E_{RX}(t) = A(t).e^{j.(\omega_{int}(t)t+\Phi_{mod}(t)+\Phi_{n}(t)+\Phi_{0})} \tag{4.11}$$

where $A(t)$ is the amplitude of the wave, $\omega_{int}(t)$ is the angular frequency containing chirp, $\Phi_{mod}(t)$ is the phase modulation, $\Phi_n(t)$ is the phase noise and Φ_0 is the initial phase. Note that $A(t)$ is positive. Combining equations (4.10) and (4.11) yields:

$$I_{PD}(t) = \mathrm{Re}[K.A(t)A(t - T_{int}) \\ .e^{j(\omega_{int}(t)t - \omega_{int}(t-T_{int})(t-T_{int}) + \Phi_{mod}(t) - \Phi_{mod}(t-T_{int}) + \Phi_n(t) - \Phi_n(t-T_{int}))} \tag{4.12}$$

which can be reduced to:

$$I_{PD}(t) = K.A(t)A(t - T_{int}) \\ .\cos\begin{pmatrix} \omega_{int}(t)t - \omega_{int}(t - T_{int})(t - T_{int}) \\ + \Phi_{mod}(t) - \Phi_{mod}(t - T_{int}) + \Phi_n(t) - \Phi_n(t - T_{int}) \end{pmatrix} \tag{4.13}$$

If the phase terms, excluding $\Phi_{mod}(t)$ and $\Phi_{mod}(t\text{-}T_{int})$, are combined into one differential phase term, $\Delta\Phi_{ni}(t)$:

$$\Delta\Phi_{ni}(t) = \omega_{int}(t)t - \omega_{int}(t - T_{int})(t - T_{int}) + \Phi_n(t) - \Phi_n(t - T_{int}) \tag{4.14}$$

Hence, equation (4.13) can be written as:

$$I_{PD}(t) = K.A(t)A(t - T_{int})\cos(\Delta\Phi_{ni}(t) + \Phi_{mod}(t) - \Phi_{mod}(t - T_{int})) \tag{4.15}$$

For DQPSK, the value of $(\Phi_{mod}(t)\text{-}\ \Phi_{mod}(t\text{-}T_{int}))$ will be an element of $\{0,\pi/2,\pi,3\pi/2\}$. A possible Gray coding format which could be used is shown in Figure 4.12 (a), where the constellation represents the total phase in the cosine argument in equation (4.15) and for Figure 4.12 (a), $\Delta\Phi_{ni}(t)$ is set to zero.

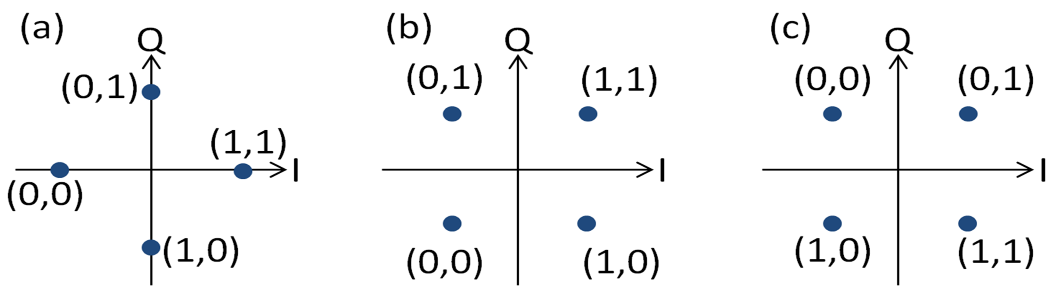

Figure 4.12: Possible Gray coding for DQPSK symbols with (a) $\Delta\Phi_{ni}(t)=0$ (b) $\Delta\Phi_{ni}(t)=\pi/4$ for the first interferometer and (c) $\Delta\Phi_{ni}(t)=-\pi/4$ for the second interferometer.

If the first interferometer is able to maintain the value of $\Delta\Phi_{ni}(t)$ equal to $\pi/4$, by varying the value of T_{int}, the constellation will be rotated as shown in Figure 4.12 (b). It can be seen from Figure 4.12 (b) that the sign of the real value indicates the first bit (one if positive and zero if negative). Since taking the cosine of the argument and multiplication by the magnitude is the same as taking the real part, equation (4.15) can determine the first bit when $\Delta\Phi_{ni}(t)=\pi/4$ using the sign of $I_{PD}(t)$. Similarly, if the second interferometer can maintain a value of $\Delta\Phi_{ni}(t)$ equal to $-\pi/4$ then the constellation is rotated as seen in Figure 4.12 (c). Using a similar argument to that given above, equation (4.15) will be positive if the second bit is 1, and negative if the second bit is a zero, allowing $I_{PD}(t)$ to determine the second bit using the sign of its output. Hence, by using two interferometers it is possible to decode DQPSK. Note that DQPSK needs to be differentially encoded at the transmitter by adding the phase of the next data symbol to the previously transmitted symbol.

If the situation from Figure 4.12 (b) is considered, an error in the value of T_{int}, which results in $\Delta\Phi_{ni}(t)$ having an absolute value between $\pi/4$ and $3\pi/4$, will result in the decoding scheme having 50% errors as half the symbols with positive real values are ones and half are zeros, with a similar situation for the symbols with negative real values. If the absolute value of $\Delta\Phi_{ni}(t)$ exceeds $3\pi/4$ then all errors will occur. A similar situation will occur for Figure 4.12 (c).

Similar to the coherent receiver measurements of the switching laser, the instantaneous frequency of the switching laser, $\omega_{int}(t)$, is written as:

$$\omega_{int}(t) = \omega_{SG\text{-}DBR\_chirp}(t) + \omega_{SG\text{-}DR\_const} \tag{4.16}$$

where $\omega_{SG\text{-}DBR\_chirp}(t)$ represents the frequency chirp, with $(\omega_{SG\text{-}DBR\_chirp}(t)/2\pi) \in$ [-5GHz,5GHz] and $\omega_{SG\text{-}DBR\_const}$ is the constant frequency which will be in a range similar to the C-band, with $(\omega_{SG\text{-}DBR\_const}/2\pi) \in$ [191.6 THz, 195.9 THz]. Substituting equation (4.16) into equation (4.14) and simplifying yields:

$$\begin{aligned}\Delta\Phi_{ni}(t) = &\left(\omega_{SG\text{-}DBR\_chirp}(t) - \omega_{SG\text{-}DBR\_chirp}(t - T_{int})\right).t + T\omega_{SG\text{-}DBR\_chirp}(t - T_{int}) \\ &+ T_{int}\,\omega_{SG\text{-}DBR\_const} + \Phi_n(t) - \Phi_n(t - T_{int})\end{aligned} \tag{4.17}$$

Rewriting equation (4.8) here (and denoting it as equation (4.18)) so that it can be compared more easily with equation (4.17):

$$\begin{aligned}&\Delta\Phi_{coh}(t) = \left(\omega_{SG-DBR\_chirp}(t) - \omega_{SG-DBR\_chirp}(t - T_{int})\right).t \\ &+ T_{int}\omega_{SG-DBR\_chirp}(t - T_{int}) + \left(\omega_{SG-DBR\_const} - \omega_{ECL}\right)T_{int} \\ &+ \Phi_n(t) - \Phi_n(t - T_{int})\end{aligned} \tag{4.18}$$

The focus is to use the differential phase from the coherent receiver, $\Delta\Phi_{coh}(t)$, which can be measured, to characterise the differential phase term in the delay interferometer, $\Delta\Phi_{ni}(t)$. If the time delay, T_{int}, in equation (4.18) is varied on the order of femtoseconds this will have a negligible effect on the differential phase measured by the coherent receiver, $\Delta\Phi_{coh}(t)$, for the following reasons: firstly, the SG-DBR frequency transient, $\omega_{SG\text{-}DBR\_chirp}(t)$, and the instantaneous phase noise,

$\Phi_n(t)$, have negligible variation over femtosecond timescales. Secondly, the SG-DBR frequency transient, $\omega_{SG\text{-}DBR\_chirp}(t)$, and the coherent receiver's beat signal, $(\omega_{SG\text{-}DBR\_const} - \omega_{ECL})$, will both be less than 10GHz so changing the time delay, T_{int}, over femtosecond timescales will have almost no effect on the constant differential phase, $(\omega_{SG\text{-}DBR\_const} - \omega_{ECL})T_{int}$, and on the differential phase trajectory due to frequency chirp, $T_{int}\omega_{SG\text{-}DBR\_chirp}(t-T_{int})$. Similar arguments for equation (4.17) can be made for all of its terms except the constant differential phase from the carrier frequency, $T_{int}\omega_{SG\text{-}DBR\_const}$, which will vary greatly when varied on the scale of femtoseconds. This is the case because the carrier frequency, $\omega_{SG\text{-}DBR\_const}/(2\pi)$, is in the C-band having frequencies between 191.6 THz and 195.9 THz. These variations will result in an arbitrary constant phase offset in differential phase term in the interferometer, $\Delta\Phi_{ni}(t)$, which can be changed in order to optimally decode I or Q data. The constant differential phase from the carrier frequency in equation (4.17) can be matched in equation (4.18) by changing the value of coherent receiver LO carrier frequency, ω_{ECL}, which will alter the value of the constant differential phase from the coherent receiver, $(\omega_{SG\text{-}DBR\_const} - \omega_{ECL})T_{int}$. This can be fine-tuned using DSP as described in the section concerning CCDFs of the absolute corrected differential phase. By optimising the value of the LO carrier frequency, ω_{ECL}, the differential phase impairments measured using the coherent receiver (equation (4.18)) can fully characterise the differential phase impairments in equation (4.17) since all other terms match. Hence, the coherent receiver measurements can be used to fully predict the time-resolved BER of DQPSK using delay interferometers at the receiver in switching scenarios, considering only phase impairments.

4.3 Comparing 3D-CCDF Calculated Time-Resolved BERs with Directly Counted Time-Resolved BER Measurements

By using the time-resolved BER measurement system that was described in [10] and applied to DQPSK in [8] it was possible to compare the directly measured time-resolved BER with the expected time-resolved BER calculated using the time-resolved CCDF curves. The measured time-resolved BERs were determined from a single delay interferometer using one photodiode, to decode either I or Q data at a given moment in time, with the system being described in detail in [8]. As stated in section 4.2.4.1, the value of ω_{ECL} needs to be optimised in order for the differential phase impairments to match those seen by the delay interferometer. Since the delay interferometer would be most likely be optimised so that the errors near the end of the burst would be minimised (where the laser begins to settle), the value of ω_{ECL} was be varied using DSP, as discussed in section 4.2.4, so that the value of $\Delta\Phi_{coh\text{-}cor}(t)$ is close to zero near the end of the switch. Then applying equation (4.9) to the time-resolved CCDF of $|\Delta\Phi_{coh\text{-}cor}(t)|$ shown in Figure 4.10, the red curve in Figure 4.11 is generated. Note that Figure 4.10 and Figure 4.11 have been copied here for convenience at Figure 4.13 and Figure 4.14, respectively. The blue dots in Figure 4.14 show the time-resolved BER measured by using the FPGA to do direct error counting [8].

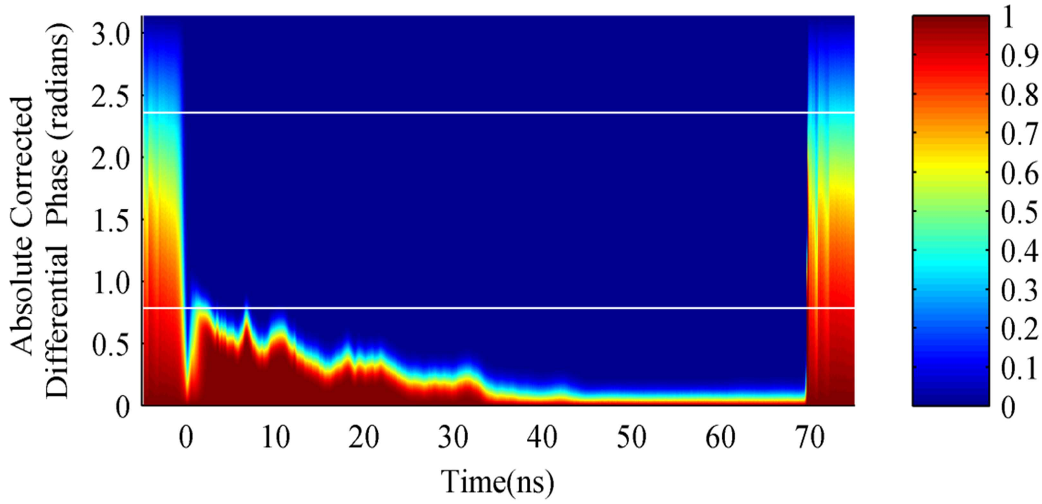

Figure 4.13: Copy of Figure 4.10.

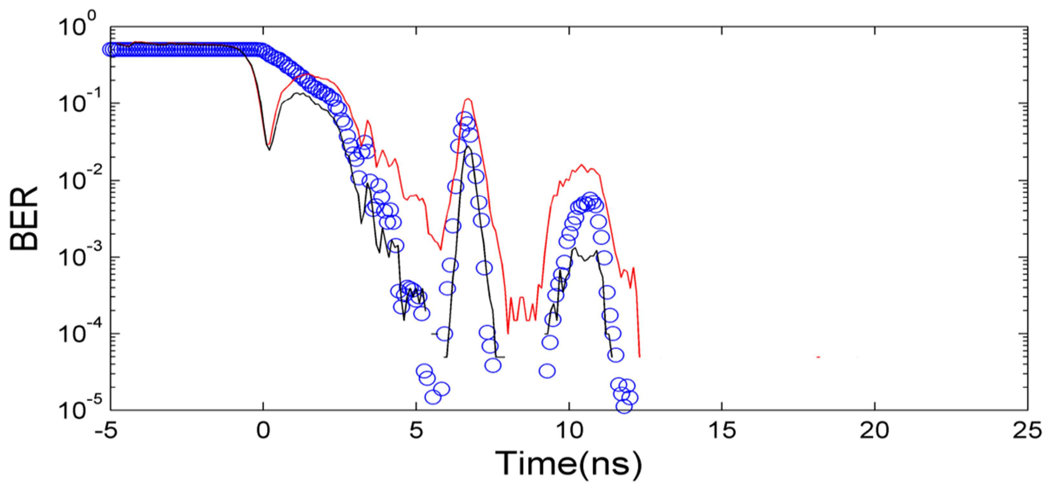

Figure 4.14: Copy of Figure 4.11.

It can be seen that the blue circles and red lines have similar trends but are not exactly matched. This could be explained by the delay in the interferometer not being exactly optimised for the frequency at the end of the switch and this would result in a slight constant phase offset as explained in section 4.2.4.1. This slight constant phase offset could be fitted by slightly varying the frequency offset removed in the DSP in the CCDF calculations. If the frequency offset removed from the instantaneous phase trajectories is varied slightly from the one near the end of the switch so as to optimise the fit between the CCDF time-resolved BER and the FPGA time-resolved BER, it can be seen that this results in remarkably close matching as seen in Figure 4.14 where the optimised CCDF time-resolved BER (black line) matches the FPGA time-resolved BER (blue circles) except for two points at 0ns and at 10.5ns. Hence, this is verification of the 3-D CCDF of the differential phase characterisation technique since the matching between expected and measured time-resolved BERs is excellent. The difference at 0ns may be due to the fact that amplitude noise effects are not taken into consideration and these may have an additional impact on the interferometer receiver. Observing equation (4.15), if $A(t)$ is greatly reduced then some noise effects in the receiver, such as thermal noise, may become more significant. As can be seen from Figure 4.15, the magnitude is low at the start of the switch compared with its value at the end of the switch and it is during this low magnitude part that the frequency offset passes through the 0GHz frequency offset twice.

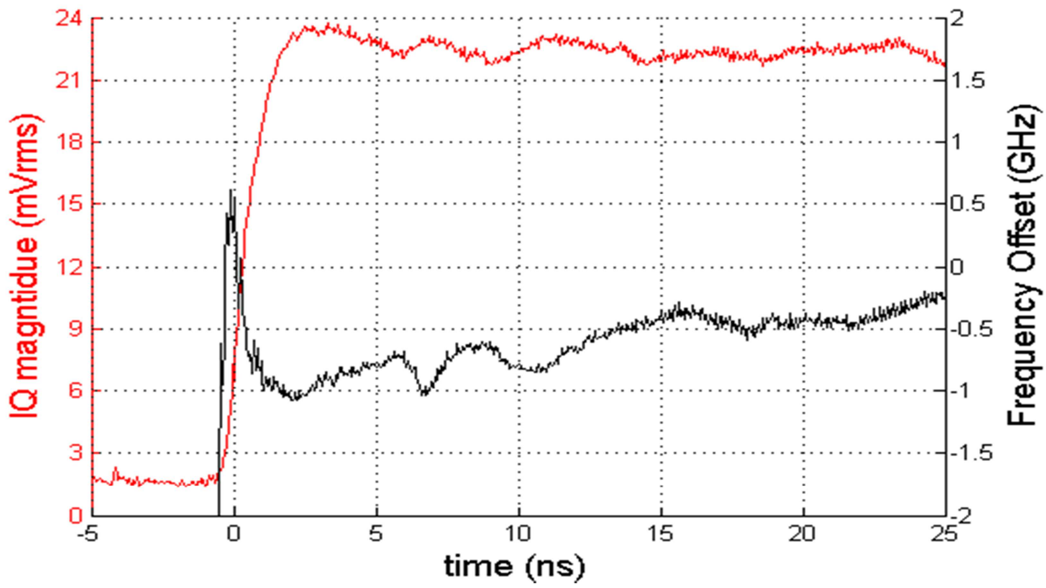

Figure 4.15: Plot showing frequency offset transient versus time (black) and the magnitude of the constellation versus time in rms millivolts (red), showing low magnitude at the start of the switch.

The CCDF would calculate points where the frequency offset is near 0GHz to be points of low BER. However, these 0GHz frequency offset points have low amplitude and, hence, higher BER in the case of a delay interferometer receiver. Nevertheless, it can be seen that the match for all other parts (except for 0ns and at 10.5ns) is very close. It should be noted that the CCDF curve relates to a 100ps symbol period while the FPGA curve relates to a 93ps symbol period. It was found that resampling the sampled waveforms made a negligible difference to improving the accuracy of the calculated time-resolved BERs. This shows that the time-resolved CCDF of the differential phase is able to characterise the phase dynamics well enough to accurately calculate the performance of DQPSK using delay interferometers at the receiver in a switching scenario.

The time-resolved BER of the other wavelength (at 1560nm) can be seen in Figure 4.16. It can be seen that the CCDF calculated time-resolved BER with optimised frequency offset removal (black line) matches extremely well to the FPGA measured time-resolved BER (blue circles), except for the part of the switch at 30ns. This is further verification of the 3-D CCDF of the differential phase characterisation approach since it produces remarkably accurate expected results.

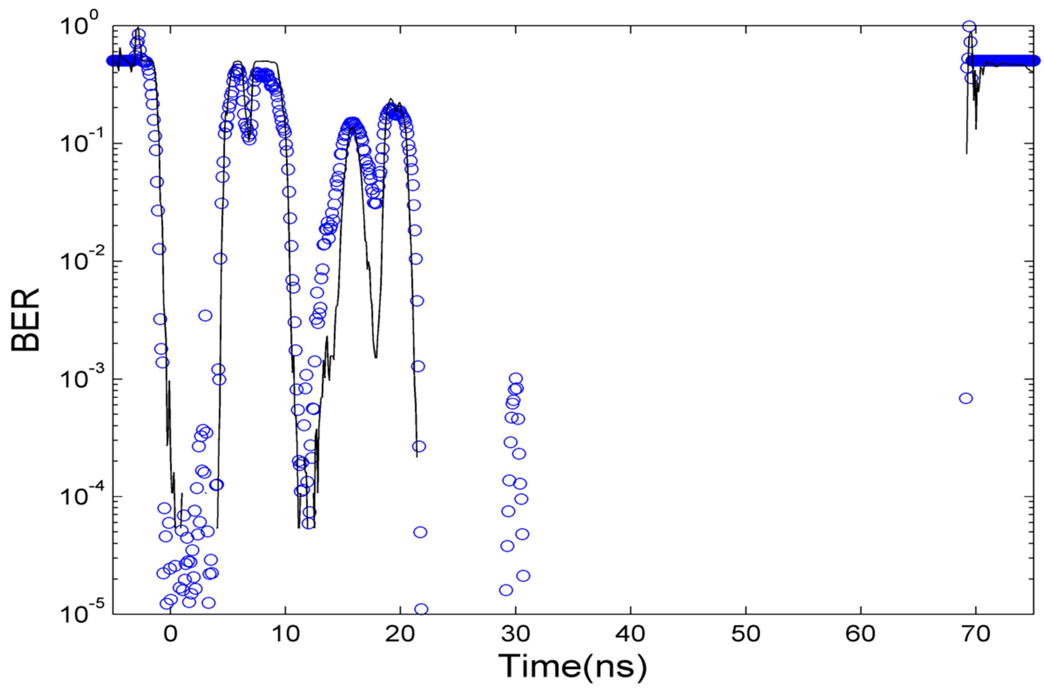

Figure 4.16: Plot of the FPGA measured time-resolved BER (blue circles) and the optimised CCDF calculated time-resolved BER (black line) for the part of switch at the 1560nm wavelength.

Note that the minimum BER observable by the CCDF time-resolved BER is approximately $5*10^{-5}$ since approximately 10^{4} switches were used allowing for probabilities as low as 10^{-4} to be calculated, and BERs calculated in equation (4.9) can have half these probabilities. This means that the BERs at 30ns should be within the resolution of the CCDF time-resolved BER. A possible explanation for this discrepancy at 30ns is that the coherent receiver can only measure frequency offsets within ±10GHz from the ECL centre frequency and any spurious modes that appear during a switching event which exist outside this range will not be observed. By contrast, it is possible for the interferometer to be affected by another spurious mode if the delay set by the interferometer allows for sufficient constructive interference and the power in the other spurious mode is sufficiently high. This would result in higher BERs for the interferometer case than the coherent receiver case. It was also anticipated from the analysis in [11] that changes in the wavelength of the largest side mode are possible after a switching event which is consistent with the theory given here.

4.4 Time-Resolved Linewidth

If Wiener phase noise statistics are assumed, it is possible to determine a time-resolved linewidth plot. By calculating the variance of the differential phases within a given time slot by using multiple switches and then applying equation (4.1) it is possible to determine the linewidth in a given time slot. A very similar time-resolved linewidth method was described in [12] which used a delayed self-homodyne system instead of the heterodyne system was used here. Shown in Figure 4.17 are multiple time-resolved linewidths where the figure legend indicates which time-resolved linewidth curves relate to which part of the wavelength switch.

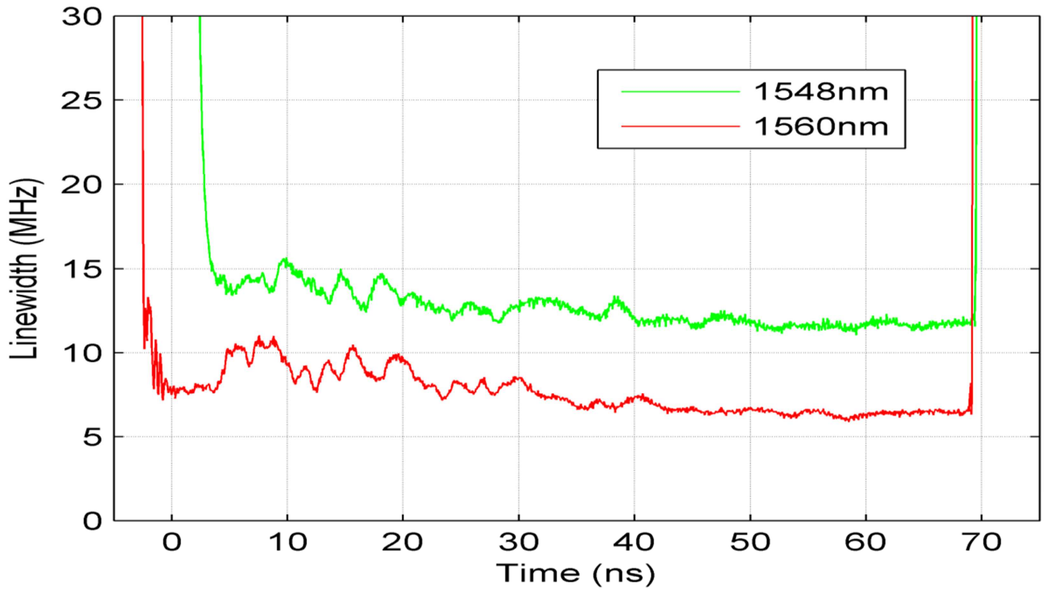

Figure 4.17: Time-resolved linewidths for the switching SG-DBR laser, with the green curve corresponding to the 1548nm wavelength (Figure 4.14) and the red curve corresponding to the 1560nm wavelength (Figure 4.16).

However, it is not sufficient to just know the time-resolved linewidth to predict performance as the frequency chirp reduced the BER tolerances of the absolute differential phase and made the effect of phase noise more pronounced. This can be deduced by looking at equation (4.9). Considering Figure 4.14, Figure 4.15 and the green curve in Figure 4.17 together, the error peaks in Figure 4.14 occurred at 1.3ns, 6.7ns and at 10.5ns. It can be seen that the linewidth from the green curve in Figure 4.17 did not vary greatly over the burst period. However, there were peaks in the frequency offset near 6.7ns and 10.5ns in Figure 4.15 (the area near 1.3ns is not suitable for this analysis since it was affected by low amplitude as well as quick varying frequency offsets). This shows that the frequency chirp brought the average absolute differential phase closer to the $\pi/4$ tolerance line where the phase noise will have a greater impact. Hence, frequency chirp and phase noise both need to be considered for accurate predictions of time-resolved BERs. This can be done in a consistent manner by using CCDFs of differential phase or CCDFs of absolute corrected differential phase. Note that the time-resolved linewidth work in [12] and the CCDF work in [3] were published contemporaneously.

4.5 Physical Interpretation of Switching Characteristics

There are a number of factors which influence the switching characteristics of the SG-DBR in the system shown here. Firstly, the switching signal applied to the laser will affect the switching performance, where it was demonstrated in [13] that appropriately controlling the switching signal(s) the frequency chirp and phase noise characteristics can be made to settle much quicker resulting in shorter waiting times for optical packet decoding. The excitation of different modes when the laser switches from one wavelength to another is also a factor as discussed in [11]. In addition, thermal changes caused by electrical power dissipation from switching electrical inputs can have an effect on wavelength accuracy [14].

4.6 Summary

It has been shown in this chapter that static linewidth measurements which use coherent receivers need to use sampling intervals that do not overlap in order to ensure statistical independence so that the variance is calculated correctly. A novel method of simultaneously characterising both the phase noise and the frequency chirp of a switching tuneable laser was described and experimentally demonstrated. This method overcomes previous limitations such as assuming a Wiener phase noise model and separating frequency chirp and phase noise allowing for a single combined characterisation scheme to be used. Frequency chirp can be subsequently interpreted as the mean values from the time-resolved distributions, and phase noise can be considered as the spread or width of the distribution about the mean. The validity and accuracy of this method of characterisation was tested by correctly calculating, using CCDFs, expected time-resolved BERs of DQPSK after a switching event and showing that these matched time-resolved BERs experimentally measured using an FPGA. Discrepancies are attributed to: (i) low optical power affecting the FPGA-measured BERs at the start of a switch, (ii) other spurious modes that appear during a wavelength switch outside the bandwidth of the scope affecting the FPGA-measured BERs, and (iii) limitations relating to the lowest possible non-zero BER determinable by the CCDF calculated BERs. It was also shown that time-resolved linewidth measurements could also be determined from this setup using a similar approach to [12]. However, it was also shown that time-resolved frequency chirp is also required for accurate time-resolved BER calculations. Having characterised the phase dynamics of a switching tuneable laser (which are impairments to a coherent optical packet /burst system), which were seen to have significant frequency chirp and some phase noise variation, the next step is to find methods of compensating the frequency offset after a switching event. The difficulties involved in this are that the frequency offset will be time-varying, potentially large, and will have to be estimated almost immediately once the packet or burst arrives in order for the system to be considered a packet or burst system.

References

1. K. Kikuchi and K. Igarashi, "Characterization of Semiconductor-Laser Phase Noise with Digital Coherent Receivers," in *Optical Fiber Communication Conference and Exposition,* (IEEE, 2011), pp. OML3.

2. E. Kreyszig, *Advanced Engineering Mathematics, Ninth Edition* (John Wiley & Sons, 2006).

3. A. J. Walsh, J. A. O'Dowd, V. M. Bessler, K. Shi, F. Smyth, J. M. Dailey, B. Kelleher, L. P. Barry, and A. D. Ellis, "Characterization of time-resolved laser differential phase using 3D complementary cumulative distribution functions," Optics Letters **37,** 1769-1771 (2012).

4. N. Chernov, "Ellipse Fit (Taubin method)," *Updated (2009),* http://www.mathworks.com/matlabcentral/fileexchange/22683-ellipse-fit--taubin-method-/content/EllipseFitByTaubin.m

5. G. Taubin, "Estimation of Planer Curves, Surfaces, and Nonplanar Space Curves Defined by Implicit Equations with Applications to Edge and Range Image

Segmentation." IEEE Transactions on Pattern Analysis and Machine Intelligence **13,** 1115-1138 (1991).

6. E. W. Weisstein, ""Ellipse." From MathWorld--A Wolfram Web Resource," *Updated (2014),* http://mathworld.wolfram.com/Ellipse.html

7. R. Ramaswami and K. N. Sivarajan, *Optical Networks A Practical Perspective, Second Edition* (Academic Press, 2002).

8. J. A. O'Dowd, K. Shi, A. J. Walsh, V. M. Bessler, F. Smyth, T. N. Huynh, L. P. Barry, and A. D. Ellis, "Time Resolved Bit Error Rate Analysis of a Fast Switching Tunable Laser for Use in Optically Switched Networks," Journal of Optical Communications and Networking **4,** A77-A81 (2012).

9. F. Smyth, C. Browning, K. Shi, F. Peters, B. Corbett, B. Roycroft, and L. P. Barry, "10.7Gbd DQPSK packet transmission using a widely tunable slotted Fabry-Pérot laser," in *European Conference and Exhibition on Optical Communication,* (IEEE, 2010), pp. Mo.1.F.5.

10. J. A. O'Dowd, V. M. Bessler, S. K. Ibrahim, A. J. Walsh, F. H. Peters, B. Corbett, B. Roycroft, P. O'Brien, and A. D. Ellis, "Implementation of a High Speed Time Resolved Error Detector Utilising a High Speed FPGA," in *International Conference on Transparent Optical Networks,* (IEEE, 2011), pp. We.D1.2.

11. K. Shi, Y. Yu, R. Zhang, W. Liu, and L. P. Barry, "Static and dynamic analysis of side-mode suppression of widely tunable sampled grating DBR (SG-DBR) lasers," Optics Communications **282,** 81-87 (2009).

12. K. Shi, R. Watts, D. Reid, T. N. Huynh, C. Browning, P. M. Anandarajah, F. Smyth, and L. P. Barry, "Dynamic Linewidth Measurement Method via an Optical Quadrature Front End," IEEE Photonics Technology Letters **23,** 1591-1593 (2011).

13. J. E. Simsarian, J. Gripp, S. Chandrasekhar, and P. Mitchell, "Fast-Tuning Coherent Burst-Mode Receiver for Metropolitan Networks," IEEE Photonics Technology Letters **26,** 813-816 (2014).

14. J. E. Simsarian, M. C. Larson, H. E. Garrett, H. Xu, and T. A. Strand, "Less Than 5-ns Wavelength Switching With an SG-DBR Laser," IEEE Photonics Technology Letters **18,** 565-567 (2006).

Chapter 5

Doubly Differential Phase Shift Keying for High Frequency Offset Tolerance

In this chapter, the key concern will be on removing/ compensating for the effect of the frequency offset between the transmitter laser and the LO laser at the polarisation-diverse coherent receiver. Conventional techniques require either that the frequency offset is kept within certain limits or that training symbols are sent so that, effectively, the frequency offset can be measured and, thereafter, tracked (training symbol techniques may vary but a simple implementation is to just measure the frequency offset with no modulation and to then track small deviations). While these techniques can be implemented in static scenarios such as OCS where long start-up times to set up channels could possibly be used, they will not be suitable in situations where the frequency offset varies greatly or when decoding needs to occur soon after the data is received, such as in coherent optical packet/ burst switched scenarios. One technique which overcomes these difficulties is DDPSK. However, the typical DDPSK implementation has a large SNR penalty associated with it. Although techniques to reduce this SNR penalty have been published (which are discussed at the end of section 5.2), it will be shown that the novel M^{th} power DDPSK (which is a novel system and is a novel contribution of the research published in this thesis) can achieve very similar BER versus OSNR performance compared with M^{th} power single differential phase shift keying (SDPSK). It will be shown from a theoretical point of view that M^{th} power doubly differential quadrature phase shift keying (DDQPSK) represents an improvement in the BER versus SNR performance of DDQPSK compared with prior art. Additional advantages of M^{th} power DDPSK are that it can be implemented with only very modest additions to M^{th} power SDPSK and it is a feed-forward method. BER versus OSNR results with static and switching frequency offsets using simulation and experimental data will demonstrate that M^{th} power DDPSK has a very large frequency offset range, can achieve very short waiting times after a switching event, and provides a very robust demodulation system for coherent optical packet/ burst switched networks using M-ary PSK constellations.

5.1 Frequency Offset Compensation Schemes

The need for frequency offset compensation has already been established in this thesis. In the case of coherent optical packet/ burst switched networks, one key aspect which needs to be focused on is the range of the frequency offset compensation algorithm. The frequency offset is expected to be time-varying and potentially large in coherent optical packet/ burst switched networks, which means that without a large compensation range decoding coherent data will almost certainly result in large errors or require large waiting times. With regard to range, it was explained previously in section 3.2.3 of this thesis that for M-ary PSK systems where the signals have been downsampled to one sample per symbol there is an inherent limit to the maximum frequency offset which can be estimated and/or removed, and this is given as $\Delta\omega=\pm\pi/(MT)$ (or $\nu=1/(2MT)$). Note that if a frequency offset equal to the symbol rate, i.e. $\Delta\omega=(2\pi/T)$, is added to the original frequency offset, ω, then for one sample per symbol systems, the frequency offset compensation scheme will still work as the corresponding rotation of the constellation will be an additional 2π from symbol to symbol. However, such circumstances may not be common in practice as frequency offsets that are high may cause the data to be filtered out by the limited electronic bandwidth of the receiver. It is possible to extend the $(\pm\pi/(MT))$ range by using training symbols (known symbols) in order to determine the initial frequency offset and to track small deviations thereafter as described in [1]. Note that [1] also makes reference to using feedback from FEC but it is not clear how this system is intended to work. There are a number of frequency offset correction techniques which use the fast-Fourier transform (FFT) but may have limited ranges if exponential operations are used to remove data, for example for QPSK formats the range is the $(\pi^*R_s/4)$ if the signal is raised to the power of 4 to removed data before calculating the FFT, where R_s is the symbol rate [2].

Other publications which use spectrum based methods to estimate/compensate frequency offsets such as [3, 4] and another paper which uses a system based on a timing recovery algorithm [5] claim to have frequency offset ranges greater than $\pm\pi/(MT)$ (or equivalently $\pm(\pi^*R_s)/(MT)$), however, it is not clearly stated what the requirements of these methods are in terms of the minimum number of samples per symbol required. These publications either state that they used two samples per symbol or did not state the number of samples per symbol used. As was explained previously in chapter 3, data which contains a high frequency offset equal to $2\pi/(MT)$ which is sampled at one sample per symbol cannot overcome this ambiguity. In addition, these three papers seem to adopt a common approach of performing a coarse estimation to remove frequency offset ambiguity and then use an M^{th} power method for precise frequency offset estimation, which means additional computational complexity if only the M^{th} power frequency offset estimation algorithm was originally used. For the proposed frequency offset estimation scheme which will be given later in this chapter, M^{th} power DDQPSK, only modest additions to the DSP of M^{th} power frequency offset estimation and M^{th} power phase estimation are required.

5.2 Doubly Differential Concept

As was seen for the M^{th} power frequency offset estimation scheme for M-ary PSK data [6], there is a limited range of frequency offsets which can be tolerated, which are inside the range $(-\pi/(MT), \pi/(MT))$, or alternatively written as $(-(\pi * R_s)/M, (\pi * R_s)/M)$ [7]. This is problematic in a coherent system as the frequency difference between transmitter laser and the LO needs to be within this tolerance, e.g. for 10GBaud QPSK the frequency offset must be less than 1.25GHz if the frequency offset is to be compensated by the M^{th} power frequency offset compensation method. From the previous chapter, it is clear that a large frequency offset range is essential in a coherent optical packet/ burst switched network. One way to allow for large frequency offsets to exist between the transmitter and LO is to employ DDPSK [8]. One of the earliest mentions of DDPSK in the literature is given in [9] where the application of interest is dealing with Doppler Effect induced frequency shifts in air-to-air and air-to-ground coherent communications. A block diagram of the encoding and decoding stages for DDPSK is shown in Figure 5.1 (a) and Figure 5.1 (b) respectively.

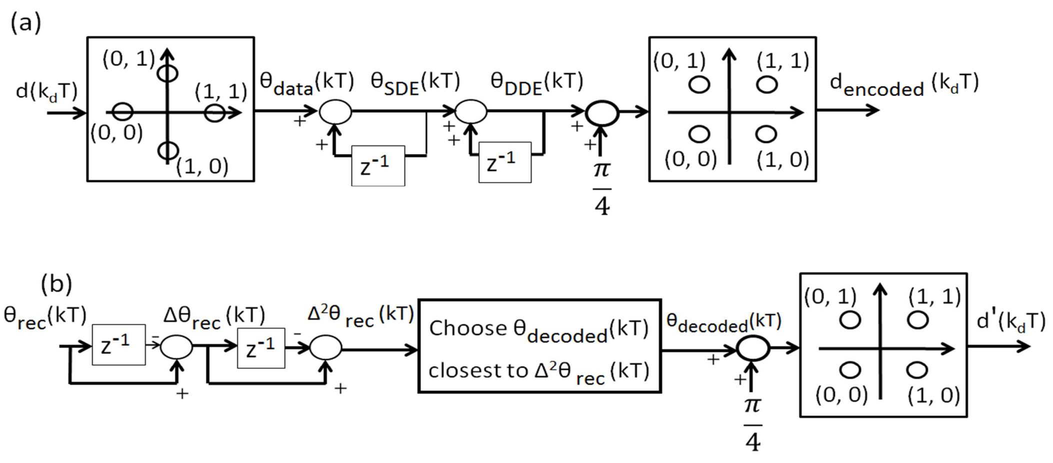

Figure 5.1: Operations showing (a) doubly differential encoding and (b) doubly differential decoding [8, 10].

At the transmitter, the data to be transmitted, $d(k_dT)$, where k_d is the sample index for data bits, is first converted from a bit stream to phases using Gray coding to give the phase term, $\theta_{data}(kT)$, where k is the sample index for symbols. The resulting phase terms are then passed through two single differential encoding stages, with $\theta_{SDE}(kT)$ being the equivalent to the single differentially encoding phase and $\theta_{DDE}(kT)$ being the doubly differentially encoding phase, as seen in Figure 5.1. The encoding equation is given as [8, 10]:

$$\begin{aligned}\theta_{DDE}(kT) = \mathrm{mod}(\,&\theta_{data}(kT) + 2\theta_{DDE}((k-1)T) \\ &- \theta_{DDE}((k-2)T), 2)\end{aligned} \tag{5.1}$$

where $k \geq 3$. After adding a $\pi/4$ term to $\theta_{DDE}(kT)$, Gray coding converts the phase to a data stream, $d_{encoded}(k_dT)$, which is the bit stream to be transmitted, presumably using an IQ modulator or a phase modulator.

In Figure 5.1 (b), the input to the decoder is the phase received from a coherent receiver, $\theta_{rec}(kT)$, which is downsampled to one sample per symbol, for example, by using the downsampling algorithm proposed in chapter 3 based on using the sampling phase with the highest average magnitude. $\theta_{rec}(kT)$ is passed through differential phase stages, with $\Delta^2\theta_{rec}(kT)$ being the doubly differentially decoded phase. Then, the element of [0, $\pi/2$, π, $3\pi/2$] which is closest to $\Delta^2\theta_{rec}(kT)$ is selected, with the selected phase being $\theta_{decoded}(kT)$. After adding a $\pi/4$ phase shift to $\theta_{decoded}(kT)$ the phase is converted to data bits using Gray encoding, with $d'(k_dT)$ being the decoded phase.

The frequency offset tolerance of DDPSK can be illustrated as follows, using a similar argument as in [10]. Assuming that $\theta_{rec}(kT)$ is of the form:

$$\theta_{rec}(kT) = \theta_{data}(kT) + \Delta\omega_{rec} T k_1 + \theta_0 \tag{5.2}$$

where $\Delta\omega_{rec}$ is the frequency offset, T is the symbol period, and θ_0 is the initial phase. Phase noise and additive white Gaussian noise will not be considered for the moment. Hence, $\Delta^2\theta_{rec}(kT)$ can be calculated as:

$$\Delta\theta^2{}_{rec}(kT) = \Delta\theta_{rec}(kT) - \Delta\theta_{rec}((k-1)T) \tag{5.3}$$

where,

$$\Delta\theta_{rec}(kT) = \theta_{rec}(kT) - \theta_{rec}((k-1)T) \tag{5.4}$$

Substituting equation (5.4) into equation (5.3), yields:

$$\Delta\theta^2{}_{rec}(kT) = \left(\theta_{rec}(kT) - \theta_{rec}((k-1)T)\right) - \left(\theta_{rec}((k-1)T) - \theta_{rec}((k-1)T)\right) \tag{5.5}$$

$$\Delta\theta^2{}_{rec}(kT) = \theta_{rec}(kT) - 2\theta_{rec}((k-1)T) + \theta_{rec}((k-2)T) \tag{5.6}$$

Substituting equation (5.2) into equation (5.6) yields:

$$\begin{aligned}\Delta\theta^2{}_{rec}(kT) = &\left(\theta_{data}(kT) + \Delta\omega_{rec}Tk + \theta_0\right) \\ &- 2\left(\theta_{data}((k-1)T) + \Delta\omega_{rec}T(k-1) + \theta_0\right) \\ &+ \left(\theta_{data}((k-2)T) + \Delta\omega_{rec}T(k-2) + \theta_0\right)\end{aligned} \tag{5.7}$$

which can be simplified to:

$$\Delta\theta^2{}_{rec}(kT) = \theta_{data}(kT) - 2\theta_{data}((k-1)T) + \theta_{data}((k-2)T) \tag{5.8}$$

Hence, it can be seen from equation (5.8) that the doubly differentially decoded phase, $\Delta^2\theta_{rec}(kT)$, depends only on $\theta_{data}(kT)$ values and is independent of the frequency offset and initial phase. Therefore, DDPSK can tolerate frequency offsets up to the limits of the electronic bandwidth of the receiver in the presence of no phase noise or additive white Gaussian noise. Note that for larger symbol rates the frequency offset range will be reduced. This occurs since the edge of the spectrum will be filtered out by the limited electronic bandwidth of the receiver at smaller frequency offsets since the spectrum width increases with larger symbol rates. Note that the DDPSK decoding scheme described up to this point and depicted in Figure 5.1 (b) is referred to here as “Simple DDPSK”. The term “Simple SDPSK” is used here also and is similar to Simple DDPSK except only single differential encoding and differential decoding stages are used. The terms Simple DDPSK and Simple SDPSK are only used in this thesis and in papers co-authored by the author of this thesis to more easily distinguish them from other decoding methods which use additional DSP.

However, for the zero frequency offset case, a 4.77dB penalty is expected when using Simple DDPSK instead of Simple SDPSK. In [11], it is pointed out that the impulse response given in equation (5.8) will result in a multiplication of the input noise variance by a factor of 6 (since the variances from the different terms will add as ($\sigma^2 + 4\sigma^2 + \sigma^2 = 6\sigma^2$)) and this will be 3 times the value for the SDPSK case (which will be ($\sigma^2 + \sigma^2 = 2\sigma^2$)). This factor of three will result in a $10 \cdot \mathrm{Log}_{10}(3) = 4.77$dB penalty when using DDPSK instead of SDPSK. Note also that the 4.77dB penalty is compared with SDPSK without any phase estimation algorithm applied which means that an even larger penalty will be seen when comparing M^{th} power SDPSK (SDPSK using M^{th} power frequency offset compensation and M^{th} power phase estimation) and Simple DDPSK.

There are methods which attempt to reduce the power penalty associated with Simple DDPSK. It shown in [11] that a slightly varied doubly differential format (referred to as non-adjacent double differential phase shift keying [12]) which finds the doubly differential phase over 4 symbols instead of 3 as shown in equation (40) gives only a multiplication of the variance by a factor 4 leading to a 3.01dB penalty (from: $10*\mathrm{Log}_{10}(4)$ - $10*\mathrm{Log}_{10}(2)$) compared with SDPSK without phase estimation. Another method is described [13] where essentially the second differential stage is replaced by an M^{th} power phase estimation stage which allows for one of the differential stages to be performed after the hard decision which will reduce the SNR penalty. In [14], a similar approach of using only one simple differential phase operation before the hard decision is used except that the second differential stage and hard decision are replaced by a multi-symbol decision directed stage which feeds back decisions in order to improve the second differential stage so it can have negligible penalty. However, the method in [14] has a BER performance approximately equivalent to performing simple single differential quadrature phase shift keying (SDQPSK) without phase estimation and performing the differential decoding before the hard decision, and the method in [13] will have approximately twice the BER of [14]. Also, [14] uses a feedback mechanism which is less suitable than a feed-forward method for an optical packet/ burst switched network since an error in a feedback system can result in continuous propagation of errors, while a feed-forward system is guaranteed to eventually forget any large disturbances. It can be seen that the ideal method for using DDPSK in a coherent optical packet/ burst switched network should be feed-forward and should also try to eliminate or reduce any penalty associated with simple differential phase stages before the hard decision. Unlike the methods in [13, 14] whose BER versus SNR performance will be greater than that of Simple SDPSK, the novel method, M^{th} power DDPSK, will be shown to have a BER twice that of M^{th} power SDPSK. It will be shown later how M^{th} power DDQPSK will give superior performance to Simple SDQPSK.

5.3 M^{th} Power DDPSK

It is instructive to first consider the M^{th} power SDPSK algorithm and the deficiencies associated with it before introducing the M^{th} power DDPSK algorithm.

The frequency offset, ω, at the input of the M^{th} power SDPSK algorithm is expressed as follows:

$$\omega = 2\pi\left(N_f /\left(MT\right) + \delta_f\right) \tag{5.9}$$

where N_f is an integer, and δ_f is in the range $|\delta_f| < 1/(2MT)$. The frequency offset component ($2\pi{*}N_f/(MT)$) will not be seen by the M^{th} power frequency offset compensation scheme since it is indistinguishable from data and any M^{th} power operation will remove this frequency offset, i.e. raising the field to the power of M will essentially multiply ω by M giving:

$$\omega M = \left(2\pi N_f / T + 2\pi M\delta_f\right) \tag{5.10}$$

The phase shift due to frequency offset after the M^{th} power operation over one symbol period will be given by ωMT:

$$\omega MT = \left(2\pi N_f + 2\pi M\delta_f T\right) \tag{5.11}$$

It can be seen in equation (5.11) that only the $2\pi M\delta_f T$ term can be observed and that the $2\pi{*}N_f$ term will not be observed due to phase wrapping. Hence, there will be an ambiguity in the frequency offset as a result of the ($2\pi N_f/(MT)$) term. However, the $2\pi\delta_f$ component will still be removed since it is in the M^{th} power frequency offset range. Hence, ω could potentially have a frequency offset component of ($2\pi N_f/(MT)$) after the frequency offset compensation stage if N_f is non zero. The M^{th} power phase estimation stage will also not see this frequency offset as it will be indistinguishable from the data. Hence, after the hard decision there is potentially a ($2\pi N_f/(MT)$) frequency offset component still in the hard decision symbols. This is the reason that the M^{th} power frequency offset scheme requires N_f to be equal to zero, so that only the limited $2\pi\delta_f$ term remains. Noting from the analysis in section 5.2 above that doubly differential phase decoding will remove any frequency offset, this will also apply to symbols after the hard decision. Hence, performing a doubly differential operation after the hard decision can remove any residual frequency offset that is a multiple of ($2\pi/(MT)$) and, therefore, can remove any residual ($2\pi N_f/(MT)$) term. Hence, M^{th} power DDPSK can remove any frequency offset within the electronic bandwidth of the receiver, which is the same frequency offset compensation range as Simple DDPSK.

A diagram comparing different demodulation algorithms is given in Figure 5.2. In Figure 5.2 the DSP for (a) M^{th} power SDPSK, as described in chapter 2, (b) Simple DDPSK, as described in section 5.2, and (c) M^{th} power DDPSK is given.

For Mth power SDQPSK the received downsampled constellation has its frequency offset removed and has its phase noise mitigated by a phase estimation stage. The constellation is expected to then resemble an M-ary PSK constellation or in the case of Figure 5.2, a QPSK constellation. Then, a hard decision on the constellation is made. After this, a single differential decoding stage gives the original data. For Figure 5.2 (b), the received downsampled constellation has its phase applied to two differential stages, and then a hard decision is made on the constellation to give the original data. It can be seen from Figure 5.2 (b) that the constellation before the hard decision is quite noisy which is due to the fact that noise terms are being added together twice. Finally, Figure 5.2 (c) shows the algorithm for the novel Mth power DDPSK scheme. All the steps are the same as for Figure 5.2 (a) up to the hard decision. After the hard decision, instead of a single differential decoding stage being applied to the hard decision phase, two differential decoding stages are applied. Note that Mth power SDPSK must have only one differential phase encoding stage performed at the transmitter while Mth power DDPSK must have two differential phase encoding stages performed at the transmitter.

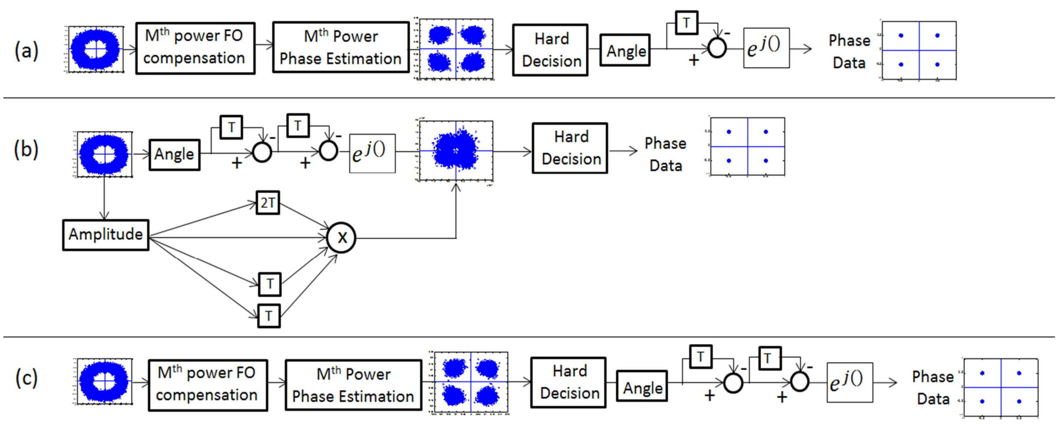

Figure 5.2: DSP for (a) Mth power SDPSK, (b) Simple DDPSK and (c) Mth power DDPSK [15], where the constellation used for illustration purposes is QPSK (similar diagram in [15]).

One key issue with using Simple DDPSK is that it has a 4.77dB SNR penalty compared with the Simple SDPSK. We can greatly reduce the SNR penalty by using the novel "Mth power DDPSK" algorithm. It was explained in [16] that the BER of PSK will double as a result of using differential decoding with Mth power SDPSK. This can be explained as follows; if low BERs and high OSNRs are considered, errors will predominantly be ones where AWGN causes symbols to appear inside the decision boundaries of adjacent symbols and the probability of consecutive errors will be small. When no differential decoding after the hard decision is used, this will result in a single error from AWGN due to Gray coding. Where single differential decoding after the hard decision is used, a single AWGN $2\pi/M$ error will results in single bit errors for the first and second phase terms in the differential phase decoding equation and will result in two errors where previously there was one. This explains the doubling of the BER when going from PSK to M^{th} power SDPSK. For M^{th} power DDPSK with $M \geq 4$, from equation (5.6), which will be applied after the hard decision, a single $2\pi/M$ error will result in a single bit error for the first term, two bit errors for the second term (π/M rotation will result in two bit errors due to Gray coding) and a single bit error for the last term, leading to four times as many errors than if no differential decoding with PSK was used and twice as many errors than if single differential decoding was used. A plot of the theoretical BER versus SNR per bit for QPSK, Simple SDQPSK, M^{th} power SDQPSK and M^{th} power DDQPSK is shown in Figure 5.3 using the appropriate formulae from the end of chapter 3 given in [6, 17] and applying the analysis given above

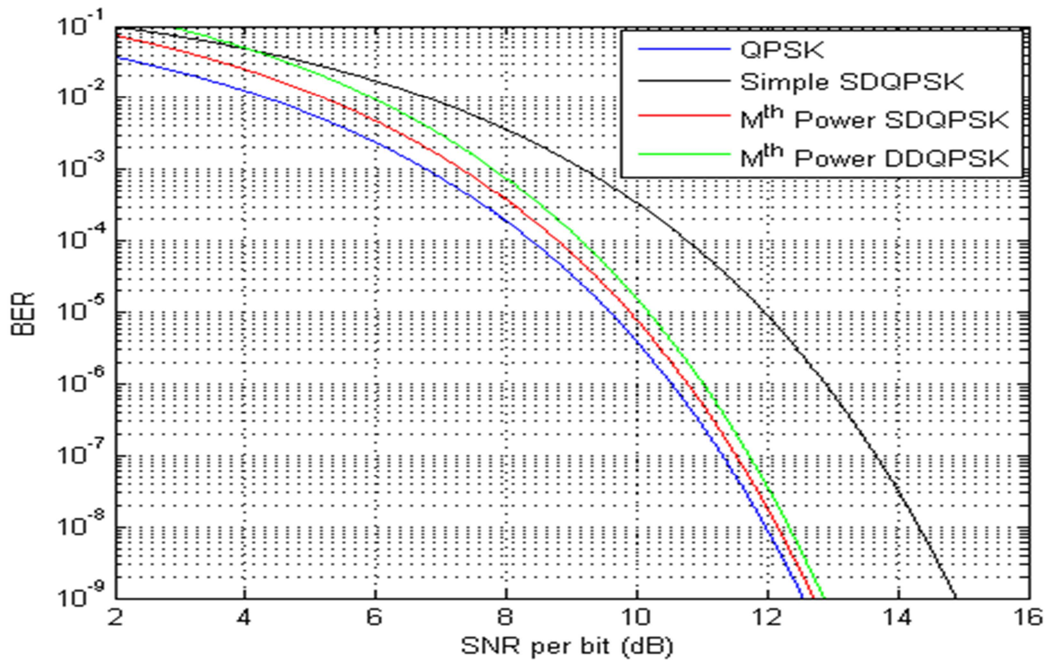

Figure 5.3: Theoretical BER versus SNR per bit for different methods of demodulating QPSK data.

Note that only AWGN is considered here with no frequency offset and no phase noise. QPSK with no differential encoding could be decoded with the aid of training symbols and using some phase estimation technique such as M^{th} power phase estimation. It should be noted that there is a 0.49dB penalty when using M^{th} power DDQPSK instead of M^{th} power SDQPSK at a BER of 10^{-3}, and a 1.03dB penalty when using M^{th} power DDQPSK instead of QPSK at a BER of 10^{-3}. This shows that M^{th} power DDQPSK can be used with only small additional SNR requirements to M^{th} power SDQPSK. Simple SDQPSK has 1.37dB additional SNR requirements than M^{th} power DDQPSK at a BER of 10^{-3}. Simple DDQPSK is expected to have a 4.77dB SNR penalty compared with Simple SDQPSK. Hence, it is clear that M^{th} power DDQPSK makes enormous gains over the original Simple DDQPSK. In addition, M^{th} power DDQPSK will have better BER versus SNR performance than the DDQPSK methods in [13, 14] at a BER of 10^{-3}, since [13, 14] have higher SNR requirements than Simple SDQPSK and Simple SDQPSK has higher SNR requirements than M^{th} power DDQPSK for BERs less than $4.6*10^{-2}$.

5.3.1 Modification to M^{th} Power Frequency Offset Compensation for M^{th} power DDPSK

One additional component of the M^{th} power DDPSK scheme not already discussed is that for improved performance, the M^{th} power frequency offset compensation algorithm will need to be slightly adjusted to account for possible transients where the frequency offset changes causes the value of N_f in equation (5.9) to change. When the value of N_f changes this can lead to errors in the M^{th} power DDPSK algorithm close to where the change occurs since the doubly differential decoding will only remove constant frequency offsets. In order to keep N_f constant, an unwrap function can be applied to the estimated differential phase due to frequency offset. The adjustment to be made to the M^{th} power frequency offset compensation algorithm is shown in Figure 5.4.

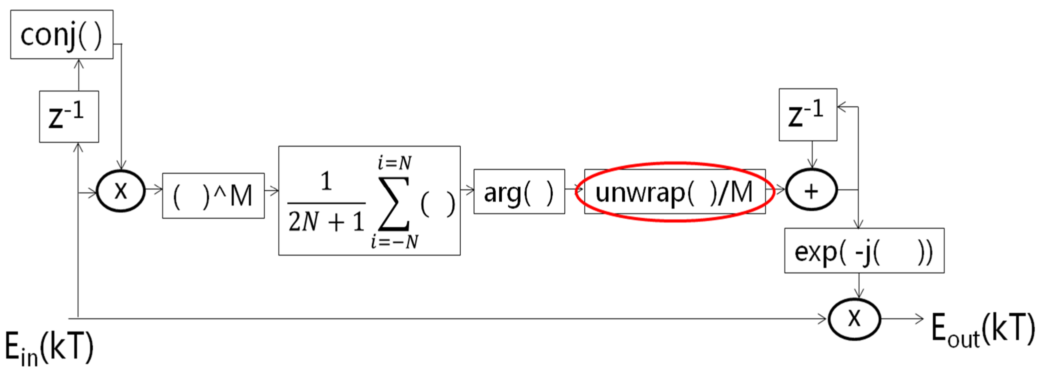

Figure 5.4: M^{th} power frequency offset compensation algorithm with unwrap function included for M^{th} power DDPSK algorithm.

An unwrap function is placed after the argument of the averaged field is determined in order to ensure that a smooth frequency offset trajectory is calculated. A similar idea to using this is suggested in [1] except with training symbols or feed-back from FEC used to determine the initial differential phase due to frequency offset which is added to the estimated differential phase which should then be unwrapped before the accumulator. The measured frequency offset and estimated frequency offset from the M^{th} power frequency offset compensation method are shown in Figure 5.5, where the frequency offset estimation is done without the unwrap function in (a) and with the unwrap function in (b).

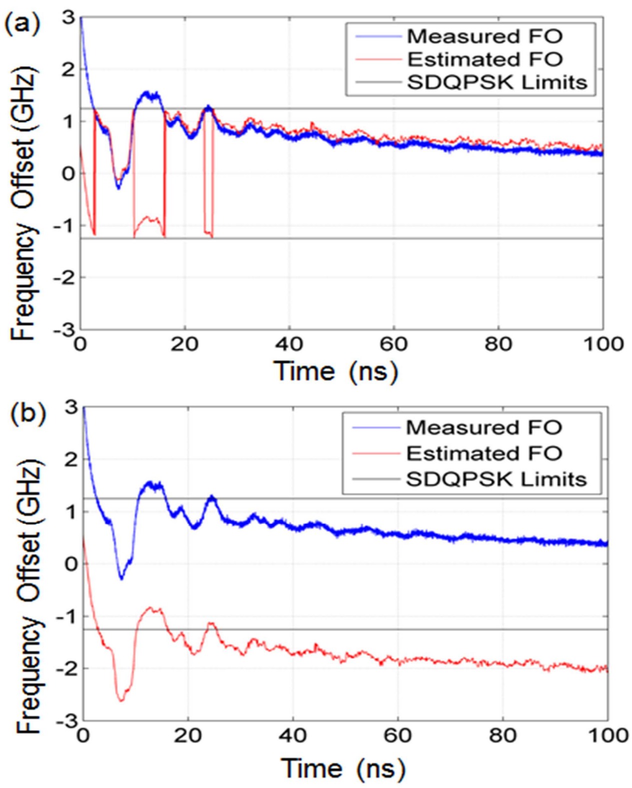

Figure 5.5: Plots of measured frequency offset and estimated frequency offset versus time using M^{th} power frequency offset compensation (a) without unwrapping and (b) with unwrapping. The black lines indicate the frequency offset limitations for M^{th} power SDQPSK.

The measured frequency offset was determined by measuring a number of different beat signals (without modulation being present) using a polarisation-diverse coherent receiver, time-aligning the bursts using the same method discussed in the previous chapter and averaging the frequency offset trajectories. It can be seen in Figure 5.5 (a) that the estimated frequency offset is always within the solid black lines, which represent the $\pm\pi/(MT)$ limits of the M^{th} power frequency offset compensation algorithm for SDQPSK. It is clear that there is not a constant frequency offset difference between the measured and the estimated frequency offsets in Figure 5.5 (a) which will result in errors during the doubly differential decoding. However, when the unwrap function is used it can be seen that the estimated trajectory has the same trend as the measured frequency offset with a constant frequency offset difference of 2.5GHz, which for this 10GBd system with T=100ps and M=4, is a multiple of $2\pi/(MT)$. Since it is a multiple of $2\pi/(MT)$, it will appear correctly after the hard decision and will be fully compensated for with the doubly differential decoding after the hard decision.

In terms of the complexity of implementing Mth power DDPSK, it is clear that the only additional functions which would be required on top of an Mth power SDPSK system would be one additional differential encoding operation at the transmitter, one additional differential decoding operation at the receiver after the hard decision, and an unwrap function in the Mth power frequency offset compensation algorithm.

5.4 Static Performance of Mth Power DDQPSK- BER versus OSNR[10]

The experimental setup to test the static BER versus OSNR performance of DDQPSK is shown in Figure 5.6. Note that many of the details provided in this section are given in the paper at [10] and the experimental data used here relates to the same simulation and experiment documented in [10].

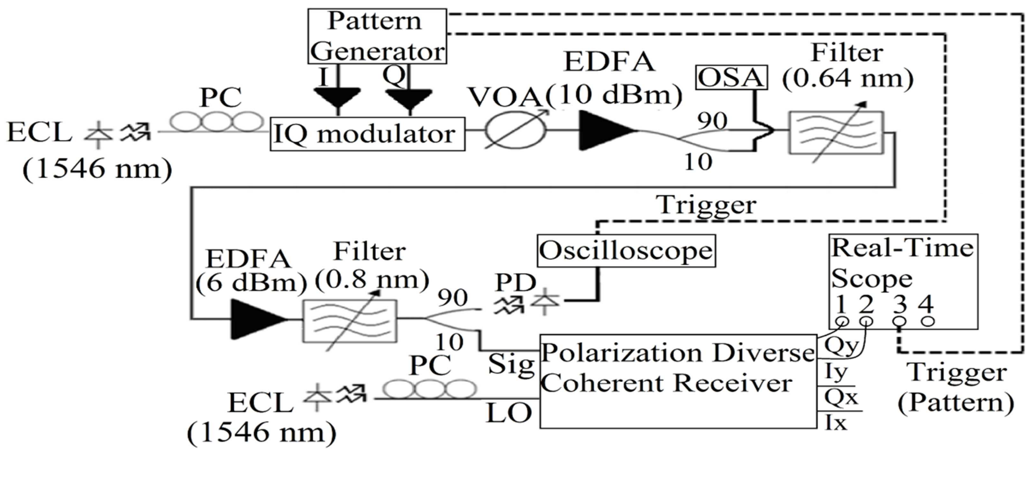

Figure 5.6: Experimental setup to perform BER versus OSNR measurements to compare Mth power SDQPSK, Simple DDQPSK and Mth power DDQPSK (diagram from [10]).

A low linewidth laser at 1546nm is used at the transmitter where a PC is used to rotate the input polarsation to that required by the IQ modulator. The transmitter and LO were both ECL sources which came from two different ports of a box which provided four outputs from four ECLs (Agilent Technologies “N7714A Tunable Laser Source” with a typical linewidth of less than 100kHz specified). The IQ modulator has inputs from a pattern generator whose signals are electrically amplified. A 2^7 -1 pseudo random bit sequence (PRBS), i.e. PRBS7, data sequence with a zero appended to it was generated in MATLAB and this data sequence was encoded for DDQPSK transmission, using the encoding scheme given in [8]. The encoded sequence was loaded onto the pattern generator or used in VPI TransmissionMaker V8.7 (a simulation tool for telecommunication systems using components in the optical or electrical domain) in order to simulate the experiment. The extra zero was included since the pattern generator only accepted particular pattern lengths. Note that the same recorded received data was also decoded as if it were SDQPSK encoded and the resulting data sequence compared against the data sequence expected from SDQPSK decoding of perfectly transmitted DDQPSK encoded data. The DDQPSK encoded I and Q data streams were then inputs into electrical amplifiers in the experiment whose outputs were inputs to an IQ modulator which modulated the transmitting laser’s output, with no electrical amplifiers used in the simulation. The symbol rate of the system was 10GBaud. The OSNR was varied by varying the attenuation of the variable optical attenuator (VOA) before the first EDFA. After the first EDFA, the OSNR was measured using a 10% tap from the EDFA output and measuring the OSNR from the OSA with a bandwidth of 0.14nm. The measured OSNR was later corrected using MATLAB so that it corresponded to a bandwidth resolution of 0.1nm. The other 90% went through a 0.64nm optical bandpass filter, then through a second EDFA, to maintain constant power and then through a 0.8nm optical bandpass filter.

After this, a 90% tap went to a photodiode connected to an oscilloscope which was used to observe the eye diagram in order to optimise the DC bias points of the IQ modulator (90% was required to provide sufficient clarity for the eye diagram). The oscilloscope for the eye diagram was triggered from a signal from the pattern generator. The other 10% went to the signal input of the polarisation-diverse coherent receiver. In simulation, a thermal noise value of 40pA/($Hz^{1/2}$) was used for the photodiodes in the receiver. Another low linewidth ECL at 1546nm was used as the LO and this went through a PC before entering the LO port of the polarisation diverse coherent receiver. Only the Y components of the polarisation diverse coherent receiver were recorded. In order to vary the frequency offset in the experiment and the simulation, the frequency of the ECL at the LO was varied. A real-time scope was used to record the data in the experiment with a sampling rate of 50GSample/s and an analogue bandwidth of 16GHz. The real-time scope was triggered with a periodic signal from the pattern generator. A 16GHz Butterworth filter was used in the simulations as this had the best match to the experimental conditions and the recorded data from the simulation was resampled to 5 samples per symbol. Offline DSP was performed in MATLAB. In the offline DSP, the data was downsampled to one sample per symbol, where the sample with the highest field amplitude was the sampling phase used. The BER was determined from direct error counting by comparing the expected data from DDQPSK or SDQPSK decoding with what was decoded in the presence of different OSNRs and different frequency offsets. 351 averaging terms were used in the M^{th} power frequency offset compensation algorithm and 13 averaging terms were used in the M^{th} power phase estimation algorithm. The expected data streams for Simple DDQPSK decoding and M^{th} power DDQPSK decoding were the same. More than $6.4*10^4$ bits, and more than $3.9*10^4$ bits, were used to calculate each BER value in the simulation and experimental results, respectively. This allowed for BERs of 10^{-3} to be measured accurately.

Shown in Figure 5.7 are the BER versus OSNR curves for static simulated and experimental systems using (a) M^{th} power SDQPSK decoding, (b) Simple DDQPSK decoding and (c) M^{th} power DDQPSK decoding. Note that from the theory already discussed the range of frequency offsets which M^{th} power SDQPSK can compensate for is between $-\pi/(MT)$ and $\pi/(MT)$ (or -1.25 GHz and 1.25GHz for the 10Gbaud work in this experiment). It should also be noted that M^{th} power SDQPSK can compensate for frequency offsets which can be expressed as $(2\pi((N/T)+ \delta_f))$, where N is an integer and δ_f is within the SDQPSK compensation range. This is the case as frequency offsets which are multiples of the symbol rate will rotate symbols a multiple of 2π between symbols. From Figure 5.7 (a) it can be seen that frequency offsets which are greater than 1.25GHz and less than 8.75GHz cannot be compensated for as expected. There is an OSNR offset between experimental and simulation results which could be due more noise being present in the experiments than the simulation, e.g. the thermal noise may be larger in experiment than in simulation, or power levels at different parts of the simulation may be different from experiment. From Figure 5.7 (b) it can be seen that all frequency offsets can be compensated for almost equally well, except for the experimental 10GHz curve. However, the OSNR required for a BER of 10^{-3} is approximately 24dB for almost all the curves which is approximately 10dB worse than that for the correctly decoded Mth power SDQPSK experimental curves in Figure 5.7 (a). However, for Mth power DDQPSK shown in Figure 5.7 (c) the BER versus OSNR performance is approximately the same for all frequency offsets with an OSNR offset of about 2dB between simulation and experimental results. It should be noted that the OSNR penalty of using Mth power DDQPSK instead of Mth power SDQPSK is less than 0.5dB at a BER of 10^{-3} which is in close agreement with the analysis above.

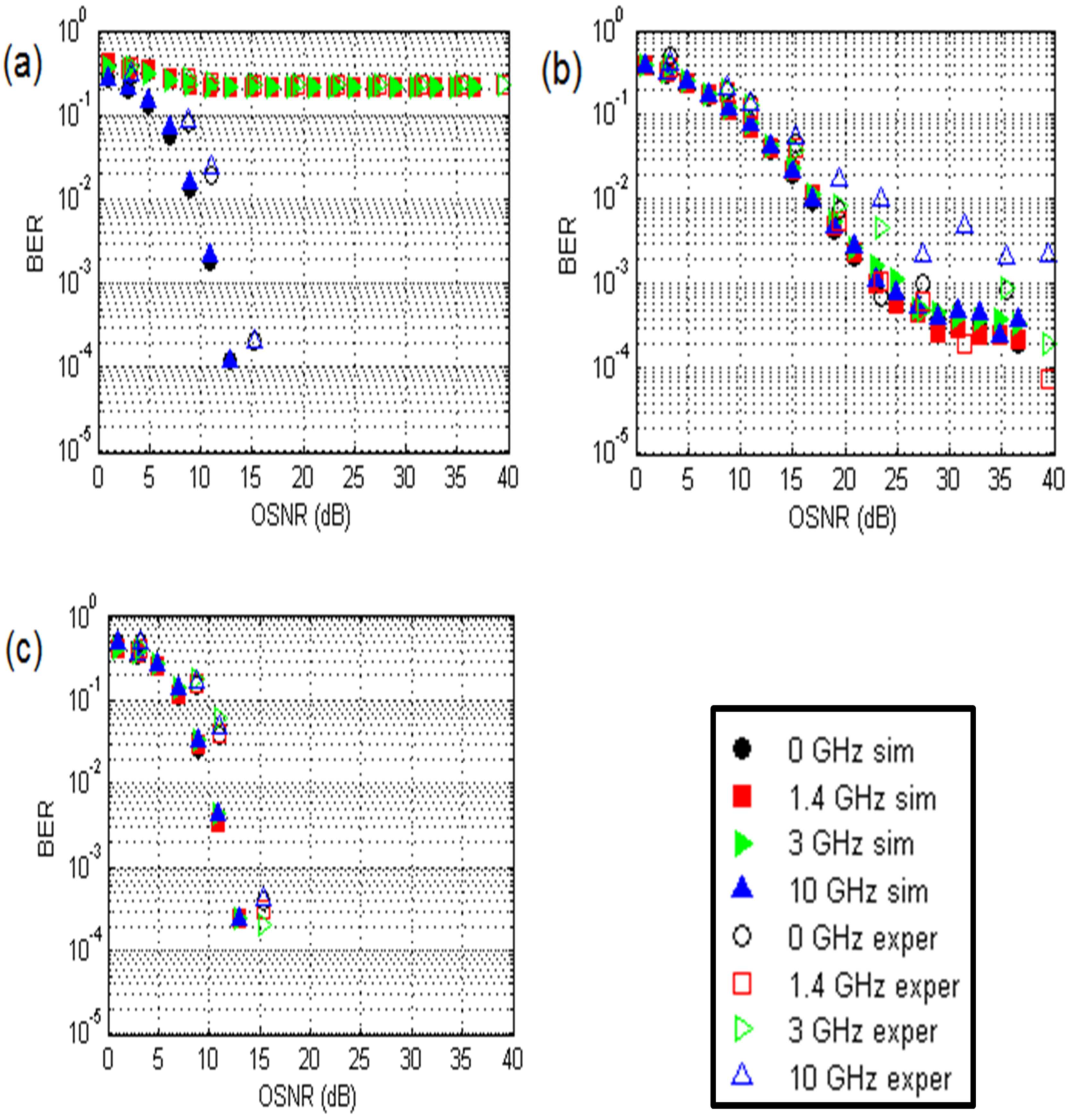

Figure 5.7: BER versus OSNR for different levels of frequency offset using simulation and experimental data decoded with (a) Mth power SDQPSK, (b) Simple DDQPSK and (c) Mth power DDQPSK.

Shown in Figure 5.8 is the OSNR required for a BER of 10^{-3} versus frequency offset, where the required OSNR was determined from a linear fit of $Log_{10}(-Log_{10}(BER))$ versus OSNR in dB. BER values greater than or equal to 0.4 were ignored for all the fittings and BER values less than $0.9*10^{-3}$ were ignored for Simple DDQPSK so that the fittings would be less affected by non-linear regions. It is clearly shown in Figure 5.8 that M^{th} power DDQPSK has a very similar OSNR requirement for a BER of 10^{-3} as M^{th} power SDQPSK, while having the same frequency offset range as Simple DDQPSK. Hence, it is clearly shown that M^{th} power DDQPSK could be used in static scenarios in order to provide a very large frequency offset tolerance.

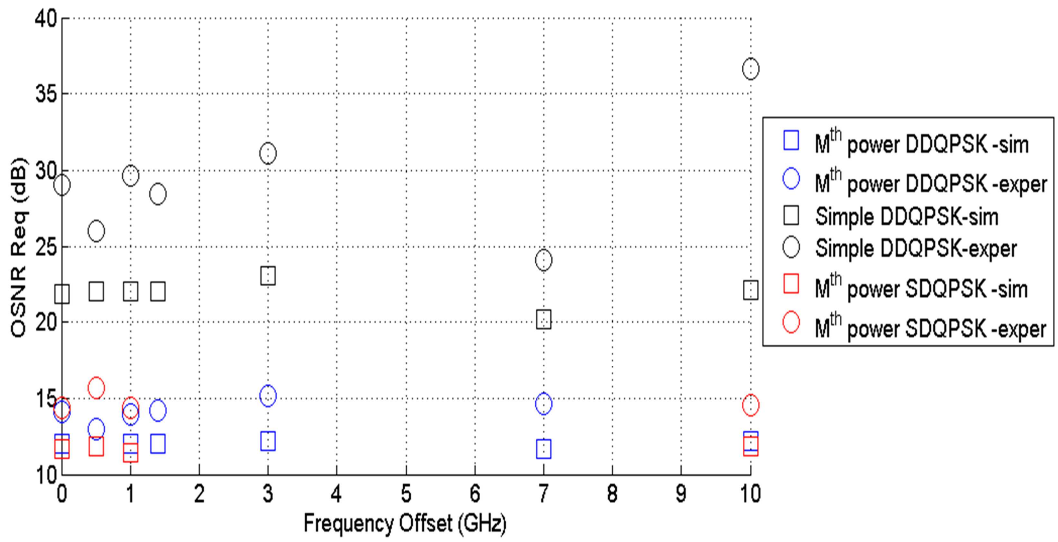

Figure 5.8: OSNR required for a BER of 10^{-3} versus frequency offset for simulation and experimental data using either M^{th} power SDQPSK, Simple DDQPSK or M^{th} power DDQPSK.

5.5 Switching Performance of M^{th} Power DDQPSK- BER versus OSNR[15]

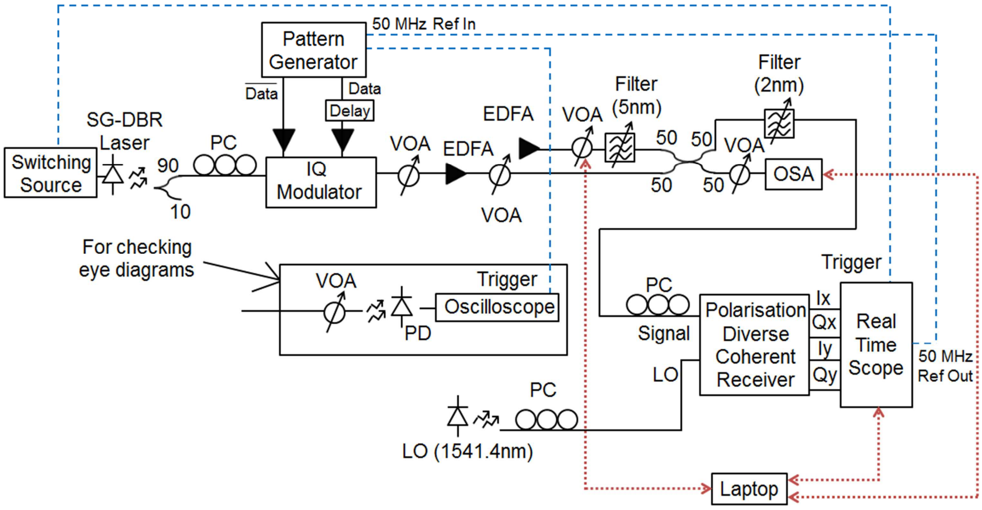

Figure 5.9: BER versus OSNR measurement scheme to assess the performance of different decoding schemes in a switching scenario.

Shown in Figure 5.9 is the experimental setup to test the performance of M^{th} power DDQPSK directly after a switching event using a tuneable laser transmitter (note that the material presented here was published in [15]). Here, the SG-DBR laser switches between 1541.4nm and 1547.5nm, with a switching voltage signal being applied to the back section. The laser stays on each wavelength for 500ns. The laser output went through a 90/10 coupler, where the 10% output was used to measure frequency offsets between the SG-DBR and the LO using the polarisation-diverse coherent receiver. The 90% output was modulated with an IQ modulator with data being provided by a pattern generator. The bit rate of the system was 20GBit/s (symbol rate of 10GBaud). The pattern used was a PRBS7 sequence of length 2^7-1. The delay used to decorrelate the data and inverse data streams was 15 bits. Note that the SDQPSK and DDQPSK decoded results are both related to the same bit sequences coming from the pattern generator, but the expected decoded bit sequences for SDQPSK and DDQPSK were both different. By decoding the known transmitted bit streams using either SDQPSK or DDQPSK decoding, the expected output data for each decoding scheme can be determined. Electrical amplifiers were used to provide high enough voltage levels for the data signals going into the IQ modulator. The bias points were optimised regularly using manual optimisation algorithm described in [18]. An oscilloscope was used to monitor the eye diagram of the modulator to ensure that the bias points of the modulator were set so as to give the expected DQPSK eye diagram with three levels at the transitions. The modulated laser output then went through a VOA, which had an inline power meter, and then an EDFA. Since the output of this EDFA was too high for the signal input of the polarisation-diverse coherent receiver (+6.5dBm) and could not be finely adjusted, a VOA was used after this EDFA. At the 50/50 coupler, noise was added to change the OSNR. The OSNR was varied using a VOA to attenuate ASE from the EDFA with no input. A 5nm filter was used to flatten the ASE noise spectrum where the flatness of the added ASE noise was determined using the OSA. One output from the 50/50 coupler went through a VOA and then went to an OSA in order to measure the OSNR. The resolution of the OSA was 0.1nm. The other output from the 50/50 coupler went through a 2nm filter and then through a PC before going to the signal port of the polarisation-diverse coherent receiver. The LO used was an ECL (NETTEST TLS WDM Source Model C with a specified linewidth of less than 100kHz). Note that TLS stands for “Tuneable laser source”. A static laser at 1541.4nm acting as the LO went through a PC and then into the LO port of the polarisation-diverse coherent receiver. Note that the PC at the signal port was set so as to maximise the power on only one polarisation. The real-time scope captured the outputs from the polarisation-diverse coherent receiver, with the real-time scope having a bandwidth of 12.5GHz and a sampling rate of 50GSample/s. The experiment was controlled using an automatic program which was run on a laptop. The laptop changed the attenuation of the VOA which varied the added ASE, measured the new OSNR value by gathering information from the OSA, and recorded data from the real-time scope at different OSNR values. More than 1.8×10^5 bits were used for each BER point which allowed for BERs of 10^{-3} to be measured accurately. 11 averaging terms were used in both the frequency offset estimation and phase estimation.

Shown in Figure 5.10 are the BER versus OSNR performance curves when using (a) M^{th} power SDQPSK, (b) Simple DDQPSK decoding and (c) M^{th} power DDQPSK. The red curves relate to decoding bursts with a waiting time of 30ns after the start of the burst (after the laser switched wavelength) and the blue curves are for a 0ns waiting time. The 0ns time is when the amplitude exceeds 70% of its maximum value, with 490ns after that time being used for the BER calculation which essentially relates to 98% utilization of the 500ns burst. The triangle symbols are for 0GHz steady-state frequency offsets (the frequency offset at the end of the switch) and the quadrangles are for 3GHz steady-state frequency offsets. It can be seen from Figure 5.10 (a) that the system is only able to produce BERs less than

10^{-3} for 0GHz steady-state frequency offsets and for 30ns waiting times. From Figure 5.10 (b) it can be seen that Simple DDQPSK cannot produce BERs less than 10^{-3}, however, its performance is similar for different steady-state frequency offsets and different waiting times. In Figure 5.10 (c) all the curves can reach BER values below 10^{-3} in the OSNR range shown and can start decoding with 0ns waiting times. There is also less than a 0.6dB difference between the 30ns wait time with 0GHz steady-state frequency offset curves in Figure 5.10 (a) and Figure 5.10 (c) at a BER of 10^{-3}. This is close to the expected penalty from the analysis above.

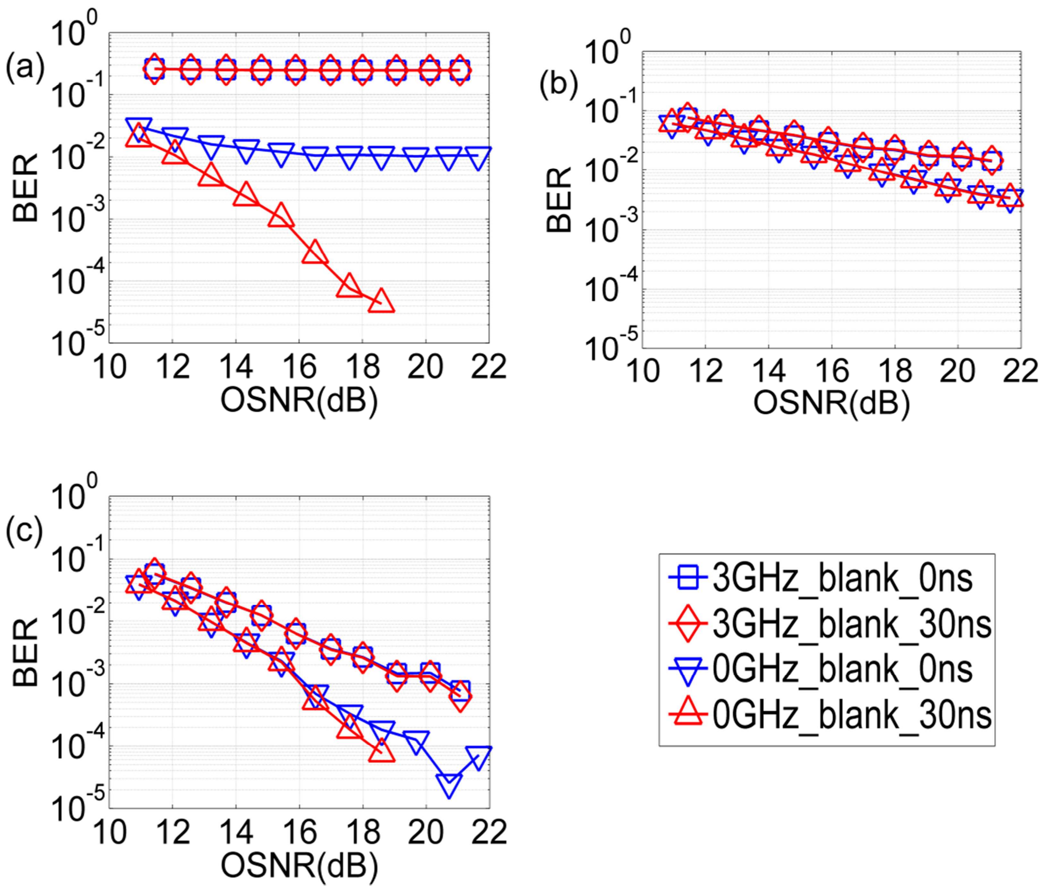

Figure 5.10: BER versus OSNR in a switching environment for different steady-state frequency offsets and different waiting times after a switch for (a) Mth power SDQPSK (b) Simple DDQPSK and (c) Mth power DDQPSK [15].

Note also that the measured and estimated frequency offset transients are shown in Figure 5.5. It should be noted that increasing the size of the moving average used in the Mth power frequency offset compensation stage will increase the accuracy of estimated static frequency offsets which will give lower BERs but may limit the maximum rate of change of frequency offset which can be tolerated and, hence, increase the waiting time. Hence, a trade-off between accuracy of the frequency offset and the maximum rate of change of frequency offset that can be tolerated needs to be taken into consideration. Note that the same averaging lengths were used for the results shown in Figure 5.10 (moving average lengths of 11 symbols for frequency offset compensation and phase estimation). This novel algorithm, M^{th} power DDPSK, allows for frequency offset range limitations previously associated with packet/ burst DP-QPSK receivers to be greatly relaxed, such as in [19] where the initialisation of the CMA equalizer must be delayed until the switching laser gets into the frequency offset compensation range. M^{th} power DDPSK can enable very short waiting times since data can be decoded as soon as the beat signal from the coherent receiver is within the receiver's electronic bandwidth.

5.6 Summary

In this chapter the novel approach of using doubly differential encoding and decoding was presented. The OSNR penalty typically associated with Simple DDPSK decoding was greatly reduced by using the novel M^{th} power DDPSK algorithm which has very similar BER versus OSNR performance to M^{th} power SDQPSK. The performance of M^{th} power DDQPSK was demonstrated and verified in static simulations and experiments. M^{th} power DDQPSK could also be used in static scenarios for improved robustness since this demodulation method can deal with large frequency offsets (limited by the bandwidth of the receiver electronics, where larger symbol rates will result in the data spectrum being filtered out by the receiver's low-pass filter response at lower frequency offsets). M^{th} power DDQPSK was shown to be able to overcome the issues of M^{th} power SDQPSK in a switching scenario, which mainly originate from its limited frequency offset compensation range. By using M^{th} power DDQPSK with its large frequency offset compensation range which is only limited by the bandwidth of the electronics (with the frequency offset range being decreased for larger symbol rates) it is possible to decode packets very soon after a switching event and at large steady-state frequency offsets. This solves the frequency offset issue associated with coherent optical burst/packet switched systems using frequency offset compensation algorithms with limited ranges. Having solved this issue, attention is turned to the other major challenge of coherent optical packet/burst switched receivers, which is demultiplexing dual-polarisation packets into separate polarisations, where the CMA methods used typically need to find some method of overcoming the singularity problem and can have variable decoding times. It will be shown next that a fully feed-forward method (initially proposed by a different group [20]) if used in a coherent optical packet/ burst switched system can overcome the variable convergence times issue associated with CMA [19], as well the singularity issue, and allowing for shorter waiting times for decoding dual-polarisation packets in a coherent optical packet/ burst switched networking scenario.

References

1. A. Leven, N. Kaneda, U. -V. Koc, and Y. -K. Chen, "Frequency Estimation in Intradyne Reception," IEEE Photonics Technology Letters **19,** 366-368 (2007).

2. B. C. Thomsen, R. Maher, D. S. Millar, and S. J. Savory, "Burst Mode Receiver for 112 Gb/s DP-QPSK with parallel DSP," Optics Express **19,** B770-B776 (2011).

3. J. C. M. Diniz, E. S. Rosa, V. B. Ribeiro, J. C. R. F. Oliveira, and A. C. Bordonalli, "Wide-Range Frequency Offset Estimator for DSP-based Optical Coherent Receivers," in *International Microwave & Optoelectronics Conference,* (IEEE, 2011), pp. 710-713.

4. T. Nakagawa, K. Ishihara, T. Kobayashi, R. Kudo, M. Matsui, Y. Takatori, and M. Mizoguchi, "Wide-Range and Fast-Tracking Frequency Offset Estimator for Optical Coherent Receivers," in *European Conference and Exhibition on Optical Communication,* (IEEE, 2010), pp. We.7.A.2.

5. S. Zhang, L. Xu, J. Yu, M. -. Huang, P. Y. Kam, C. Yu, and T. Wang, "Dual-Stage Cascaded Frequency Offset Estimation for Digital Coherent Receivers," IEEE Photonics Technology Letters **22,** 401-403 (2010).

6. X. Liu, S. Chandrasekhar, and A. Leven, "Self-coherent optical transport systems," in *Optical Fiber Telecommunications VB: Systems and Networks,* I. P. Kaminow, T. Li, and A. E. Willner, (Academic Press, Oxford, 2008), pp. 131-178.

7. Y. Gao, A. P. T. Lau, and C. Lu, "Residual Carrier-Aided Frequency Offset Estimation for Square 16-QAM Systems," in *OptoElectronics and Communications Conference/ International Conference on Photonics in Switching,* (IEEE, 2013), pp. TuPR-8.

8. D. L. Alphen and W. C. Lindsey, "Higher-Order Differential Phase Shift Keyed Modulation," IEEE Transactions on Communications **42,** 440-448 (1994).

9. M. Pent, "Double Differential PSK Scheme in the Presence of Doppler Shift," in *AGARD, Digital Communications in Avionics,* (AGARD, 1978), pp. 43-1-43-11.

10. A. J. Walsh, H. Shams, J. Mountjoy, A. Fagan, J. Zhao, L. P. Barry, and A. D. Ellis, "Demonstrating Doubly-Differential Quadrature Phase Shift Keying in the Optical Domain," IEEE Photonics Technology Letters **25,** 1054-1057 (2013).

11. R. G. Albano, L. Franchina, and S. A. Kosmopoulos, "Bit Error Performance Evaluation of Double-Differential QPSK in Faded Channels Characterized by Gaussian Plus Impulsive Noise and Doppler Effects," IEEE Transactions on Vehicular Technology **49,** 148-158 (2000).

12. S. Qu and S. M. Fleisher, "Double Differential MPSK on the Fast Rician Fading Channel," IEEE Transactions on Vehicular Technology **41,** 278-295 (1992).

13. H. Ishikawa and H. Kobayashi, "Frequency-Offset Compensation for MPSK Differential Detection by Using Double Differential Encoding," Electronics and Communicaitons in Japan, Part 1 **78,** 62-71 (1995).

14. M. Nazarathy, A. Gorshtein, and D. Sadot, "Doubly-Differential Coherent 100G Transmission: Multi-Symbol Decision-Directed Carrier Phase Estimation with Intradyne Frequency Offset Cancellation," in *Signal Processing in Photonic Communications,* (OSA, 2010), pp. SPWB4.

15. A. J. Walsh, J. Mountjoy, A. Fagan, C. Browning, A. D. Ellis, and L. P. Barry, "Reduced OSNR Penalty for Frequency Drift Tolerant Coherent Packet Switched Systems Using Doubly Differential Decoding," in *Optical Fiber Communication Conference and Exposition,* (IEEE, 2014), pp. Th4D.8.

16. K. Kikuchi, "Coherent optical communication systems," in *Optical Fiber Telecommunications VB: Systems and Networks,* I. P. Kaminow, T. Li, and A. E. Willner, (Academic Press, Oxford, 2008), pp. 95-130.

17. J. G. Proakis and M. Salehi, *Digital Communications, Fifth Edition* (McGraw-Hill, 2008).

18. L. Zhao, H. Shankar, and A. Nachum, "40G QPSK and DQPSK Modulation," (accessed 03/10/2014), http://www.inphi.com/technology-overview/40G-QPSK-and-DQPSK-Modulation.pdf

19. R. Maher, D. S. Millar, S. J. Savory, and B. C. Thomsen, "Widely Tunable Burst Mode Digital Coherent Receiver With Fast Reconfiguration Time for 112 Gb/s DP-QPSK WDM Networks," Journal of Lightwave Technology **30,** 3924-3930 (2012).

20. B. Szafraniec, B. Nebendahl, and T. Marshall, "Polarization demultiplexing in Stokes space," Optics Express **18,** 17928-17939 (2010).

Chapter 6

Dual-Polarisation Doubly Differential Phase Shift Keying

One of the key motivations behind using coherent detection is that spectrally efficient modulation formats can be used with typically only the DSP having to be changed for different modulation formats. One way of increasing spectral efficiency is to multiplex coherently modulated signals using two different polarisations. As discussed in chapter 3, where there is birefringence in the fibre this will effectively lead to the Jones vector at the input of the fibre being multiplied by an unknown unitary matrix. The typical method of compensating for this multiplication with a random unitary matrix in the case of polarisation multiplexed signals is to use some form of constant modulus algorithm (CMA), where a feedback algorithm updates filter coefficients so that the output constellations on each polarisation after the CMA tend towards constellations which have constant moduli, when using M-ary PSK data on each polarisation. When the CMA is used in coherent optical packet/burst switched scenarios issues arise such as the length of time required for convergence being long (hundreds of nanoseconds), variable and dependent on the input polarisation[1]. There can also be issues that both polarisations converge to the same polarisation which is known as the singularity problem. In this chapter a least mean squares (LMS) algorithm which uses Stokes parameters, described in [2], will be applied to a coherent optical burst scenario for the first time and it will be shown that this method can potentially overcome the issues associated with singularities and long variable convergence times seen in previous DP-QPSK methods. Consistent polarisation demultiplexing waiting times are critical to correctly designing a burst switched transmission protocol. Throughout this chapter M^{th} power DDQPSK will be used with either the LMS algorithm with Stokes parameters, or the CMA.

6.1 Description of the CMA

Shown in Figure 6.1 is the filter structure of the CMA used to demultiplex the two polarisations that are detected at the receiver. The crucial aspects of the CMA are how the initial values of the filters are set and how they are updated.

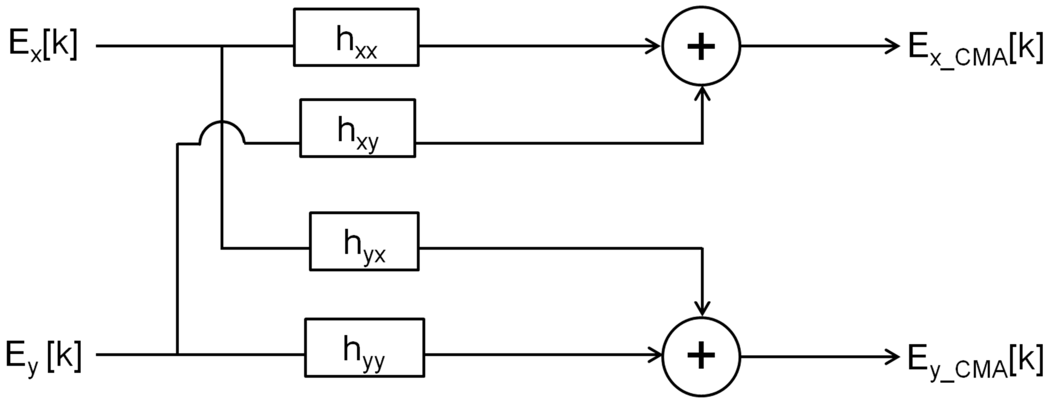

Figure 6.1: Schematic of how the CMA filters are applied to the input polarisation signals.

The input fields, $E_x[k]$ and $E_y[k]$, are normalised in the work here. The filters are updated using formulae given in [3] (using slightly different notation here):

$$h_{xx\_new} = h_{xx\_old} + \mu\varepsilon_x E_{x\_CMA} (E_x)^* \tag{6.1}$$

$$h_{xy\_new} = h_{xy\_old} + \mu\varepsilon_x E_{x\_CMA} .(E_y)^* \tag{6.2}$$

$$h_{yx\_new} = h_{yx\_old} + \mu\varepsilon_y E_{y\_CMA} .(E_x)^* \tag{6.3}$$

$$h_{yy\_new} = h_{yy\_old} + \mu\varepsilon_y E_{y\_CMA} .(E_y)^* \tag{6.4}$$

where the updated filters are on the left hand side of the equations (with “new” appended), the previous filters are on the right hand side of the equation (with “old” appended), μ is the convergence parameter, the input and output field terms (shown in Figure 6.1) are vectors whose length depends on the size of the filter used, and the error terms, ε_x and ε_y, are given by:

$$\varepsilon_x = 1 - \left|E_{x\_CMA}\right|^2 \tag{6.5}$$

$$\varepsilon_y = 1 - \left|E_{y\_CMA}\right|^2 \tag{6.6}$$

In [3], it was suggested that once the filters have converged a decision-directed LMS update algorithm be used which appears to give improved performance according to results in [3] (this is not the same as the Stokes parameter method which calculates a plane fit using an equation derived by LMS, which will be discussed later). However, the decision-directed LMS algorithm will not be used here and the CMA implementation above will instead be the only one used. Hence, the CMA will only begin its convergence at the start of a burst.

6.1.1 Methods of Initialising the CMA- Static Systems

There are many methods in the literature which suggest how to initialise the CMA for static channels. In [4], the X-polarisation filters are updated first until they have converged and then the Y-polarisation filters are determined by exploiting the fact that the channel matrix should be a unitary matrix. However, this may have varying convergence times depending on how far the initial guess is from a value considered to be a converged value, and this potential variability would mean that worst case convergence times would need to be assumed when designing the transmission and receiver system protocol. Another method given in [5] uses a two stage CMA method which can also monitor PDL and PMD, where the first stage uses a system similar to [4], but it may have variable convergence times as the first stage uses a system based on [4]. Another method is to use training symbols to initially determine the channel matrix which can achieve short waiting times that do not depend on the state of polarisation of the received field [6]. It should also be noted that there are methods other than the CMA such as the cost function method given in [7] which focus on maximising the average sum of the moduli on both polarisations which uses feedback, and is reported to require a few thousand symbols to converge which may be problematic for burst/ packet applications. Another approach is to consider a feed-forward method that does not require initialisation so that the system is guaranteed to stay stable. In [8], an algorithm which is claimed to be feed-forward is proposed, however, it does not seem to assume the general unitary matrix channel model for two polarisations, and [8] uses CMA in addition to the feed-forward method in experiment which would mean that it is not a fully feed-forward method. While these approaches focus on static scenarios, it is also important to discuss the convergence times of work published on packet/ burst scenarios.

6.2 Comparison of Contemporaneously Reported Coherent Optical Packet/ Burst Switching Systems

A number of groups have published in the area of coherent optical packet/burst switching since this work began [1, 9-13], where previously optical packet/burst systems focused on direct detection. One of the key distinguishing factors of the different published coherent optical packet/ burst switched receiver systems transmitting dual-polarisation M-ary PSK data is how they overcome the singularity/ initialisation problem of the CMA. In [14], a three stage CMA is used, where the two stages preceding the usual one stage CMA are used to initialise the CMA, however, this system has variable convergence times (maximum convergence time is 200ns or 11200 symbols) which means that it may be difficult to anticipate how long the CMA start-up time will be. Variable convergence times for DP-QPSK are also observed in [1] where a procedure using 25 initial test cases is required to initialise the CMA (with a maximum convergence time of approximately 410ns or 11480 symbols). Note that the group that performed the work in [1] have developed their work on switching DP-QPSK over a number of publications [15-20] and while [17] does report a waiting time of less than 150ns, it is in [1] that variations in waiting times due to changes in the input state of polarisation are explored leading, to the maximum convergence time of approximately 410ns.

It is also possible to use training symbols and pilot tones to assist optical packet/burst receivers at the cost of lower throughput and, in the case of training symbols, extra DSP to identify locations of the training symbols. Convergence times of CMA can be reduced by using cross-correlation and training patterns [10] where the maximum convergence times were reduced by more than half (from 3840 symbols (768ns) using only CMA to 1440 symbols (288ns) using polarisation back rotation from cross-correlations before applying CMA). Data-aided techniques for frequency transient compensation and channel estimation have been simulated [12] with 5% overhead for a 3.5μs burst and 500ns guard time. Experimental demonstration of a real-time burst-mode DP-QPSK receiver is described in [21] using data aided techniques (same group as [12]), however, requiring a 120ns guard time (3000 symbols). Dual-polarisation coherent orthogonal frequency division multiplexing (OFDM) in a burst scenario has also been published in [22, 23], however, pilot tones, training symbols of coherent OFDM and dropping of subcarriers reduce the efficiency of this scheme and it is not a truly blind system, e.g. in [22] 15 sub-carriers did not carrier data. 16-QAM switched systems using pilot tones have also been published [11, 24], however, these result in the loss of either one polarisation (did not use tuneable lasers) [11] or the loss of 2.5GHz of bandwidth between the data and the pilot tone [24].

It is also important to consider ways of improving waiting times by increasing hardware complexity. A direct way of determining the initial polarisation rotation matrices is to use the signal carvers which send a header in only one polarisation so that the state of polarisation can be determined using only 64 symbols (9ns), and use this determined state of polarisation to initialise the CMA for dual-polarisation transmission [13]. However, this will require additional equipment and, also, this system does not use fast switching tuneable lasers so it is not be affected by large frequency offset transients. It is also possible to use pre-emphasis of the drive signals to further improve switching performance when using fast switching tuneable lasers as performed in [25], where the cross-correlation method used in [10] is also used, where 100ns (2800 symbols) waiting time after the switch, the cross-correlation method can determine the polarisation with a 25ns (700 symbols) convergence time. In addition, work on dual-polarisation 16-QAM in a switching scenario has also been published [26], however, without the convergence times of the combined CMA pre-convergence and radius-directed equalizer being clearly presented, and this system employed a digital enhancement technique which increases implementation complexity. This digital enhancement technique requires the use of a delay line and an additional coherent receiver (the signal input of the additional coherent receiver is a delayed version of the LO used for data demodulation and the LO input of the additional coherent receiver is a copy of the LO used for data demodulation with a frequency shift potentially applied) [27, 28].

An ideal polarisation demultiplexing algorithm for burst-mode applications should have a number of key features. Firstly, it should not have convergence times which are long, variable and dependent on the state of polarisation of the input signal. Secondly, it should not have the potential to suffer from the singularity problems associated with the CMA. Thirdly, it should not use training symbols since they increase overhead, require additional DSP to recognise the start of the training symbols, and can potentially result in bursts of errors if they are sent during large channel fluctuations, which are more likely to occur at the start of a burst. Finally, hardware complexity should be kept as low as possible. One type of system which satisfies the requirements of eliminating variable convergence times and potentially not requiring initialisation would be a feed-forward system. By eliminating variable convergence times, long worst case convergence times can be avoided and this can potentially reduce waiting times. A scheme which satisfies the above constraints will be described next and it will be shown to require a 30ns (300 symbols) waiting time.

6.3 Description of the LMS Algorithm

The motivation for using the LMS algorithm described in [2] is that it is a feed-forward algorithm, it does not require an initial channel matrix, does not suffer from the singularity issue, does not have variable convergence times and does not require additional hardware. The fact that the algorithm is feed-forward means that any large errors observed by the system will eventually be forgotten which ensures a certain degree of system stability. In addition, unlike CMA and other feedback mechanisms, there is no need to select an initial channel matrix which simplifies the operation of the demultiplexing algorithm. It should be clear that not having the singularity issue is a great advantage. In addition, not having variable convergence times for polarisation demultiplexing provides certainty which will allow for more straightforward design of burst/ packet switched networks.

The first step is to determine the down-converted X and Y polarisation fields using the polarisation diverse coherent receiver. In the work here the receiver outputs Ix, Iy, Qx and Qy have their offsets removed, magnitudes normalised, deskews removed, and, then, are downsampled to one sample per symbol (note that it is explained in [2] that the LMS method is independent of the clock frequency so polarisation demultiplexing could be done before clock recovery but here polarisation demultiplexing is done using signals downsampled to one sample per symbol). Similar to the previous chapter, the sampling phase was determined by selecting the sampling phase which had the largest average magnitude. These outputs are then used to determine the X and Y polarisation fields, E_x and E_y respectively, as follows:

$$E_x = \left(I_x + jQ_x\right) \tag{6.7}$$

$$E_y = \left(I_y + jQ_y\right) \tag{6.8}$$

Then, the s-parameters can be calculated using equations from [2] (the real value function is used in the calculations here to ensure that each calculation is always real but this is not explicitly done in [2]):

$$s_0 = \frac{1}{2}\mathrm{Re}\left(E_x\left(E_x\right)^* + E_y\left(E_y\right)^*\right) \tag{6.9}$$

$$s_1 = \frac{1}{2}\mathrm{Re}\left(E_x\left(E_x\right)^* - E_y\left(E_y\right)^*\right) \tag{6.10}$$

$$s_2 = \frac{1}{2}\mathrm{Re}\left(\left(E_x\right)^* E_y + E_x\left(E_y\right)^*\right) \tag{6.11}$$

$$s_3 = \frac{1}{2}\mathrm{Re}\left(-j\left(E_x\right)^* E_y + jE_x\left(E_y\right)^*\right) \tag{6.12}$$

The key observation pointed out in [2] is that for dual-polarisation M-ary QPSK, s_1, s_2 and s_3 (for the non-downsampled case) form a “lens” shape object in the 3D space. The orientation of the lens shape is dependent on the unitary matrix of the channel where a normal vector to the plane which best fits the lens can be used to determine the unitary matrix of the channel. It is also argued in [2] that all constellations, except ones that have only single lines or points in a complex plane, will form the “lens” shape in 3D space and, hence, this provides the possibility for a general polarisation demultiplexer for any polarisation-multiplexed M-QAM. Note that it can be shown that for DP-QPSK downsampled to one sample per symbol with optimum sampling phase that (s_1, s_2, s_3) points lie on a perfectly flat surface in 3D-space in the presence of no noise, with the normal vector to that surface containing sufficient information to determine the demultiplexing matrix for that channel. Assuming a unitary matrix channel, the best fit plane through this flat surface can be shown to go through the origin and this can be exploited to reduce the LMS calculations required.

To calculate the normal vector to the plane, (a_1, a_2, -1), the following LMS matrix equation can be used (this was derived by the author of the thesis, with the derivation shown in section 6.4 below):

$$\begin{bmatrix} a_1 \\ a_2 \end{bmatrix} = \begin{bmatrix} \sum_{i=-N}^{i=N} \left(s_1[i]\right)^2 & \sum_{i=-N}^{i=N} s_1[i]s_2[i] \\ \sum_{i=-N}^{i=N} s_1[i]s_2[i] & \sum_{i=-N}^{i=N} \left(s_2[i]\right)^2 \end{bmatrix}^{-1} \begin{bmatrix} \sum_{i=-N}^{i=N} s_1[i]s_3[i] \\ \sum_{i=-N}^{i=N} s_2[i]s_3[i] \end{bmatrix} \tag{6.13}$$

The equations to calculate two important parameters for the compensating matrix, $\Delta\Phi_{LMS}$ and θ_{LMS}, are slightly different from the equations used in [2] since one of the fitting terms has been removed by utilizing the fact that the plane goes through the origin (the notation is also slightly different from [2]):

$$\Delta\Phi_{LMS} = \mathbf{atan2}\left[a_2, -1\right] \tag{6.14}$$

$$\theta_{LMS} = \frac{1}{2}\mathbf{atan2}\left[a_1, \sqrt{a_2^2+1}\right] \tag{6.15}$$

where **`atan2[p,q]`** is the MATLAB command for the two-argument arctan where p is the cos input and q is the sin input (its output is in the range ($-\pi$, π]). The compensating matrix, $M_{inverse}$, can then be calculated using the equation given in [2]:

$$M_{inverse} = \begin{bmatrix} \cos(\theta_{LMS}).e^{j\Delta\Phi_{LMS}/2} & \sin(\theta_{LMS}).e^{-j\Delta\Phi_{LMS}/2} \\ -\sin(\theta_{LMS}).e^{j\Delta\Phi_{LMS}/2} & \cos(\theta_{LMS}).e^{-j\Delta\Phi_{LMS}/2} \end{bmatrix} \quad (6.16)$$

Shown in Figure 6.2 are two different perspectives of a downsampled DP-DDQPSK 3D plot of (s_1, s_2, s_3) represented by blue dots and the LMS best-fit plane is traced out with red lines. The plot in Figure 6.2 (a) shows four distinctive (s_1, s_2, s_3) clusters of points and the plot in Figure 6.2 (b) is just a rotated version of Figure 6.2 (a) showing the plane and these clusters from a different perspective. It is important to note that the fitting needs to be repeated three times as the plane to be fitted to might be parallel to the surface with s_1=0, the surface with s_2=0, or the surface with s_3=0. When applying the LMS algorithm three times, the s_1, s_2, and s_3 points should be cyclically swapped so that the axes are effectively rotated ensuring that at least one fitting will not contain an infinite slope.

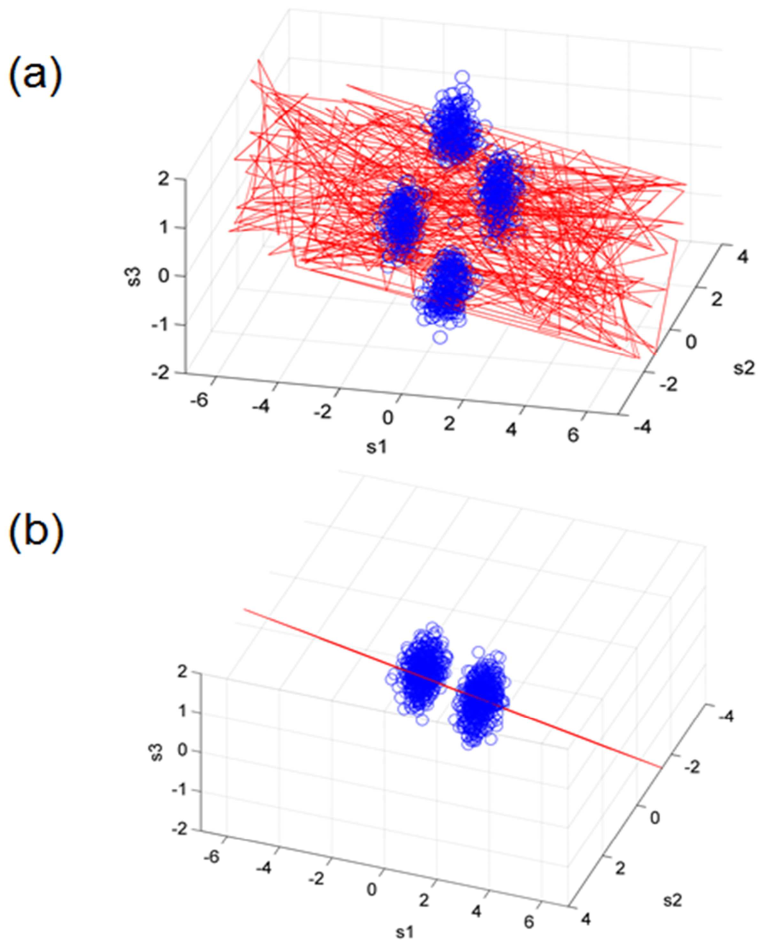

Figure 6.2: 3D plot of (s_1, s_2, s_3) points calculated using DP-DDQPSK experimental data (blue dots) with a linear plane fit (red lines) shown from two different perspectives.

6.4 Derivation of the Stokes Space Plane Estimation Equation Using a LMS Approach

The following section will derive the Stokes space plane estimation equation given in equation (6.13) using a LMS approach. Here, s_1, s_2, and s_3 will be replaced by x, y, and z respectively as it makes following the equations easier. Since the fitted plane is expected to go through the origin the following equation applies:

$$a_{plane}\, x + b_{plane}\, y + z = 0 \tag{6.17}$$

where a_{plane} and b_{plane} are real numbers. Note that a c_{plane} coefficient for z is not necessary as both sides of the equation can be divided by c_{plane} without loss of generality, except for $c_{plane}=0$. It is this $c_{plane}=0$ case, as well as the $b_{plane}=0$ and $a_{plane}=0$ cases, which makes it necessary to rotate (s_1, s_2, s_3) three times and then apply this LMS algorithm for each rotation. In addition, by not having a c_{plane} coefficient the possible solutions for a_{plane} and b_{plane} are reduced from an infinite set of possible pairs of values to one possible pair of values. If a set of points is produced which is expected to agree with the relationship given in equation (6.17), then in order to find the best fit to that equation in the least mean squares sense the following variable, ERR_{LMS}, should be minimised, where ERR_{LMS} is given by:

$$ERR_{LMS} = \sum_{i=-N}^{i=N} \left(a_{LMS}\, x_i + b_{LMS}\, y_i + z_i\right)^2 \tag{6.18}$$

where the indexing is done so that the averaging takes place over symbols before and after the current point in time being investigated. a_{LMS} and b_{LMS} are the estimated values of a_{plane} and b_{plane} respectively. In order to minimise ERR_{LMS}, ERR_{LMS} should be differentiated with respect to one of the control variables, either a_{LMS} or b_{LMS}. Differentiating with respect to a_{LMS} yields:

$$\frac{dERR_{LMS}}{da_{LMS}} = \sum_{i=-N}^{i=N} 2\left(a_{LMS}\, x_i + b_{LMS}\, y_i + z_i\right) x_i \tag{6.19}$$

which implies that:

$$\frac{dERR_{LMS}}{da_{LMS}} = 2\sum_{i=-N}^{i=N} \left(a_{LMS}\, x_i^{\,2} + b_{LMS}\, y_i x_i + z_i x_i\right) \tag{6.20}$$

Using similar calculations to those given in equations (6.19) and (6.20) it is possible to show that the derivative of ERR_{LMS} with respect to b_{LMS} is given as:

$$\frac{dERR_{LMS}}{db_{LMS}} = 2\sum_{i=-N}^{i=N}\left(b_{LMS}y_i^{\,2} + a_{LMS}y_ix_i + z_iy_i\right) \tag{6.21}$$

Since a_{LMS} and b_{LMS} can assume any real value and do not have a restricted range here, maximum and minimum ERR_{LMS} values will occur when the derivatives equal zero. Hence, it is of interest to find where the derivatives in equations (6.20) and (6.21) equal zero. For the derivative with respect to a_{LMS}:

$$\frac{dERR_{LMS}}{da_{LMS}} = 0 \tag{6.22}$$

$$2\sum_{i=-N}^{i=N}\left(a_{LMS}x_i^{\,2} + b_{LMS}y_ix_i + z_ix_i\right) = 0 \tag{6.23}$$

$$\sum_{i=-N}^{i=N}\left(a_{LMS}x_i^{\,2}\right) + \sum_{i=-N}^{i=N}\left(b_{LMS}y_ix_i\right) + \sum_{i=-N}^{i=N}\left(z_ix_i\right) = 0 \tag{6.24}$$

$$\sum_{i=-N}^{i=N}\left(a_{LMS}x_i^{\,2}\right) + \sum_{i=-N}^{i=N}\left(b_{LMS}y_ix_i\right) = -\sum_{i=-N}^{i=N}\left(z_ix_i\right) \tag{6.25}$$

Repeating the same arguments except with the derivative with respect to b_{LMS} given in equation (6.21) yields:

$$\sum_{i=-N}^{i=N}\left(b_{LMS}y_i^{\,2}\right) + \sum_{i=-N}^{i=N}\left(a_{LMS}y_ix_i\right) = -\sum_{i=-N}^{i=N}\left(z_iy_i\right) \tag{6.26}$$

Combining equations (6.25) and (6.26) into matrix form yields:

$$\begin{bmatrix} \sum_{i=-N}^{i=N}\left(x_i^{\,2}\right) & \sum_{i=-N}^{i=N}\left(y_ix_i\right) \\ \sum_{i=-N}^{i=N}\left(y_ix_i\right) & \sum_{i=-N}^{i=N}\left(y_i^{\,2}\right) \end{bmatrix} \begin{bmatrix} a_{LMS} \\ b_{LMS} \end{bmatrix} = \begin{bmatrix} -\sum_{i=-N}^{i=N}\left(z_ix_i\right) \\ -\sum_{i=-N}^{i=N}\left(z_iy_i\right) \end{bmatrix} \tag{6.27}$$

Multiplying both sides of the equation by the inverse of the 2x2 matrix yields:

$$\begin{bmatrix} a_{LMS} \\ b_{LMS} \end{bmatrix} = \begin{bmatrix} \sum_{i=-N}^{i=N}\left(x_i^{\,2}\right) & \sum_{i=-N}^{i=N}\left(y_ix_i\right) \\ \sum_{i=-N}^{i=N}\left(y_ix_i\right) & \sum_{i=-N}^{i=N}\left(y_i^{\,2}\right) \end{bmatrix}^{-1} \begin{bmatrix} -\sum_{i=-N}^{i=N}\left(z_ix_i\right) \\ -\sum_{i=-N}^{i=N}\left(z_iy_i\right) \end{bmatrix} \tag{6.28}$$

Converting (x, y, z) back to (s_1, s_2, s_3), respectively, and denoting the coefficients multiplying s_1, s_2 and s_3 as ($-a_1$), ($-a_2$) and 1, respectively, the following LMS equation emerges:

$$\begin{bmatrix} -a_1 \\ -a_2 \end{bmatrix} = \begin{bmatrix} \sum_{i=-N}^{i=N} (s_1[i])^2 & \sum_{i=-N}^{i=N} s_2[i]s_1[i] \\ \sum_{i=-N}^{i=N} s_2[i]s_1[i] & \sum_{i=-N}^{i=N} (s_2[i])^2 \end{bmatrix}^{-1} \begin{bmatrix} -\sum_{i=-N}^{i=N} s_3[i]s_1[i] \\ -\sum_{i=-N}^{i=N} s_3[i]s_2[i] \end{bmatrix} \quad (6.29)$$

which can be re-written as:

$$\begin{bmatrix} a_1 \\ a_2 \end{bmatrix} = \begin{bmatrix} \sum_{i=-N}^{i=N} (s_1[i])^2 & \sum_{i=-N}^{i=N} s_1[i]s_2[i] \\ \sum_{i=-N}^{i=N} s_1[i]s_2[i] & \sum_{i=-N}^{i=N} (s_2[i])^2 \end{bmatrix}^{-1} \begin{bmatrix} \sum_{i=-N}^{i=N} s_1[i]s_3[i] \\ \sum_{i=-N}^{i=N} s_2[i]s_3[i] \end{bmatrix} \quad (6.30)$$

Hence, it can be seen that the LMS equations given in equations (6.13) and (6.30) are the same and can be used to find coefficients to fit a flat plane to (s_1, s_2, s_3). Using these coefficients, it is possible to determine a vector normal to the plane of this surface [29]:

$$v_{norm\,1} = \begin{bmatrix} -a_1 & -a_2 & 1 \end{bmatrix} \quad (6.31)$$

or

$$v_{norm\,2} = \begin{bmatrix} a_1 & a_2 & -1 \end{bmatrix} \quad (6.32)$$

Using this normal vector and the equations provided in [2] equations (6.14) and (6.15**)** can be verified to be correct. Equation (6.16) is provided in [2].

6.5 Differential Polarisation Encoding: 2-D Differential Encoding Rule

When sending polarisation multiplexed M-ary PSK data it is possible even after the two polarisations have been separated that the X-polarisation transmitted data will end up on the decoded Y-polarisation output at the receiver and vice versa after the DSP. It is also possible that each transmitted data stream will end up on the correct polarisation output at the receiver. One way to overcome this ambiguity is to transmit initialisation symbols to identify which decoded polarisation is which. While this is a simple and straightforward method, problems could arise if the initialisation symbols are transmitted with errors. For a burst/ packet switched system, a robust method of overcoming this ambiguity is required as the initialisation symbols are likely to be sent at the start of the packet where errors are probably most likely.

In [30], a method of differentially encoding the data on both polarisations is provided, which appears to be termed as the “2-D differential encoding rule”, along with a method of decoding the data at the receiver such that it is possible to identify which decoded data stream corresponds to which transmitted polarisation data stream. A block diagram of this method is shown in a block diagram in Figure 6.3, with the 2-D differential encoding rule at the transmitter shown in Figure 6.3 (a), and the 2-D differential decoding rule at the receiver shown in Figure 6.3 (b). The key aspect to realise about this algorithm is that if the inputs to the differential polarisation decoder in Figure 6.3 (b), $\hat{b}_{pol\,X}[k]$ and $\hat{b}_{polY}[k]$, are swapped then the same data streams will appear on $\hat{a}_{pol\,X}[k]$ and $\hat{a}_{polY}[k]$ as if the inputs had not been swapped. Hence, whether the polarisation demultiplexing algorithm produces a demultiplexing matrix which puts the X-polarisation field on the Y output and the Y-polarisation field on the X output, or puts both polarisation fields on the correct outputs, the 2-D differential decoding rule will ensure that the X-polarisation data is always on the $\hat{a}_{pol\,X}[k]$ output, and Y-polarisation data is always on the $\hat{a}_{polY}[k]$ output.

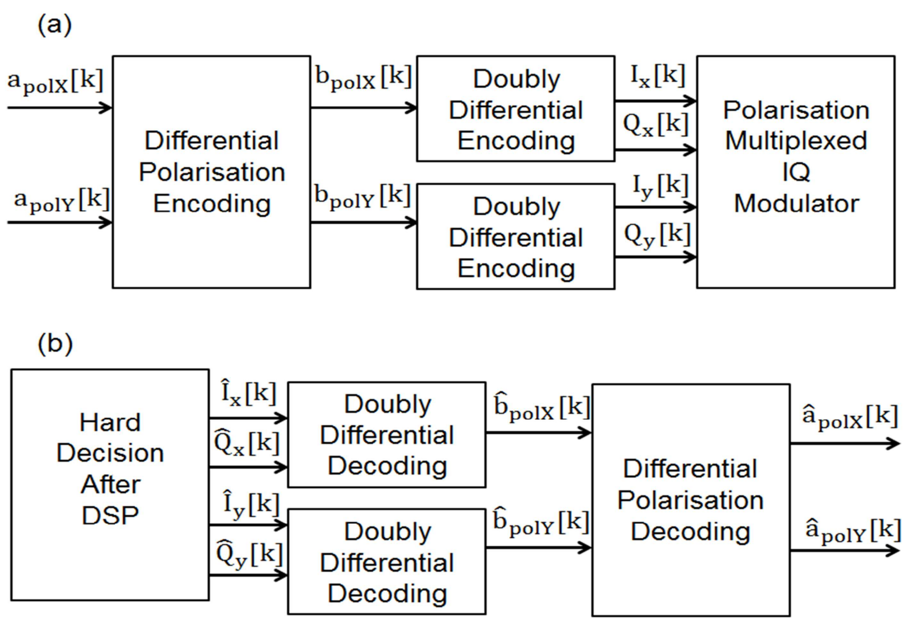

Figure 6.3: Block diagram of implementation of (a) 2-D differential encoding rule at the transmitter and (b) 2-D differential decoding rule at the receiver.

Let the terms $a_{polX}[k]$ and $a_{polY}[k]$ represent the two data streams to be transmitted in a polarisation multiplexed M-QAM system, where $a_{polX}[k]$ and $a_{polY}[k]$ are integers selected from the set $S_{pol}=\{0,1,\ldots,M\text{-}1\}$ with each M-QAM symbol being associated with a member of this set. The encoding at the transmitter can be implemented as follows [30]:

$$b_{polX}[k] = \begin{cases} a_{polX}[k], \text{ if } \sigma_{pol}[k] = -1 \\ a_{polY}[k], \text{ if } \sigma_{pol}[k] = 1 \end{cases} \tag{6.33}$$

$$b_{polY}[k] = \begin{cases} a_{polY}[k], \text{ if } \sigma_{pol}[k] = -1 \\ a_{polX}[k], \text{ if } \sigma_{pol}[k] = 1 \end{cases} \tag{6.34}$$

$$\sigma_{pol}[k+1] = \begin{cases} -1, \text{ if } b_{polX}[k] < b_{polY}[k] \\ \sigma_{pol}[k], \text{ if } b_{polX}[k] = b_{polY}[k] \\ 1, \text{ if } b_{polX}[k] > b_{polY}[k] \end{cases} \tag{6.35}$$

where $b_{polX}[k]$ and $b_{polY}[k]$ are the 2-D differentially encoded symbols which are elements of S_{pol}, and $\sigma_{pol}[k]$ is the state variable at the transmitter. The data streams $b_{polX}[k]$ and $b_{polY}[k]$ should then be converted to the appropriate complex symbols associated with their integer representations from S_{pol}. Then, $b_{polX}[k]$ and $b_{polY}[k]$ have their phases encoded using doubly differentially encoding (this step can be replaced by single differential encoding or no phase encoding at all depending on the particular implementation used on each polarisation). After the phase encoding, the Ix, Qx, Iy and Qy data signals are used to modulate the carrier at the transmitter.

At the receiver, after performing downsampling, polarisation demultiplexing, frequency offset compensation, phase estimation, hard decision and single or doubly differential phase decoding (or possible no phase decoding), 2-D differential decoding can be performed on the resulting data streams from the two polarisations, $\hat{b}_{pol\,X}[k]$ and $\hat{b}_{polY}[k]$, using the following decoding scheme [30]:

$$\hat{a}_{polX}[k] = \begin{cases} \hat{b}_{polX}[k], \text{ if } \hat{\sigma}_{pol}[k] = -1 \\ \hat{b}_{polY}[k], \text{ if } \hat{\sigma}_{pol}[k] = 1 \end{cases} \tag{6.36}$$

$$\hat{a}_{polY}[k] = \begin{cases} \hat{b}_{polY}[k], \text{ if } \hat{\sigma}_{pol}[k] = -1 \\ \hat{b}_{polX}[k], \text{ if } \hat{\sigma}_{pol}[k] = 1 \end{cases} \tag{6.37}$$

$$\hat{\sigma}_{pol}[k+1] = \begin{cases} -1, \text{ if } \hat{b}_{polX}[k] < \hat{b}_{polY}[k] \\ \hat{\sigma}_{pol}[k], \text{ if } \hat{b}_{polX}[k] = \hat{b}_{polY}[k] \\ 1, \text{ if } \hat{b}_{polX}[k] > \hat{b}_{polY}[k] \end{cases} \tag{6.38}$$

where, $\hat{a}_{pol\,X}[k]$ and $\hat{a}_{polY}[k]$ are the estimated data symbols, and $\hat{\sigma}_{pol}[k]$ is the state variable at the receiver (note that $\hat{b}_{pol\,X}[k]$, $\hat{b}_{polY}[k]$, $\hat{a}_{pol\,X}[k]$ and $\hat{a}_{polY}[k]$ are all in integer form and elements of S_{pol}). In terms of BER versus SNR, the SNR penalty associated with using the 2-D differential encoding rule with two polarisation streams is estimated from simulations in [30] to be less than 0.1dB. One important point to note is that the state variable at the receiver, $\hat{\sigma}_{pol}[k]$, at the receiver will only be initialised when two different symbols are present at $\hat{b}_{pol\,X}[k]$ and $\hat{b}_{polY}[k]$, at the same k. If $\hat{\sigma}_{pol}[k]$ is initially incorrect, symbol errors affecting both polarisation will occur but only at the first time where $\hat{b}_{pol\,X}[k]$ and $\hat{b}_{polY}[k]$ are different. If, for example, the first 16 pairs of symbols (pairs of $\hat{b}_{pol\,X}[k]$ and $\hat{b}_{polY}[k]$) are the same but for the 17th pair of symbols there are different symbols and the initial value of $\hat{\sigma}_{pol}[k]$ is incorrect, then errors will only occur for the 17th pair of symbols but not for the first 16 pairs of symbols. Assuming that random data is transmitted, the probability of two different symbols not having different values within 20 symbols for QPSK is less than $9.1*10^{-13}$, with this probability being even lower for larger M-QAM constellations, thus ensuring that the state variable at the receiver, $\hat{\sigma}_{pol}[k]$, will be initialised very quickly.

6.6 LMS Stokes Parameters Algorithm and CMA: Static and Switching Performance[9]

6.6.1 Experimental System to Determine the Performance of Different Polarisation Demultiplexing Algorithms

The experimental setup to investigate the performance of DP-DDQPSK in static and switching scenarios and compare the LMS and CMA demultiplexing methods is shown in Figure 6.4. This setup was used to measure BER versus OSNR curves. Note that many details of this work have been published by the author [9].

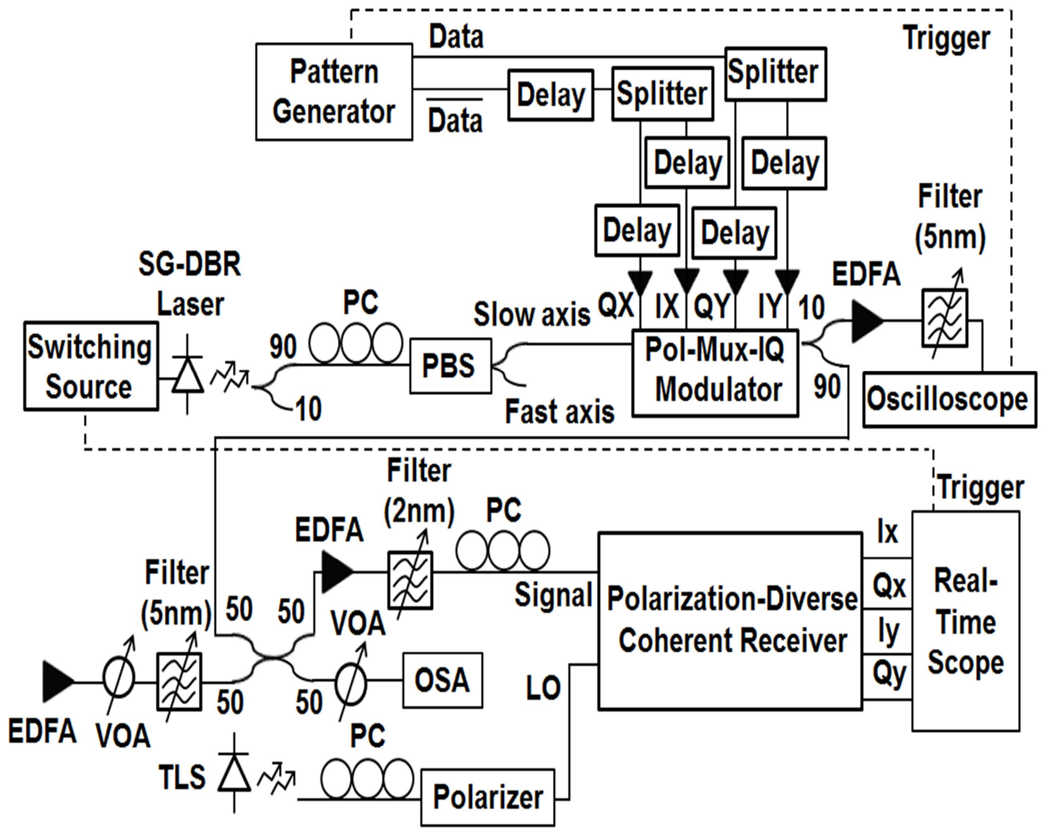

Figure 6.4: Experimental setup for BER versus OSNR measurements for DP-DDQPSK in static and switching scenarios [9].

The transmitter laser, which is an SG-DBR laser, switches wavelength in the switching scenarios by applying a 1MHz square wave voltage to the back section of the laser and uses a constant voltage for the static scenarios. It switches between 1541.2nm and 1547.4nm. The SG-DBR initially goes through a 90/10 coupler where the 10% is used to measure the precise frequency offset between the SG-DBR and the LO using the polarisation-diverse coherent receiver. The LO is based on an ECL design (NETTEST TLS WDM Source Model C with a specified linewidth of less than 100kHz). The LO is kept close to 1541.2nm. At the start of experiments 10 frequency offsets (with no data present) were recorded so that the relative deskews between the four outputs of the polarisation-diverse coherent receiver could be measured. It was necessary to use multiple frequency offsets so that small time delays could be determined between I_x and I_y, and between Q_x and Q_y with the correct deskew correction leading to identical elliptical fits to I_y versus I_x parametric plots for each frequency offset, and the same would be the case for Qy versus Qx parametric plots. Also, correct deskew correction would lead to circular parameter plots for Qx versus Ix, and Qy versus Iy. The 90% output of the 90/10 coupler after the SG-DBR laser went through a polarisation controller and then through a PBS. The PBS was used to ensure that the state of polarisation of the light going into the modulator was aligned with the slow axis. The power from the fast axis output was minimised by varying the polarisation controller so as to maximise the power on the slow axis output. The pattern generator produced a PRBS7 2^7-1 data stream and its inverse. Delays and splitters were used to create four electrical output data signals. The delays were 25 bits between Iy and Qy, 10 bits between Ix and Qx, and 31 bits between Qx and inverted Iy. By setting up the delays in this manner it was possible to identify which decoded data stream was which in order to ascertain if the decoding process had swapped the data streams. The symbol rate of the system was 10 GBaud, giving a bit rate of 40 Gbit/s. The modulator used was an integrated dual-polarisation QPSK modulator. A quad electrical amplifier was used to amplify the four electrical data signals so that they could adequately drive the dual-polarisation QPSK modulator. The output of the modulator went to another 90/10 splitter where the 10% output was amplified with an EDFA, then filtered with a 5nm optical bandpass filter and then went to an oscilloscope to observe the eye-diagram in order to optimise the bias points of the modulator. The oscilloscope was triggered with a signal from the pattern generator. The observation of the eye-diagram and optimisation of the DC bias points of the modulator was performed using an automatic program. The 90% output of the second 90/10 coupler went to a 50/50 coupler which was where the ASE noise was added at the other input using an EDFA with no input, a VOA, and another 5nm optical bandpass filter used to flatten the added noise near the wavelength of the data signal. One output of the 50/50 coupler went to another VOA whose output went to an OSA in order to measure the OSNR with a reference bandwidth of 0.1nm. The other output of the 50/50 coupler went to another EDFA, then a 2nm optical bandpass filter, then to a polarisation controller before going to the input of the polarisation-diverse coherent receiver. The LO, which is a TLS based on an ECL design, initially goes through a polarisation controller, then through a polarizer in order to ensure that the state of polarisation is correct before going to the LO input of the polarisation-diverse coherent receiver. The four outputs of the polarisation-diverse coherent receiver are recorded by a real-time scope. The real-time scope has a sampling rate of 50GSample/s and a bandwidth of 12.5GHz. A laptop automatically changed the VOA which attenuated the ASE noise in order to vary the OSNR, read the OSNR measured by the OSA, and saved the signals recorded by the real-time scope. The recorded signals were then analysed in MATLAB using offline DSP. The real-time scope was triggered by the square wave applied to the SG-DBR in the switching cases in order to maximise the number of packets captured in each screen shot of the real-time scope.

In the offline DSP, the signals had their offsets removed, their amplitudes normalised and their deskews removed. The signals were then downsampled to one sample per symbol using the sampling phase of E_X with the maximum average amplitude. The polarisation demultiplexing is then performed using either the CMA or the LMS algorithm. 201 symbols were used in the moving average filters in the LMS averaging, and finite impulse response filters of length 1 were used in the CMA with a convergence parameter of $\mu=0.0158$ used. In the case of switching, the CMA is only set running when a packet is detected while the LMS algorithm can be kept running as it is a feed-forward algorithm. The frequency offset is removed using the M^{th} power frequency offset algorithm with the unwrap function included since M^{th} power DDQPSK was being used, with the reasons for this having been explained in the previous chapter. 101 symbols were used in the moving average filter in the M^{th} power frequency offset compensation algorithm. The phase estimation was performed using the M^{th} power phase estimation algorithm, where 11 symbols were used in the moving average filter. A hard decision was then made. Doubly differential decoding was then performed on the hard decision bits. In the case that no 2-D differential decoding of the two polarisation streams was used (described in section 6.5) then the decoded X polarisation data was compared with the bit pattern which gave it the lowest BER (from the two expected bit patterns which were expected to be on separate polarisations) and the decoded Y polarisation data was compared with the other expected bit pattern. In the case of singularities this would mean that the decoded Y polarisation would have very high BERs. In the case of using 2-D differential decoding with the polarisation streams, the decoded bit patterns were compared with the bit patterns they would be expected to match from the algorithm given in [30]. In terms of determining the bit patterns expected, this was done by decoding the expected Ex and Ey fields expected from knowledge of the data pattern produced by the pattern generator and from knowledge of the delays used in the experiment.

6.6.2 Static and Switching Experimental Results

The average BER over both polarisations versus OSNR for polarisation multiplexed M^{th} power DDQPSK using either the LMS or CMA algorithms with no

2-D differential decoding is shown in Figure 6.5. Shown in Figure 6.6 is essentially the same plot as shown in Figure 6.5 except using 2-D differential decoding.

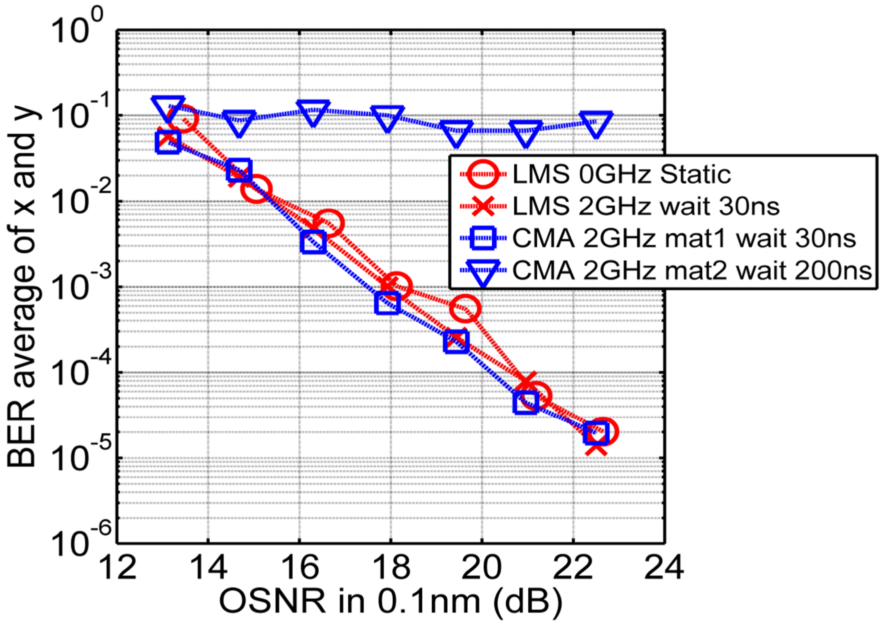

Figure 6.5: Average BER over X and Y polarisations versus OSNR for DP-DDQPSK using either the CMA [3] or the LMS algorithm [2] for polarisation demultiplexing with different waiting times after a switching event and with frequency offsets reported with no 2-D differential decoding [9].

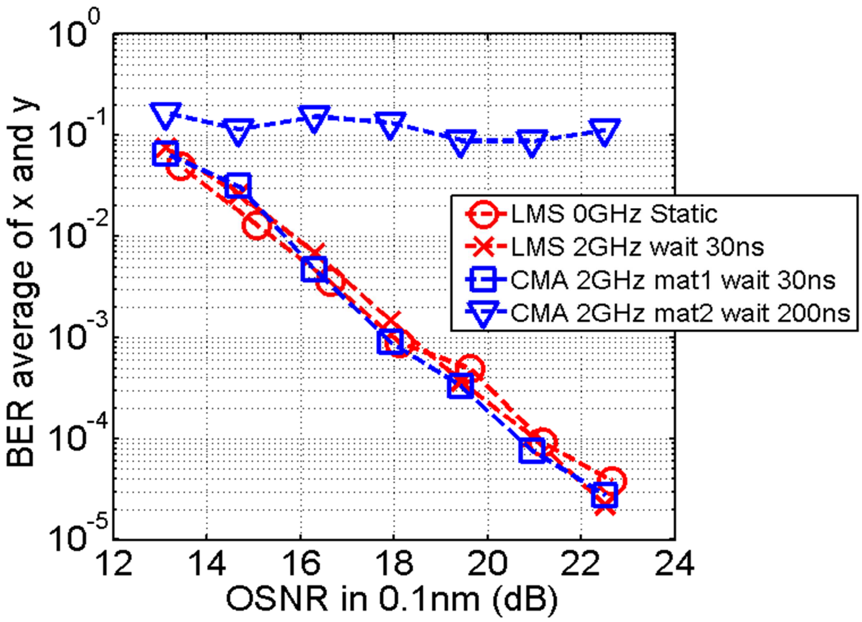

Figure 6.6: Average BER over both polarisations versus OSNR for DP-DDQPSK with 2-D differential encoding used.

The only static curves included in these figures are the ones with the red circles indicating the performance of the LMS algorithm with a 0GHz frequency offset between the transmitter and LO lasers. All other curves are for when the laser transmitter is switching between wavelengths (1541.2nm and 1547.4nm). The LO wavelength is kept close to 1541.2nm. The red “x” curves have a steady-state frequency offset of 2GHz (i.e. the frequency offset value at the end of the packet), use the LMS decoding algorithm, and have a 30ns wait time after the start of a packet before BER values are calculated. The blue squares have a steady-state frequency offset of 2GHz, use CMA with a wait time of 30ns, and use an initial unitary matrix designated as “mat1”. The blue triangles have a steady-state frequency offset of 2GHz, use CMA with a wait time of 200ns, and an initial unitary matrix designated as “mat2” (mat1 and mat2 are two different unitary matrices).

In terms of analysing the results, it can be seen that the performance with and without using 2-D differential decoding is approximately the same, with all the correctly decoded curves having BERs of 10^{-3} at OSNR values close to 18dB. It can be seen that static LMS has quite similar performance to the switching case for both sets of curves. It was demonstrated with the two CMA curves that if the initial matrix is changed it can completely change the performance of the CMA from correct decoding after a 30ns wait with mat1, to high BER values even after a 200ns wait with mat2. Note that the precautions against using an initial matrix which would result in a singularity discussed previously were not utilised here. The results show that the LMS method has correctly decoded the switching data and that the CMA may not properly decode the data if an initial matrix is selected which results in a singularity which will result in a loss of data. Note that the reasons for preferring the use of the LMS method over the CMA are that the LMS method cannot result in a singularity since the compensating matrix in equation (6.16) can never be singular, and the LMS method does not have issues to do with variable convergence times since it is a feed-forward method that only needs to wait for all the terms in its moving average filters to be filled with values from a packet.

6.7 Summary

It has been shown in this chapter that by applying the LMS method in coherent optical packet switched networks, which has not been done before, waiting times can be achieved that are shorter than have been previously reported for wavelength switched DP-QPSK systems (30ns or 300 symbols). The CMA was shown to suffer from the singularity issue which is an issue which the LMS method does not suffer from. The LMS method also does not have issues with variable convergence times and does not require additional hardware. It was also discussed how using the 2-D differential encoding rule can provide a robust method of solving the ambiguity about which output polarisation channel contains which transmitted data stream and this method was experimentally demonstrated. The 2-D differential encoding rule could provide for a more robust method of solving this ambiguity in coherent optical packet/burst scenarios than tagging the polarisations as this tagging would most likely be implemented at the start of a packet where errors could be more likely at this part of the packet. Hence, a fully robust, feed-forward coherent optical packet/ burst switched receiver system has been presented and demonstrated with very short waiting times, which is robust against large frequency offsets and is not sensitive to the state of polarisation of the received packet.

References

1. R. Maher, D. S. Millar, S. J. Savory, and B. C. Thomsen, "Widely Tunable Burst Mode Digital Coherent Receiver With Fast Reconfiguration Time for 112 Gb/s DP-QPSK WDM Networks," Journal of Lightwave Technology **30,** 3924-3930 (2012).

2. B. Szafraniec, B. Nebendahl, and T. Marshall, "Polarization demultiplexing in Stokes space," Optics Express **18,** 17928-17939 (2010).

3. S. J. Savory, "Digital filters for coherent optical receivers," Optics Express **16,** 804-817 (2008).

4. L. Liu, Z. Tao, W. Yan, S. Oda, T. Hoshida, and J. C. Rasmussen, "Initial Tap Setup of Constant Modulus Algorithm for Polarization De-multiplexing in Optical Coherent Receivers," in *Optical Fiber Communication Conference and Exposition,* (IEEE, 2009), pp. OMT2.

5. C. Xie and S. Chandrasekhar, "Two-Stage Constant Modulus Algorithm Equalizer for Singularity Free Operation and Optical Performance Monitoring in Optical Coherent Receiver," in *Optical Fiber Communication Conference and Exposition,* (IEEE, 2010), pp. OMK3.

6. M. Morsy-Osman, M. Chagnon, Q. Zhuge, X. Xu, M. E. Mousa-Pasandi, Z. A. El-Sahn, and D. V. Plant, "Ultrafast and low overhead training symbol based channel estimation in coherent M-QAM single-carrier transmission systems," Optics Express **20,** B171-B180 (2012).

7. R. Schmogrow, P. C. Schindler, C. Koos, W. Freude, and J. Leuthold, "Blind Polarization Demultiplexing With Low Computational Complexity," IEEE Photonics Technology Letters **25,** 1230-1233 (2013).

8. T. Yoshida, T. Sugihara, H. Goto, T. Tokura, K. Ishida, and T. Mizuochi, "Fast Feed-Forward Polarization Tracking in a DP-mPSK Coherent Receiver Employing

Blind SOP Estimation," in *Optical Fiber Communication Conference and Exposition,* (IEEE, 2012), pp. OTh4C.6.

9. A. J. Walsh, J. Mountjoy, A. Fagan, C. Browning, A. D. Ellis, and L. P. Barry, "Reduced Waiting Times Using a Fast Switching Dual-Polarization DDQPSK Receiver in a Packet Switched Network," in *European Conference and Exhibition on Optical Communication,* (IEEE, 2014), pp. P.4.2.

10. J. Gripp, J. E. Simsarian, S. Corteselli, and T. Pfau, "Wavelength-Tunable Burst-Mode Receiver with Correlation-Based Polarization Separation," in *European Conference and Exhibition on Optical Communication,* (IET, 2013), pp. Th.2.A.3.

11. S. Shinada, M. Nakamura, Y. Kamio, and N. Wada, "16-QAM Optical Packet Switching with Real-time Self-homodyne Detection using Polarization-multiplexed Pilot-carrier," in *European Conference and Exhibition on Optical Communication,* (IEEE, 2012), pp. We.2.A.2.

12. M. Li, N. Deng, F. N. Hauske, Q. Xue, X. Shi, Z. Feng, S. Cao, and Q. Xiong, "Optical Burst-mode Coherent Receiver with a Fast Tunable LO for Receiving Multi-wavelength Burst Signals," in *Optical Fiber Communication Conference and Exposition,* (IEEE, 2012), pp. OTu1G.3.

13. F. Vacondio, C. Simonneau, A. Voicila, E. Dutisseuil, J. -. Tanguy, J. -. Antona, G. Charlet, and S. Bigo, "Real-time implementation of packet-by-packet polarization demultiplexing in a 28 Gb/s burst mode coherent receiver," in *Optical Fiber Communication Conference and Exposition,* (IEEE, 2012), pp. OM3H.6.

14. J. E. Simsarian, J. Gripp, A. H. Gnauck, G. Raybon, and P. J. Winzer, "Fast-Tuning 224-Gb/s Intradyne Receiver for Optical Packet Networks," in *Optical Fiber Communication Conference and Exposition,* (IEEE, 2010), pp. PDPB5.

15. B. C. Thomsen, R. Maher, D. S. Millar, and S. J. Savory, "Burst Mode Receiver for 112 Gb/s DP-QPSK," in *European Conference and Exhibition on Optical Communication,* (IEEE, 2011), pp. Mo.2.A.5.

16. B. C. Thomsen, R. Maher, D. S. Millar, and S. J. Savory, "Burst Mode Receiver for 112 Gb/s DP-QPSK with parallel DSP," Optics Express **19,** B770-B776 (2011).

17. R. Maher, D. S. Millar, S. J. Savory, and B. C. Thomsen, "Fast Switching Burst Mode Receiver in a 24-Channel 112Gb/s DP-QPSK WDM System with 240km Transmission," in *Optical Fiber Communication Conference and Exposition,* (IEEE, 2012), pp. JW2A.57.

18. R. Maher, D. S. Millar, S. J. Savory, and B. C. Thomsen, "Fast Wavelength Switching 112Gb/s Coherent Burst Mode Transceiver for Dynamic Optical Networks," in *European Conference and Exhibition on Optical Communication,* (IEEE, 2012), pp. Tu.3.A.2.

19. R. Maher, D. S. Millar, S. J. Savory, and B. C. Thomsen, "Fast Wavelength Switching 100Gb/s Burst Mode Transceiver for COherent Metro Networks," in *International Conference on Photonics in Switching (PS),* (IEEE, 2012), pp. 0076.

20. R. Maher, D. S. Millar, S. J. Savory, and B. C. Thomsen, "SOA Blanking and Signal Pre-Emphasis for Wavelength Agile 100Gb/s Transmitters," in *Opto-Electronics and Communications Conference,* (IEEE, 2012), pp. 905-906.

21. M. Li, N. Deng, Q. Xue, G. Gong, Z. Feng, and S. Cao, "A 100-Gb/s Real-time Burst-mode Coherent PDM-DQPSK Receiver," in *European Conference and Exhibition on Optical Communication,* (IET, 2013), pp. PD2.D.4.

22. R. Maher, K. Shi, S. J. Savory, and B. C. Thomsen, "Fast Wavelength Switching Digital Coherent OFDM Transceiver," in *European Conference and Exhibition on Optical Communication,* (IET, 2013), pp. Mo.3.C.3.

23. R. Maher, H. Chin, M. P. Thakur, D. Lavery, P. Bayvel, S. J. Savory, and B. C. Thomsen, "Fast Wavelength Switching DP-OFDM Transceiver in a 5-Node 800km Coherent OBS Network," in *Optical Fiber Communication Conference and Exposition,* (IEEE, 2014), pp. Tu2G.4.

24. T. N. Huynh, L. Nguyen, V. Vujicic, and L. P. Barry, "Pilot-Tone-Aided Transmission of High-Order QAM for Optical Packet Switched Networks," Journal of Optical Communications and Networking **6,** 152-158 (2014).

25. J. E. Simsarian, J. Gripp, S. Chandrasekhar, and P. Mitchell, "Fast-Tuning Coherent Burst-Mode Receiver for Metropolitan Networks," IEEE Photonics Technology Letters **26,** 813-816 (2014).

26. R. Maher, D. Lavery, M. Paskov, P. Bayvel, S. J. Savory, and B. C. Thomsen, "Fast Wavelength Switching 6 GBd Dual Polarization 16QAM Digital Coherent Burst Mode Receiver," IEEE Photonics Technology Letters **26,** 297-300 (2014).

27. M. Secondini, G. Meloni, T. Foggi, G. Colavolpe, L. Potì, and E. Forestieri, "Phase Noise Cancellation in Coherent Optical Receivers by Digital Coherence Enhancement," in *European Conference and Exhibition on Optical Communication,* (IEEE, 2010), pp. P4.17.

28. D. Lavery, R. Maher, M. Paskov, B. C. Thomsen, P. Bayvel, and S. J. Savory, "Digital Coherence Enhancement Enabling 6-GBd DP-64QAM Using a 1.4-MHz Linewidth Laser," IEEE Photonics Technology Letters **25,** 2213-2216 (2013).

29. E. Kreyszig, *Advanced Engineering Mathematics, Ninth Edition* (John Wiley & Sons, 2006).

30. G. Colavolpe, T. Foggi, E. Forestieri, and G. Prati, "Robust Multilevel Coherent Optical Systems With Linear Processing at the Receiver," Journal of Lightwave Technology **27,** 2357-2369 (2009).

Chapter 7

Conclusions and Future Work

There appears to be an insatiable demand for higher data rates through fibre optic telecommunication networks for internet applications. This is one motivation for the use of spectrally efficient modulation formats which can achieve higher transmission rates, and these modulation formats are often implemented with the use of coherent detection at the receivers. In addition, more efficient use of network resources is important and using OBS or OPS can potentially reduce the usage of electronic routing which could reduce the energy consumption in the network. Also, OBS and OPS can improve the temporal utilisation of network resources as demands between nodes in the network change with time.

Previous work in this field focused on intensity modulation and direct detection scheme. The use of coherent optical packet/ burst switched networks would help to achieve both high transmission rates, through greater spectral efficiency, and reduced energy consumption in the network. The use of OPS or OBS usually requires the use of fast switching tuneable lasers at the transmitter and/ or receiver and these switching tuneable lasers tend to exhibit large, time-varying frequency transients after switching. In addition, the use of coherent optical detection to allow for decoding of spectrally efficient modulation formats will require that impairments such as frequency offsets, phase noise and polarisation rotations need to be compensated/ mitigated in a robust and timely manner in OBS or OPS scenarios. The focus of this thesis work has been to fully understand the switching behaviour of the tuneable lasers being used, and to develop a robust coherent optical packet/ burst switched receiver so that coherent optical packet/ burst switched networks can be realised.

7.1 Contributions of This Thesis

The research questions and problems addressed in this thesis are described next along with their proposed solutions.

Simultaneous Time-Resolved Characterisation of Frequency Chirp and Phase Noise Dynamics: Time-Resolved 3D-CCDF of Instantaneous Differential Phase

There was an issue in the literature in that the time-resolved phase dynamics of fast switching tuneable lasers did not have a fully consistent method of characterisation. The main issues were: (i) the need to make assumptions about the probability distribution of the phase noise, (ii) the resolution not being limited by time-bandwidth constraints associated with FFT methods, and (iii) resolving the confusion between time-resolved frequency chirp and time-varying phase noise dynamics so as to characterise both deterministic and random phase noise dynamics into a single consistent method. The proposed novel time-resolved 3D-CCDF of the instantaneous differential phase characterisation technique simultaneously takes into account deterministic frequency chirp and dynamic random phase noise, with no assumptions made about the probability distribution of the phase noise. The 3D-CCDF of the instantaneous differential phase has a time-resolution which is only dependent on the sampling rate used. The validity of this approach has been clearly verified with very close matching between measured time-resolved BER curves and expected time-resolved BER curves calculated from the time-resolved 3-D CCDF plots.

Need for a Blind Frequency Offset Compensation Algorithm with a Large Tolerance Range: Mth Power DDPSK

An issue facing many coherent optical packet/ burst receivers was that they could only tolerate a limited frequency offset range when using blind frequency offset compensation methods using one sample per symbol. This meant that a large waiting time was required for the switching laser to settle so that the frequency offset would be in the tolerable range. As well as this, the steady-state frequency offset could be so large that it would not be inside the tolerable range. By using the proposed novel decoding method developed in this work, Mth power DDPSK, it was possible to tolerate any frequency offset within the bandwidth of the receiver electronics (larger symbols rates will be filtered out at lower frequency offset). Mth power DDPSK is more robust than using training symbols; especially if training symbols are used at the start of a burst since large frequency offset transients at the start of a burst would make errors more probable at this part of the burst. Not only does this solve a major issue in coherent optical packet/ burst switched networks but could potentially be applied to coherent M-ary PSK transmission systems in general. In addition, M^{th} power DDPSK is a method of greatly reducing the OSNR penalty associated with simple DDPSK while still retaining the large frequency offset tolerance range.

Initial Matrix Selection Problem and Sensitivity to the State of Polarisation of the Received Packet When Using CMA: DP-DDQPSK Optical Packet Receivers Using LMS Polarisation Decoding

A key issue with coherent optical packet/ burst receivers is the operation of the CMA when used for polarisation demultiplexing DP-QPSK signals in switching scenarios. The issues are usually: (i) the initialisation of the CMA, (ii) the occurrence of singularities, and (iii) convergence times of the CMA (which can be large, variable and sometimes dependent on the state of polarisation of the received packet). One way to completely overcome these issues is to use the LMS method which uses Stokes parameters in order to determine the compensation matrix in a feed-forward manner which means that issues to do with stability do not occur as errors will eventually be forgotten by the system. In addition, the LMS method cannot produce singular compensating matrices, does not require initialisation, and will not have variable convergence times that might vary depending on the state of polarisation of the received packet, with its waiting times only determined by the size of the moving average filters employed. The application of this LMS method in coherent optical packet/ burst switched scenarios had not been done before, hence its application in this scenario is novel, and as well as appropriate for the reasons given above. The additional use of M^{th} power DDPSK allows for a fully robust coherent optical packet/ burst receiver with very short waiting times, which is precisely what was sought after at the outset of this work.

7.2 Possible Future Research Directions

There are a number of different ways that the research presented in this thesis could be further developed. Shown below are some of the potential directions that a continuation of this research could go in.

- Firstly, investigating ways to implement a decoding method for 16-QAM or general M-QAM which has a frequency offset tolerance limited only by the bandwidth of the electronics (with signals at higher symbols rates being filtered out at lower frequency offsets). This could possibly be done by appropriately modifying the DDPSK approach or by a completely different approach.

- Secondly, the approximately 1dB penalty between M^{th} power DDQPSK and QPSK could possibly be further reduced by undertaking further research into novel DSP algorithms.
- Finally, real-time implementation of the proposed M^{th} power DDPSK decoding scheme using LMS polarisation demultiplexing with FPGAs would show that this receiver can be potentially implemented in the field.

Appendix A: List of Published Papers

Journal Papers

- **A. J. Walsh**, J. A. O’Dowd, V. M. Bessler, K. Shi, F. Smyth, J. M. Dailey, B. Kelleher, L. P. Barry, and A. D. Ellis, "Characterization of time-resolved laser differential phase using 3D complementary cumulative distribution functions," Optics Letters 37, 1769-1771 (2012).
- J. A. O’Dowd, K. Shi, **A. J. Walsh**, V. M. Bessler, F. Smyth, T. N. Huynh, L. P. Barry, and A. D. Ellis, "Time Resolved Bit Error Rate Analysis of a Fast Switching Tunable Laser for Use in Optically Switched Networks," Journal of Optical Communications and Networking 4, A77-A81 (2012).
- **A. J. Walsh**, H. Shams, J. Mountjoy, A. Fagan, J. Zhao, L. P. Barry, and A. D. Ellis, "Demonstrating Doubly-Differential Quadrature Phase Shift Keying in the Optical Domain," IEEE Photonics Technology Letters 25, 1054-1057 (2013).

Conference Papers

- J. A. O’Dowd, V. M. Bessler, S. K. Ibrahim, **A. J. Walsh**, F. H. Peters, B. Corbett, B. Roycroft, P. O'Brien, and A. D. Ellis, "Implementation of a High Speed Time Resolved Error Detector Utilising a High Speed FPGA," in International Conference on Transparent Optical Networks, (IEEE, 2011), pp. We.D1.2.
- J. Mountjoy, **A. J. Walsh**, B. Cardiff, J. A. O’Dowd, L. P. Barry, A. Ellis, and A. Fagan, "Optical Data Transmission with Fluctuating Frequency Offset and Strong Phase Noise," in Signal Processing in Photonic Communications, (OSA, 2013), pp. SP4D.5.
- **A. J. Walsh**, T. N. Huynh, J. Mountjoy, A. Fagan, A. D. Ellis, and L. P. Barry, "Employing DDBPSK in optical burst switched systems to enhance throughput," in European Conference and Exhibition on Optical Communication, (IET, 2013), pp. P.3.17.
- **A. J. Walsh**, J. Mountjoy, A. Fagan, C. Browning, A. D. Ellis, and L. P. Barry, "Reduced OSNR Penalty for Frequency Drift Tolerant Coherent Packet Switched Systems Using Doubly Differential Decoding," in Optical

Fiber Communication Conference and Exposition, (IEEE, 2014), pp. Th4D.8.

- J. Mountjoy, **A. Walsh**, L. P. Barry, and A. Fagan, "Improved Laser Phase Noise Tolerance for 2.5 Gbaud DPSK Transmission Using Trellis-Coded Modulation," in Signal Processing in Photonic Communications, (OSA, 2014), pp. ST5D.3.
- **A. J. Walsh**, J. Mountjoy, A. Fagan, C. Browning, A. D. Ellis, and L. P. Barry, "Reduced Waiting Times Using a Fast Switching Dual-Polarization DDQPSK Receiver in a Packet Switched Network," in European Conference and Exhibition on Optical Communication, (IEEE, 2014), pp. P.4.2.

Appendix B: Proof for Chapter 3

To Prove:

Given that:

$$\Delta\Phi_{est}(kT_s) = \left(\mathrm{mod}\left(M\omega_{est}T_s + \pi, 2\pi\right) - \pi\right)/M \tag{B.1}$$

and assuming that the frequency offset is less than $1/(2MT_s)$, or expressed mathematically:

$$\omega_{est} = \pm 2\pi\left(1/(2MT_s) - \delta_1\right) \tag{B.2}$$

where $0 < \delta_1 \le 1/(2MT_s)$, that this implies that:

$$\Delta\Phi_{est}(kT_s) = \omega_{est}T_s \tag{B.3}$$

Proof:

Substituting equation (B.2) into equation (B.1):

$$\Delta\Phi_{est}(kT_s) = \left(\mathrm{mod}\left(M\left(\pm 2\pi\left(1/(2MT_s) - \delta_1\right)\right)T_s + \pi, 2\pi\right) - \pi\right)/M \tag{B.4}$$

$$\Delta\Phi_{est}(kT_s) = \left(\mathrm{mod}\left(\pm\left(\pi - 2M\pi T_s\delta_1\right) + \pi, 2\pi\right) - \pi\right)/M \tag{B.5}$$

$$\Delta\Phi_{est}(kT_s) = \left(\mathrm{mod}\left(\pm\pi\left(1 - 2MT_s\delta_1\right) + \pi, 2\pi\right) - \pi\right)/M \tag{B.6}$$

From the assumptions above:

$$0 < (2MT_s\delta_1) \le 1 \tag{B.7}$$

$$1 < 1 + (2MT_s\delta_1) \le 2 \tag{B.8}$$

$$1 - (2MT_s\delta_1) < 1 \le 2 - (2MT_s\delta_1) \tag{B.9}$$

which implies that $(1\text{-}2MT_s\delta_1)$ is less than one and, hence, the value inside the modulus of equation (B.6) will always be within 2π which allows for the modulus to be removed:

$$\Delta\Phi_{est}(kT_s) = \left(\pm\pi\left(1-2MT_s\delta_1\right)+\pi-\pi\right)/M \tag{B.10}$$

$$\Delta\Phi_{est}(kT_s) = \left(\pm\pi\left(1-2MT_s\delta_1\right)\right)/M \tag{B.11}$$

$$\Delta\Phi_{est}(kT_s) = \pm\pi\left(1/M-2T_s\delta_1\right) \tag{B.12}$$

$$\Delta\Phi_{est}(kT_s) = \pm2\pi\left(1/\left(2MT_s\right)-\delta_1\right)T_s \tag{B.13}$$

Replacing terms in equation (B.13) using equation (B.2) yields:

$$\Delta\Phi_{est}(kT_s) = \omega_{est}T_s \tag{B.14}$$

Q.E.D.